Schweizerische Eidgenossenschaft
Confédération suisse
Confederazione Svizzera
Confederaziun svizra

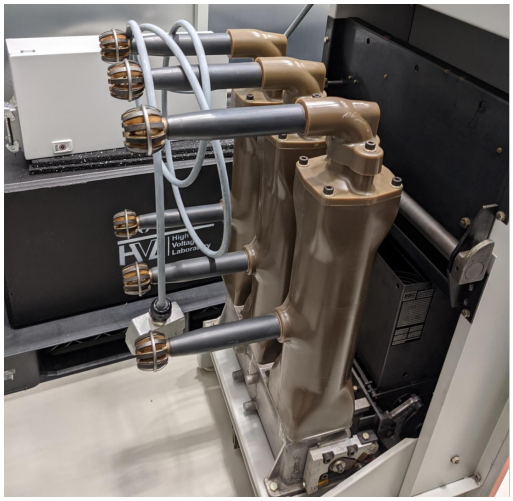
Federal Department of the Environment,
Transport, Energy and Communications DETEC

Swiss Federal Office of Energy SFOE
Energy Research and Cleantech

Final report dated November 23, 2025

INCITE

Intelligent Maintenance of Gas Circuit Breakers





©ETHZ 2025



Date: November 23, 2025

Place: Bern

Publisher:
Swiss Federal Office of Energy SFOE
Energy Research and Cleantech
CH-3003 Bern
www.bfe.admin.ch

Authors:
Chi-Ching Hsu, High Voltage Laboratory, ETH Zürich, hsuch@ethz.ch
Christian M. Franck, High Voltage Laboratory, ETH Zürich, cfranck@ethz.ch
Olga Fink, Intelligent Maintenance and Operations Systems, EPFL, olga.fink@epfl.ch

SFOE Project coordinators:
Dr. Michael Moser, michael.moser@bfe.admin.ch

SFOE contract number: SI/502080

The authors bear the entire responsibility for the content of this report and for the conclusions drawn therefrom.

Summary

Circuit breakers (CB) are designed to withstand and interrupt during normal and short-circuit operating conditions. They play a critical role in the safety and reliability of electrical transmission and distribution systems, because any CB failure can lead to severe consequences, such as equipment damage or even widespread blackouts. However, globally, over 65% of CBs still operate without a condition monitoring system. Even when it exists, it is typically limited to basic parameters, such as gas pressure with static thresholds. While these parameters are simple to monitor and straightforward to interpret, they only cover a small subset of malfunctioning mechanisms.

Therefore, CB condition monitoring with more advanced signals has been studied in the literature. In particular, vibration signals and acoustic emissions have gained increasing attention for their non-intrusive, real-time monitoring capabilities. In these studies, supervised methods were typically used for fault diagnostics, where ground-truth fault types are known due to artificially induced faults in laboratory settings. The objective of all these methods is to demonstrate that the models can differentiate between healthy conditions and various known fault types. These approaches, however, are not feasible in real-world applications, where fault labels are unavailable. In addition, it is challenging to collect data representing every possible fault type.

Another challenge in artificially induced faults is that it does not permit monitoring of gradual CB degradation or aging over time. While fault detectability is usually the primary criterion, it does not address the ability to detect faults early, track their evolution, or even perform fault prognosis. The experiment with induced faults can only distinguish between discrete healthy and faulty states, without capturing the continuous evolution of degradation over time.

In this thesis, a novel CB condition monitoring framework with three modules: feature-based, similarity-based, and machine learning (ML)-based module, using mainly vibration signals, is proposed to tackle these challenges and bridge the gaps between research and real-world applications. The feature-based module identifies features that reflect the CB's condition with distinct degradation trajectories over time. The similarity-based module compares the new operational data to the healthy baseline without the need for domain knowledge to determine which features to extract. The ML-based module includes an unsupervised fault detection and segmentation pipeline, enabling the detection of deviations from the healthy state. In addition, the explainable artificial intelligence (XAI) approach is applied to the detected faults for fault diagnostics.

The framework was applied to multiple CBs across various types with different faults. In this study, multiple run-to-failure CB datasets with more than 30 000 no-load opening and closing operations, featuring various condition monitoring signals such as vibration, coil current, and travel curve, were collected, analyzed, and made publicly available for further analysis. Depending on the CB-fault combination, some indicators are well-suited for continuous condition monitoring due to their gradual changing trend over time, which likely correlates with the true degradation condition. Others are less useful, as they show abrupt changes only before or at failure, or nearly no change during the entire run-to-failure process. In addition, a customized CB condition monitoring system with sensors and data acquisition systems was developed and installed in a substation, monitoring four CBs with the proposed condition monitoring framework for more than a year. This thesis opens the possibility for accurate tracking of the CB condition over time without the need to have ground-truth fault labels, enabling transition of maintenance strategies from time-based to condition-based maintenance or even to predictive maintenance.

Zusammenfassung

Leistungsschalter sind so konstruiert, dass sie unter normalen Betriebsbedingungen und bei Kurzschlüssen zuverlässig unterbrechen. Sie spielen eine entscheidende Rolle für die Sicherheit und Zuverlässigkeit von elektrischen Energieübertragungssystemen. Jeder Ausfall eines Leistungsschalters kann schwerwiegende Folgen haben, wie z. B. die Schädigungen von Komponenten des Energienetzes oder sogar weitreichende Stromausfälle. Weltweit werden jedoch immer noch über 65 % der Leistungsschalter ohne Zustandsüberwachungssystem betrieben. Selbst wenn ein solches System vorhanden ist, beschränkt es sich in der Regel auf grundlegende Parameter wie den Gasdruck mit statischen Schwellenwerten. Diese Parameter sind zwar einfach zu überwachen und leicht zu interpretieren, decken jedoch nur einen kleinen Teil möglicher Defekte ab.

Daher wurde in der Literatur die Zustandsüberwachung von Leistungsschaltern basieren auf mehreren komplexen Messgrössen untersucht. Insbesondere mechanische Vibration und akustische Signale haben aufgrund ihrer nicht-intrusiven Echtzeit-Überwachungsfähigkeiten zunehmend Aufmerksamkeit erlangt. In diesen Studien wurden überwachte Methoden für die Defekt-Diagnose verwendet, bei denen die tatsächlichen Defekttypen aufgrund künstlich erzeugter Defekte im Labor bekannt sind. Das Ziel dieser Methoden war es zu zeigen, dass die Modelle zwischen defektfreien Zuständen und verschiedenen bekannten Defekttypen unterscheiden können. Diese Ansätze sind jedoch in realen Anwendungen, in denen keine Defektlabels verfügbar sind, nicht umsetzbar. Darüber hinaus ist es technisch unmöglich zuverlässige Daten zu sammeln, die alle möglichen Defekttypen abdecken.

Eine weitere Herausforderung bei künstlich erzeugten Defekten besteht darin, dass sie keine Abbildung des allmählichen Verschleisses oder der Alterung von Leistungsschaltern ermöglichen. Die Erkennung von Defekten ist zwar das Hauptkriterium, jedoch wird dabei nicht berücksichtigt, ob Defekte frühzeitig erkannt, ihre Entwicklung verfolgt oder sogar Prognosen erstellt werden können. Das Experiment mit künstlich erzeugten Defekten kann nur zwischen diskreten defektfreien und defekten Zuständen unterscheiden, ohne die kontinuierliche Entwicklung der Verschlechterung zu erfassen.

In dieser Forschungsarbeit wird ein neuartiges Framework zur Zustandsüberwachung von Leistungsschaltern vorgestellt. Es besteht aus drei Modulen: ein merkmalsbasiertes, ein ähnlichkeitsbasiertes und ein auf maschinellem Lernen (ML) basierenden Modul. Dieses Framework wurde entwickelt, um die genannten Herausforderungen zu bewältigen und die Lücke zwischen Forschung und realen Anwendungen zu schliessen. Das merkmalsbasierte Modul identifiziert Merkmale, die den Zustand des Leistungsschalteres mit eindeutigen Verschlechterungsverläufen im Laufe der Zeit widerspiegeln. Das ähnlichkeitsbasierte Modul vergleicht die neuen Betriebsdaten mit der gesunden Basislinie, ohne dass Fachwissen erforderlich ist, um zu bestimmen, welche Merkmale extrahiert werden sollen. Das ML-basierte Modul umfasst eine unüberwachte Defekterkennungs- und Segmentierungspipeline, die die Erkennung von Abweichungen vom gesunden Zustand ermöglicht. Darüber hinaus wird der Ansatz der erklärbaren künstlichen Intelligenz auf die erkannten Defekte angewendet, um eine Diagnose zu erstellen.

Das entwickelte Framework wurde auf mehreren Leistungsschaltern verschiedener Typen und mit unterschiedlichen Defekten angewendet. In dieser Forschungsarbeit wurden mehrere Run-to-Failure-Datensätze von Leistungsschaltern erzeugt, die über 30 000 Ein- und Ausschaltvorgänge ohne Storm umfassen. Dabei wurden verschiedene Zustandsüberwachungssignale, wie Vibration, Spulenstrom und Position über Zeit, aufgezeichnet und analysiert. Diese Datensätze sind der Öffentlichkeit für weiterführende Analysen zur Verfügung gestellt. Je nach Kombination aus Schaltertyp und Defekttyp eignen sich einige Indikatoren aufgrund ihres allmählichen Veränderungstrends im Laufe der Zeit, der wahrscheinlich mit dem tatsächlichen Degradationzustand korreliert, gut für die kontinuierliche Zustandsüberwachung. Andere sind weniger nützlich, da sie nur vor oder bei einem Ausfall abrupte Veränderungen zeigen oder während des gesamten Run-to-Failure-Prozesses fast keine Veränderungen aufweisen. Darüber hinaus wurde ein massgeschneidertes System zur Zustandsüberwachung von Leistungsschaltern entwickelt und in einem Umspannwerk installiert, das vier Leistungsschalter mit dem Framework zur Zustandsüberwachung über einen Zeitraum von mehr als einem Jahr überwacht hat. Diese Arbeit eröffnet die Möglichkeit einer genauen Verfolgung des Zustands von Leistungsschaltern, ohne dass

Ground-Truth-Defektlabels erforderlich sind. Damit ermöglicht sie den Übergang von zeitbasierten zu zustandsbasierten Wartungsstrategien oder sogar zu vorausschauender Wartung.

Contents

Summary 4

Zusammenfassung 5

List of abbreviations 10

Definitions & Terminology 11

1 Introduction 13

1.1 Motivation . . . 13
1.2 Challenges . . . 13
1.3 Research Questions . . . 15

2 Fundamentals of Circuit Breakers 17

2.1 Functionality . . . 17
2.2 Main Components . . . 18
2.2.1 Auxiliary Circuits . . . 18
2.2.2 Contacts . . . 19
2.2.3 Interruption Chamber . . . 20
2.2.4 Operating Mechanism . . . 20
2.3 Vacuum Circuit Breaker . . . 22
2.4 Gas Circuit Breaker . . . 22
2.5 Condition Monitoring Signals and Sensors . . . 24
2.5.1 Coil Current . . . 24
2.5.2 Dynamic Contact Resistance . . . 24
2.5.3 Travel Curve . . . 25
2.5.4 Operating Timing . . . 25
2.5.5 Vibration and Acoustic Signals . . . 26

3 Overview of Data-driven Condition Monitoring Approaches 27

3.1 Overview . . . 27
3.2 Anomaly and Fault Detection . . . 28
3.2.1 Similarity-based Methods . . . 28
3.2.2 Reconstruction-based Methods . . . 28
3.3 Fault Segmentation . . . 28
3.4 Fault Diagnostics . . . 29
3.4.1 Explainable Artificial Intelligence . . . 29

4 State of the Art in CB Condition Monitoring 30

4.1 Condition Monitoring on Circuit Breakers . . . 30
4.2 Condition Monitoring Signals of Circuit Breakers . . . 30
4.2.1 Coil Current . . . 30
4.2.2 Travel Curve . . . 31
4.2.3 Acoustic Signal . . . 31
4.2.4 Vibration Signals . . . 31

4.3 Data-Driven Approaches for CB Condition Monitoring . . . 32
4.3.1 eXplainable Artificial Intelligence (XAI) . . . 32
4.3.2 CB Condition Monitoring . . . 33
4.4 Research Gaps . . . 34

5 Aim and Structure of this Work 35

5.1 Aim of this Work . . . 35
5.2 Structure of this Work . . . 35

6 Experimental Setup and Dataset 37

6.1 MV Vacuum Circuit Breaker - Run-to-Failure . . . 38
6.2 MV Vacuum Circuit Breaker - Current Interruption . . . 39
6.3 MV Gas Circuit Breaker - Run-to-Failure . . . 39
6.3.1 IoT Box . . . 39
6.4 MV Oil Circuit Breaker - High-speed Camera . . . 40
6.5 HV Gas Circuit Breakers - Run-to-Failure . . . 41
6.6 HV Gas Circuit Breaker - Fault Injection . . . 44
6.7 HV Gas Circuit Breakers - Substation . . . 46
6.8 Influence of Operating Conditions . . . 47
6.8.1 With and Without Current Load . . . 47
6.8.2 Vibration Sensor Mounting Position and Orientation . . . 48
6.8.3 Idle Time between Operations . . . 50
6.8.4 CB Fixation . . . 50
6.8.5 Spring Load Conditions . . . 51
6.8.6 Laboratory and Substation . . . 53

7 Proposed Condition Monitoring Framework 54

7.1 Assumptions . . . 54
7.2 Overview . . . 54
7.3 Feature-based Module . . . 56
7.3.1 Identification of Key Moments and Operation Stages . . . 56
7.3.2 Vibration and Acoustics Features . . . 61
7.3.3 Coil Current Features . . . 62
7.3.4 Travel Curve Features . . . 62
7.3.5 Motor Charging Time . . . 63
7.3.6 Operating Timing Features . . . 63
7.4 Similarity-based Module . . . 65
7.4.1 Time Series Similarity . . . 65
7.4.2 Spectrogram Similarity . . . 65
7.5 Machine Learning-based Module . . . 66
7.5.1 Convolutional Autoencoder (CAE) . . . 67
7.5.2 Fault Detection and Segmentation . . . 67
7.5.3 XAI-guided Fault Diagnostics . . . 69
7.6 Implementation Details . . . 70
7.6.1 HV Gas Circuit Breaker - Fault Injection . . . 70
7.6.2 HV Gas Circuit Breakers - Run-to-failure . . . 72

7.6.3 HV Gas Circuit Breakers - In Substation . . . 73
7.7 Summary and Limitations . . . 74

8 Application of the Proposed Framework 75

8.1 Feature-based Module . . . 75
8.1.1 HV Gas Circuit Breakers - Run-to-Failure . . . 75
8.1.2 MV Gas Circuit Breaker - Run-to-Failure . . . 87
8.1.3 MV Vacuum Circuit Breakers - Run-to-Failure . . . 91
8.1.4 HV Gas Circuit Breakers - In Substation . . . 92
8.2 Similarity-based Module . . . 93
8.2.1 HV Gas Circuit Breakers - Run-to-Failure . . . 93
8.2.2 MV Gas Circuit Breaker - Run-to-Failure . . . 97
8.3 Machine Learning-based Module . . . 99
8.3.1 HV Gas Circuit Breakers - Run-to-Failure . . . 99
8.3.2 HV Gas Circuit Breaker - Fault Injection . . . 100
8.3.3 MV Gas Circuit Breaker - Run-to-Failure . . . 108
8.3.4 HV Gas Circuit Breakers - In Substation . . . 108
8.4 Integrated Module . . . 110
8.4.1 HV Gas Circuit Breakers - Run-to-Failure . . . 110
8.4.2 MV Gas Circuit Breaker - Run-to-Failure . . . 111
8.4.3 Summary of the Integrated Module Applications . . . 112

9 Discussion 113

9.1 Continuous CB Condition Monitoring . . . 113
9.2 Effectiveness of the Proposed Framework . . . 114
9.2.1 Feature-based Module . . . 114
9.2.2 Similarity-based and ML-based Module . . . 114
9.2.3 Integration of the Three Modules . . . 114
9.3 Practical Considerations for Substation Deployment . . . 115
9.3.1 Idle Time Effect . . . 115
9.3.2 Threshold-action List . . . 116
9.3.3 Transferability between CBs . . . 116
9.4 Limitations and Challenges . . . 116
9.4.1 General Data Scarcity and Lack of Labels . . . 116
9.4.2 Thresholds for Fault Detection . . . 117

10 Conclusions and Outlook 118

11 National and International Cooperation 120

12 Publications and Other Communications 122

13 Open Access Dataset 122

14 References 123

List of abbreviations

AC alternating current

CIGRE International Council on Large Electric Systems

DAQ data acquisition

EMI electromagnetic interference

GCB gas circuit breaker

GWP global warming potential

HV high-voltage

IoT Internet of Things

MV medium-voltage

OCM online condition monitoring

PHM prognostics and health management

VCB vacuum circuit breaker

Definitions & Terminology

The key definitions and terminology essential for understanding this work is provided here. Most terms are derived from established literature and relevant standards [1, 2, 3].

Anomaly/abnormal condition: An anomaly is an observation that deviates considerably from some concept of normality [4]. A fault that occurred in a CB can be considered as an anomaly and the CB is in a abnormal condition. However, an anomaly indicates anything that deviates from normal or healthy, meaning that it does not necessarily have to be a fault, but could also be a change in operating condition (maintenance work, environment temperature, gas pressure, etc.) or any other change that causes a CB to change its behavior.

Condition/health indicator: A condition indicator refers to a specific feature within system data that exhibits predictable changes as the system undergoes degradation or operates in different operational modes [5]. It encompasses any feature that proves valuable in differentiating normal operation from faulty or any deviation from normal operation. Health indicators, in contrast, integrate multiple condition indicators into a single value, providing the end user with a comprehensive health status of the component or machine itself.

Fault/faulty condition: This term is commonly used in both machine learning and circuit breaker communities, but with different meanings. According to IEEE Standard Definitions for Power Switchgear, a fault refers to a short-circuit event [2], such as terminal or short-line faults. However, in the field of machine learning, fault usually appears in the context of fault detection, where a fault is a malfunction in a system or a machine. In this work, a fault refers to a defect in a CB component such as a malfunctioning spring or damper. In such cases, the CB could possibly still remain in service, but its short-term reliability is likely reduced [1]. This component-based definition is used because this aligns with the focus of assessing CB condition. Here, faults are treated as a subset of anomalies. A fault in the context of short-circuit event is denoted as short-circuit in this work.

Idle time: The time between consecutive operations of a CB during which the CB remains static [6].

Major failure (MaF): According to a CIGRE reliability survey, a MaF is a complete failure of a CB which causes the lack of one or more of its fundamental functions [3, 7]. The CB is not able to function anymore when encounter a MaF.

Minor failure (MiF): According to a CIGRE reliability survey, a MiF is any failure of a constructional element or a subassembly which does not cause a major failure [7]. A MiF means that a CB experiences a fault and is in a faulty condition but still functional.

Non-intrusive monitoring: Non-intrusive monitoring means that the CBs remain connected to the grid and remain fully functional during the monitoring process. Unlike intrusive monitoring technique, for which the CBs need to be disconnected from the grid. In some works, non-intrusive is also called non-invasive, but in this work it is referred to non-intrusive.

Online condition monitoring: Continuous online (equipment energized and connected to the network with the device(s) permanently installed) monitoring of primary equipment to measure and evaluate one or more characteristic parameters with the intention of automatically determining and reporting the real-time state of the equipment [8].

Predictive maintenance: There is no unified definition of predictive maintenance, but the core concept involves using data collected from OLCM systems to assess and forecast a machine's condition. This enables optimization of machine availability and maintenance scheduling while minimizing the costs associated with unscheduled downtime [9, 10].

Run-to-failure experiment: A test unit is continuously operated, with or without maintenance, until it ultimately fails. In this case, failure means a MaF, where the test unit stops functioning. This is typically done for testing the reliability of the test unit, such as industrial bearings [11, 12].

Sensor/signal/feature: Sensors, such as accelerometers or microphones, are devices that capture measurements. Signals are the resulting data from the sensors, typically in the form of time series.

Signal processing approach is commonly used to extract information from the signals. Features, such as peak or mean, are specific values derived from these signals that should characterize the monitored machine's condition.

1 Introduction

This report is largely copied from the doctoral thesis [13].

1.1 Motivation

*Parts of this section are based on the publication*s [14, 15].

Circuit breakers (CBs) are an essential part of the grid and are designed to withstand and interrupt during normal and short-circuit operating conditions. Therefore, they play a critical role in the safety and reliability of electrical transmission and distribution systems, particularly in recent years due to the expansion of renewable energy with more frequent switching operations. They are known for their high reliability and low failure rate, as been confirmed by the surveys from the International Council on Large Electric Systems (CIGRE) [16, 17, 7].

Due to the increasing demand for electricity in the past decades, the transmission and distribution systems were expanded, and the number of installed CBs increased. These CBs commissioned decades ago, are now approaching their end of service life as defined by the manufacturer or regulator, typically several decades [18, 19]. However, they may be still in a good condition to be operated even after decades because of their infrequent operations (in average less than 50 operations per year [16]). Therefore, extending their service lifespan, provided that their condition is monitored and the safe and reliable operations can be ensured, is advantageous for both cost savings and environmental sustainability [20, 21].

To ensure the reliable and safe operation of CBs and enable timely detection of deviations from normal operation, it is crucial to implement an online condition monitoring (OCM) system [8]. Such a system typically involves a data acquisition (DAQ) system and data analysis algorithms that assess CB health conditions based on the collected data. By using such condition monitoring systems, deviations from the healthy condition can be detected, allowing for early intervention before the CB fails in operation.

Although many studies have demonstrated the feasibility of monitoring CB conditions in laboratory environments for decades [22, 23], the deployment of OCM systems in real-world applications remains limited. In practice, most CBs are either not monitored at all or are equipped only with sensors that capture a limited range of fault types, such as gas pressure sensors monitoring gas pressure with predefined thresholds [20].

With the recent success of data-driven methods across various domains [24, 25, 26], this work investigates their feasibility for prognostics and health management (PHM) tasks for CBs. In addition, advances in Internet of Things (IoT) technology also enable real-time data transmission from OCM systems. Thus, this work investigates the possibility of developing a condition monitoring framework by first identifying the suitable sensors for effectively assessing and tracking the evolution of the CB condition, first in a laboratory environment and then in substations, bridging the gap between laboratory and real-world CB condition monitoring applications and advancing from time-based to condition-based or even to predictive maintenance strategies.

1.2 Challenges

Even though the success of data-driven approaches has been demonstrated in various fields, several challenges remain when applying these approaches in the field of CB condition monitoring.

Track CB Degradation over Time

The understanding of CB degradation and aging processes remain largely incomplete or even unknown [27], since most CBs in service are not continuously monitored. Data for CB assessment is

typically collected during time-based inspections with several years interval, providing only a few discrete points within the CB's lifespan. Only a limited number of studies focus on run-to-failure perspective [28, 29, 30, 31], which is essential for capturing the degradation trajectories over time and enabling fault detection or even RUL prediction.

While CB mechanical endurance tests are commonly performed with 2 000 no-load switching operations for M1 class and 10 000 operations for M2 class [21], these tests focus on the reliability of CBs. These operations are often not continuously monitored or are only assessed at specific intervals, such as one measurement every 500 operations. As a result, the mechanical degradation trend of CBs remains largely unexplored and cannot be effectively captured using existing supervised fault diagnostics methods. In addition, type test requires only a specified number of successful operations and are not usually continue until the CB reaches its end-of-life.

To effectively assess degradation and aging in CBs, continuous monitoring using non-intrusive measurement techniques is essential, ensuring that the monitoring process does not interfere with the integrity or functionality of the monitored CBs. While they typically operate infrequently, certain applications, such as capacitor bank switching, can still have a high number of operations. Gaining deeper insights into aging mechanisms remains challenging because of their complexity, with multiple components operating under different conditions. For reliable long-term CB condition assessment, it is essential to identify and analyze the evolution of indicators that effectively reflect the CB's condition over time.

Identification of Key Condition Monitoring Features

To monitor CB condition, several types of sensors have been used to capture different aspect of CB conditions, such as position encoders for travel curves and accelerometers for vibration. These sensors product time-series signals recorded by a DAQ. A wide range of signals has been studied in the literature, mainly in the context of fault diagnostics, aiming to distinguish between different faulty conditions of mechanical and electrical CB components, such as springs, dampers, latches, coils, motors, and contacts [22]. Commonly used health monitoring signals include the coil current [32, 33], travel curves [34, 35], dynamic contact resistance [36, 37], acoustic emissions [38, 39, 40], and vibration [41, 23, 42].

To improve interpretability, features are typically extracted from these high-dimensional signals. These features usually have lower dimensionality and can represent some parts of the original signals. They need to reflect the health status over time and should be sensitive to the changes of CB conditions, showing either a gradually increasing or decreasing trend as the CB degrades and approaches failure [43]. Ideally, they should also be robust to noise and show distinct trends for different fault types, facilitating fault diagnostics.

General Data Scarcity and Lack of Labels

Data scarcity is a challenge in some data-driven applications, referring to the insufficient amount of data available to effectively train models or learn underlying patterns. This issue is particularly critical in CB condition monitoring due to the following reasons. First, CBs typically operate infrequently, so even if OCM systems are installed, the volume of collected data remains low. Second, OCM systems are rarely deployed on CBs in substations, and when present, are often limited to small-scale projects [44, 45] or records of only a few parameters.

Moreover, within the already limited amount of data, faulty instances represent only a small fraction due to the low failure rate of CBs. Identifying ground truth failure information often requires root cause analysis, which can be costly and inconclusive depending on the underlying causes. Therefore, data-driven methods are still limited in the field of CB condition monitoring.

Lack of Interpretability of Detected Faults

Parts of this section are based on the publication [15].

To monitor CB health condition, besides tracking changes over time, knowledge about the underlying fault types is necessary, as it supports planning of interventions and maintenance actions when faults occur. While fault detection approaches have shown success in many domains using only healthy data [46], they usually do not provide additional information regarding the specific fault types.

Beyond simply detecting the presence of a fault, it is also important to distinguish between different fault types, with or without explicitly labeling them. Fault segmentation involves grouping faulty samples using unsupervised clustering methods, but fault segmentation alone does not inherently provide information regarding the specific fault types. Various fault segmentation approaches have been proposed for different systems [47, 48], but such approaches have not yet been applied to CBs. Furthermore, while they can identify different clusters, determining which cluster corresponds to a particular fault type typically requires domain knowledge. In straightforward cases, where a fault type is linked to deviations in a small subset of features, this task may be relatively simple. However, for more complex fault patterns, experts may struggle to assign fault type labels and may require additional guidance.

Contrary to fault segmentation, fault diagnostics goes one step further and aims to identify specific fault types, which is typically achievable only through supervised learning approaches where labels are available. In current CB condition monitoring research, fault diagnostics is generally performed by training a supervised model. Existing CB works predominantly focus on fault diagnostics with artificially introduced faults such as mechanism jam and spring shedding [49], providing ground-truth labels. The objective of all these methods is to demonstrate that the models can differentiate between healthy conditions and various known fault types. However, obtaining labels for CBs in real operations, without having a training dataset with artificially induced faults, is challenging. In addition, it is difficult, if not impossible, to collect data representing every possible fault type [46, 50, 51].

Transferability from Laboratory to Substation Environment

The goal is to monitor CBs also in substations, where high acoustic and electromagnetic noise environments are expected. Therefore, the transferability of the CB condition monitoring framework and the applicability of the OCM system from a laboratory to a real-world substation environment have to be evaluated. Specifically, the impact of the presence of switching currents during the interruption process and the electromagnetic interference (EMI) on signal quality, as well as the stability of data acquisition and transmission, needs to be assessed. It is essential to investigate the applicability and limitations of laboratory-based findings in real-world substation applications to ultimately deploy the OCM system in substations.

1.3 Research Questions

The following research questions were raised from the challenges mentioned in the previous section and will be investigated in this work.

1. How can the mechanical degradation and aging processes of CBs be continuously tracked to capture gradual condition changes over time?
2. Which features are most effective for continuous CB condition monitoring to ensure that degradation trends are observable, rather than only detecting abrupt changes?
3. How can challenges related to data scarcity and the lack of ground-truth labels be addressed without relying on artificially introduced faults?
4. How to interpret detected anomalies and potential fault types when ground-truth labels are unavailable during training?

5. How can condition monitoring results obtained in controlled laboratory environments be effectively transferred to real-world substation conditions?
6. How to design and develop an OCM system for CBs under practical constrains:
   (a) only healthy data available,
   (b) only non-intrusive measurement possible,
   (c) only limited amount of data available during development?

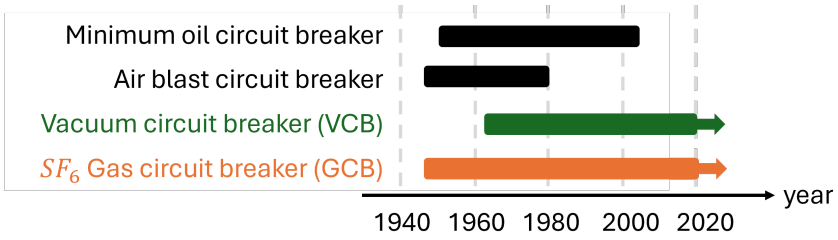


Figure 2.1: Manufacturing period of CBs with different technologies: this work focuses mainly on the modern technologies, namely VCB and GCB. Figure adapted from [6].

2 Fundamentals of Circuit Breakers

This chapter gives a brief overview of circuit breakers (CBs) used for alternating current (AC), providing the necessary background relevant to this work, including their types, components, and functionality.

According to IEEE Standard Definitions for Power Switchgear (IEEE Std C37.100-1992), CB is "a mechanical switching device, capable of making, carrying and breaking currents under normal circuit conditions and also, making and carrying for a specified time and breaking currents under specified abnormal circuit conditions such as those of short-circuit" [2]. Therefore, CBs need to conduct nominal and withstand short-circuit currents when closed, withstand high system and temporary over voltages when open, and rapidly open and extinguish short-circuit current, indicating that they are subjected to thermal, electrical, and mechanical stresses, respectively.

Even though they are subject to demanding stresses, they are well-known for their high reliability, long expected lifespan, and low failure rate [27]. They are considered the most important piece of equipment in the power system, since any unexpected CB failure could lead to catastrophic consequences. Thus, making sure that they operate smoothly without failure is a key to maintaining highly reliable power system.

They are commonly specified according to their voltage level (LV, medium-voltage (MV), or high-voltage (HV)), operating mechanisms (spring, hydraulic, etc.), and interrupting medium (vacuum, sulfur hexafluoride SF_6, ...). For instance, HV spring-operated SF_6 CBs are commonly used in substations nowadays.

In terms of voltage level, LV CBs such as household $230\,\mathrm{V}$ miniature CBs are typically excluded from condition monitoring systems due to limited economic benefits. In contrast, MV and HV CBs are more expensive and critical to system reliability, particularly HV CBs. As a result, they are more suitable candidates for installing condition monitoring systems. This work focuses exclusively on MV and HV CBs.

Besides voltage level, they can also be categorized according to the interrupting medium, such as oil, air, vacuum, and pressurized gas, where CBs using oil or air are relatively old technology [52, 6]. The new installations are typically vacuum or SF_6 CBs, as shown in Figure 2.1. This work focuses on CBs with modern interruption media, namely, vacuum CB (Section 2.3) and SF_6 gas CB (Section 2.4).

2.1 Functionality

A CB switches between open and closed positions and must reliably transition from one to the other state, based on system conditions and requirements. In the closed position, the CB functions as a conductor, allowing current to flow. However, it acts as an insulator in the open position to withstand the system and over voltages.

Transitioning between these two positions involves opening (tripping) and closing operations, which must be completed within a short period of time, typically less than $100\,\mathrm{ms}$, depending on the specific design

and requirements. The opening operation refers to the transition from the closed to the open position, while the closing operation means a change from open to closed position. These operations must be performed reliably under all conditions, no matter if with or without load current, or even under short-circuit conditions.

The main functionalities of CBs can be summarized as following [21]:

1. carry the nominal current in closed position,
2. carry and withstand the short-circuit current in closed position for a certain period of time,
3. perform opening or closing operations on command,
4. interrupt short-circuit current,
5. withstand voltages in open position.

2.2 Main Components

The design of CBs varies by type and manufacturer, but they share some main components, independent of the design, including auxiliary circuits, contacts, operating mechanism, and interruption chamber. All these components are necessary for performing opening and closing operations, usually initiated by external command signals sent to the auxiliary circuits. Once a command signal is received, the stored energy in the operating mechanism is released to actuate, causing contacts to move and change to open or closed positions. A simplified diagram of these components is shown in Figure 2.2.

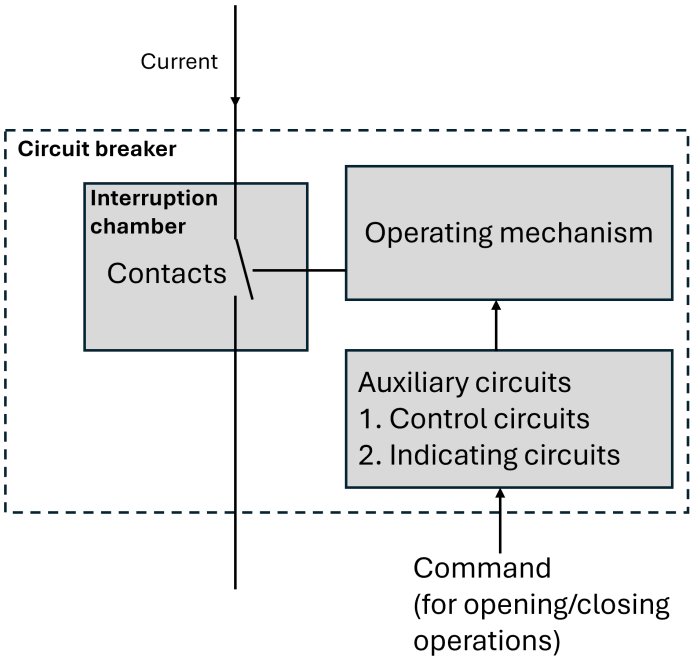


Figure 2.2: Simplified diagram of main components in a circuit breaker including auxiliary circuits, contacts, interruption chamber, and operating mechanism. Figure adapted from [6].

2.2.1 Auxiliary Circuits

Auxiliary circuits consist of control circuit and indicating circuit [6]. To perform opening or closing operations, a command signal is sent to the control circuits, specifically to an open or a close coil (trip

coil). They are solenoids that can be energized once a command signal is received. The energized coil initiates the opening or closing operation. Alternatively, it could also be operated manually by pressing a open or close bottom located on the CB front panel in case the command fails. Typically, each CB has two identical open coils for redundancy, but only one close coil.

Another component of the auxiliary circuits is the indicating circuit (also called auxiliary switch or auxiliary contact), which provides status information such as CB's position. This circuit consists of mechanical switches that are indirectly connected to the main contacts. In addition to indicating the position, it may be connected to protection systems, serving both safety interlocking and position indication purposes.

Typically, two auxiliary switches are used: one that is closed when the CB is closed and open when the CB is open, and another that operates in the opposite manner. This complementary feedback is important for verifying if the CB has operated correctly and for detecting any inconsistencies in position status. In addition, it also interrupts the current to the open and close coils once the operation is complete, protecting the coils and actuation circuits. Both the control and indicating circuits are part of auxiliary circuits and are essential for CB operations.

2.2.2 Contacts

Contacts are the end points of current-carrying conductors inside CB, typically consists of two conductive components such as metal. They should make or break a load or short-circuit current when performing opening operations. They touch each other in closed position to maintain circuit continuity. During opening operations, they are separated to initiate the current interruption process. A switching arc form between the contacts, generating strong local heating and thus burn the contacts. Therefore, they should be made of material with not only good electrical conductivity but also good heat conductivity and low wear.

In HV GCBs, two pairs of contacts are used: main contacts and arcing contacts, as shown in Figure 2.3(a). The main contacts carry the load current when the CB is closed, while the arcing contacts touch first during closing operation and separate last during opening operation to withstand the switching arc. However, contact design and configuration vary depending on the CB type and application. For example, VCBs typically utilize only a single pair of contacts, as illustrated in Figure 2.3(b).

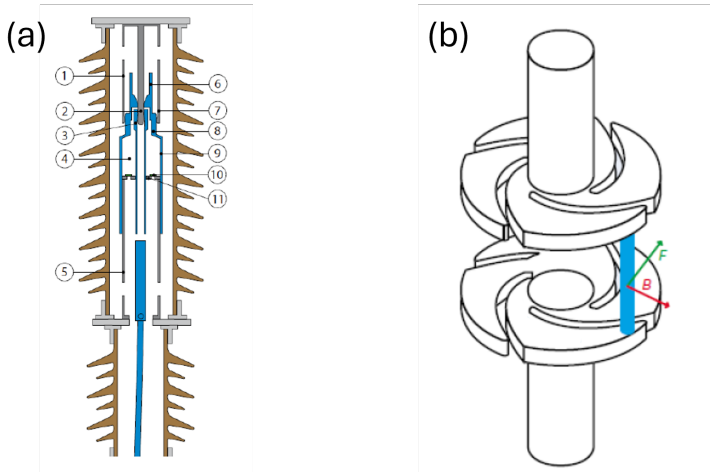


Figure 2.3: Design of contacts varies across CB types: (a) two types of contacts in an HV GCB, consisting of main contacts (⑦ and ⑧) and arcing contacts (② and ③). Further details on other components are explained in Figure 2.6. (b) Only a single pair of contacts is found in a VCB. Figures adapted from [53, 54].

2.2.3 Interruption Chamber

During the current interruption process, a switching arc forms between the contacts and must be extinguished in the interruption chamber. In HV applications, the most commonly used interruption medium is pressurized SF_6 gas, because of its outstanding arc-quenching properties. However, SF_6 is widely recognized for its negative environmental impact, particularly the high global warming potential (GWP) of approximately 23500 over a time horizon of 100 years [55]. As a result, research groups are actively searching for environmental friendly alternative gases.

In MV applications, some CBs use vacuum instead of pressurized gas, with maximum voltage levels of approximately $70\,\mathrm{kV}$ [54]. In the absence of gas, arc formation does not result from ionized gas molecules but from vaporized metal emitted by the contact surfaces during the interruption process. More details on vacuum CB is presented in Section 2.3.

2.2.4 Operating Mechanism

The operating mechanism (also called the mechanical drive or simply drive) is responsible for providing, storing, and releasing the energy required for switching operations. When a switching command is sent to the open or close coil, the stored energy is released and transmitted through mechanical components such as levers and linkages to actuate the contacts. The entire process is typically done within a short time (approximately $40\,\mathrm{ms}$ to $80\,\mathrm{ms}$, depending on CB types and designs). Commonly used operating mechanisms include spring-, hydraulic-, and pneumatic-operated systems.

According to the CIGRE reliability survey [17], approximately half of the CBs included in the survey are equipped with spring-operated mechanisms, mainly due to their high reliability and almost maintenance free characteristics. In these mechanisms, the energy required for operations is stored in springs, usually one for opening and one for closing operation. After each opening operation, a motor recharges the springs to restore the energy. During idle state with no switching events, the energy storage elements should remain fully charged to ensure enough energy is available for subsequent operating command.

In HV applications ($\geq 400\,\mathrm{kV}$), an independent operating mechanism is typically used for each pole since more energy is required, while in MV and lower HV applications, a single operating mechanism can be sufficient to actuate all three poles simultaneously.

Even though CBs are well-known for their high reliability, their complex mechanisms, consisting of a large number of moving parts, make the operating mechanism a main cause of MaF. According to the CIGRE survey, approximately 50% to 66% of CB MaF cases are attributed to problems within the operating mechanism [17, 7].

An example of a three-pole oil MV CB with a spring-operated mechanism is shown in Figure 2.4. The interruption chambers are located on the back side and not visible in the figure. As shown in the figure, the operating mechanism consists of multiple interconnected components, making the interpretation of the recorded vibration signals challenging.

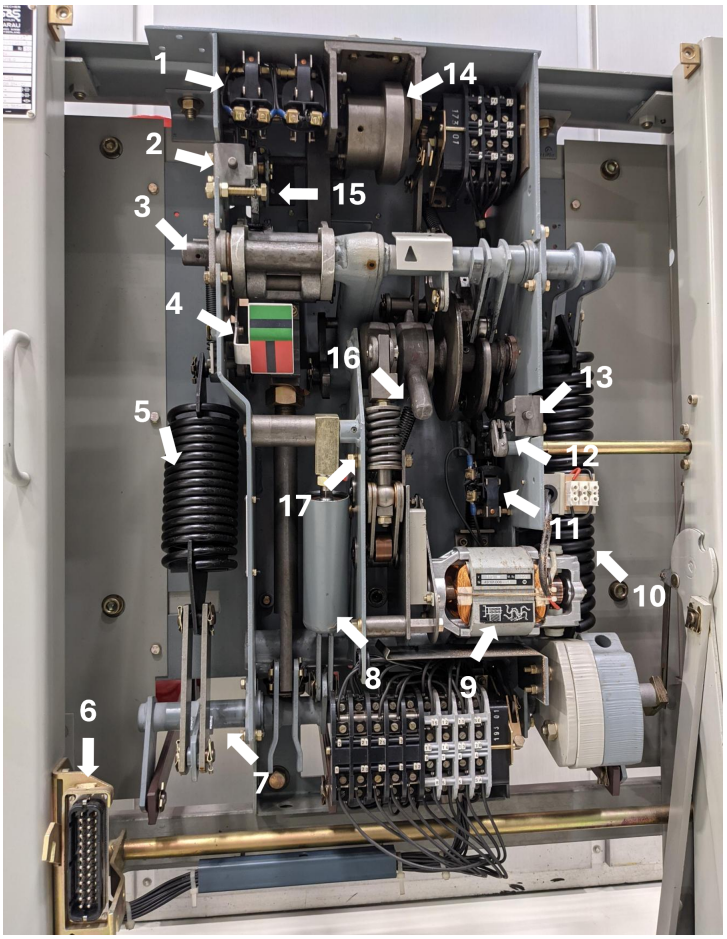


Figure 2.4: The components of a spring-operated MV oil CB, with the front panel removed. 1: open coil (2x), 2: button for opening operation, 3: secondary shaft, 4: position indicator, 5: open spring, 6: wire connector, 7: main shaft, 8: damper, 9: motor, 10: close spring, 11: close coil, 12: latch for close, 13: button for close, 14: cam, 15: latch for open, 16: manual charging lever, 17: charging mechanism.



Figure 2.5: An example of a MV VCB with three poles and a single spring-operated mechanism.

2.3 Vacuum Circuit Breaker

Parts of this section is written based on [54], for more details about VCB, please refer to Section 4.4.5 in [54].

Vacuum is commonly used as interruption medium instead of pressurized gas such as SF_6 in MV applications because vacuum offers several advantages, including no greenhouse gas used, no gas handling infrastructure needed, and less to almost no maintenance works [6].

The degree of vacuum in interruption chamber is approximately in a range of $10^{-5}\,\mathrm{Pa}$ to $10^{-6}\,\mathrm{Pa}$ [52, 54]. Even though no gas molecules are available for arc formation, an arc is generated by the metal vapor plasma released from the contact surface during the interrupting process. An example of a spring-operated MV VCB is shown in Figure 2.5, with a single operating mechanism for three poles. There is only one pair of contacts for each pole and the shapes of the contacts are typically butt type for more compact design, as shown in Figure 2.3(b). For cases with higher current interruption, the contact is further shaped with arc rotator to quickly extinguish the arc.

2.4 Gas Circuit Breaker

Parts of this section is written based on [54], for more details about GCB, please refer to Section 4.3.4 in [54].

Instead of vacuum, some CBs utilized pressurized gas as the interruption medium, particularly in HV applications but can also be found in MV ranges. The most commonly used gas is SF_6 due to its superior dielectric strength and interruption capability. Due to the difference in gas compression, the SF_6 CBs can be further separated into puffer and self-blast CBs. The focus of this section is only on puffer CBs as they were investigated in the experiments.

An example of the interruption sequence in a puffer CB is shown in Figure 2.6. As stated in Section 2.2.2, a typical GCB is equipped with two pairs of contacts: main and arcing contacts. The main contacts conduct current when the CB is closed, whereas the arcing contacts withstand the high temperature generated during the arcing process.

During the opening operation, the main contacts separate first, causing the current to commutate to the arcing contacts. An arc forms between the arcing contacts, as illustrated in Figure 2.6(b) and later,

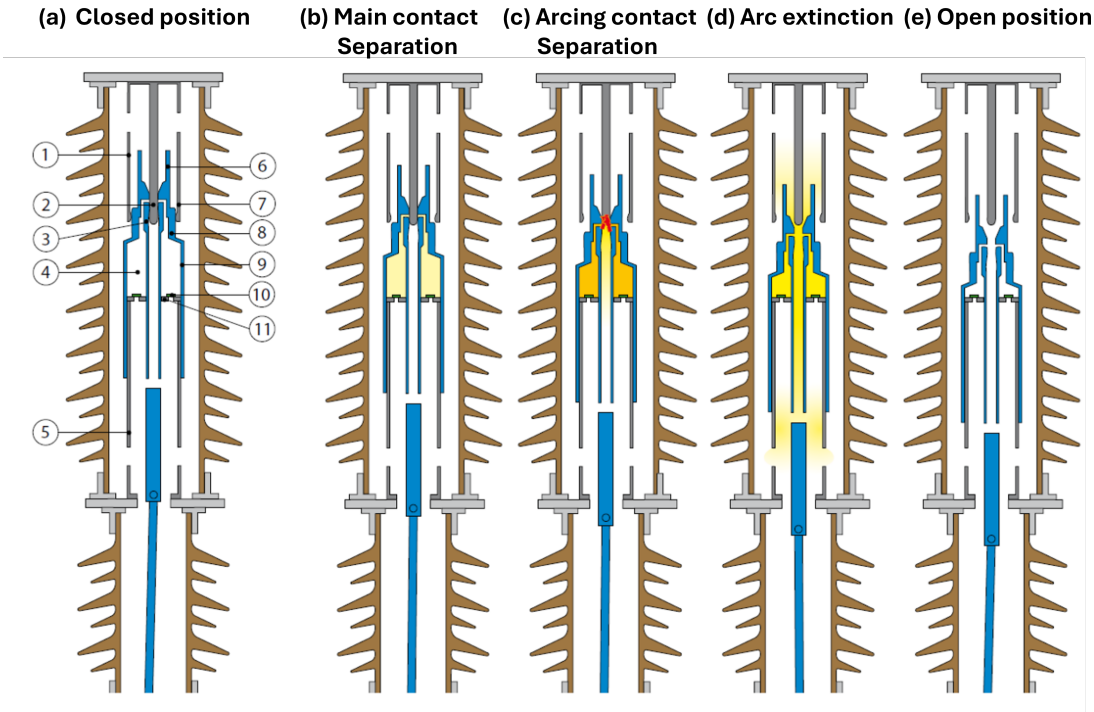


Figure 2.6: (a) Schematic of a puffer CB. ①: upper current path (fixed), ②: arcing contact (fixed), ③: arcing contact (moving), ④: puffer volume, ⑤: lower current path (moving), ⑥: nozzle, ⑦:main contact (fixed), ⑧: main contact (moving), ⑨: puffer cylinder, ⑩: refill valve, ⑪: stationary piston. The interruption process of a puffer CB: (b) The main contact separation, the current commutates to arcing contact (c) The arc form when the arcing contact separates (d) The arc is extinguish around current zero (e) The CB is in open position. Figure modified from [54].

Figure 2.6(c). To extinguish the arc, the mechanical movement of the operating mechanism compresses the gas. A nozzle is shaped to guide the gas towards the arc. As the arc cross-section becomes smaller when it approaches current zero, the compressed gas extinguishes the arc, as displayed in Figure 2.6(d). Finally, the movement of the operating mechanism stops, and the CB is open, marking the completion of the interruption process and the opening operation, as shown in Figure 2.6(e).

The single pressure SF_6 CBs are considered to have high reliability with a low failure rate of approximately only 0.5% per 100 CB-year and are widely used. As a result, they are the main focus in the CIGRE reliability surveys [17, 7] and also being investigated in this work.

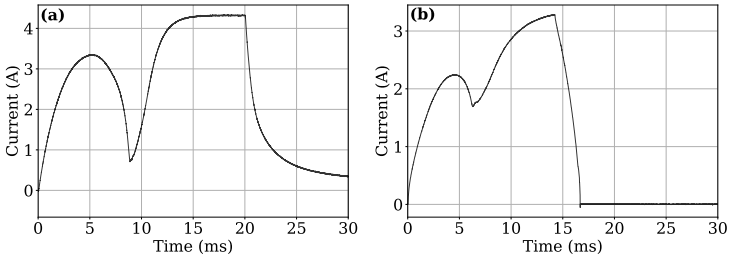


Figure 2.7: Example open coil current signals from two MV CBs: (a) GCB and (b) VCB. While the overall coil current shapes differ between CB types, both show a similar two-stage increasing trend.

2.5 Condition Monitoring Signals and Sensors

Parts of this section are based on the publication [14].

To assess the condition of a CB, various monitoring signals with different levels of complexity have been proposed, some of which are already used as part of routine inspection procedures in substations. These signals range from easily interpretable indicators to more advanced signals. For instance, gas pressure is a commonly monitored parameter used to detect SF_6 leakage for GCBs. In addition, the number of operations is often tracked as a potential indicator of aging and degradation. Some of these commonly used CB condition monitoring signals are presented in this section.

2.5.1 Coil Current

The current passing through the open or close coils marks the start of the switching process. Therefore, coil current measurements are widely used in today's inspection routine since it reflects conditions of various components involving in the initial stage of switching process. This condition monitoring signal is well-established and also relatively simple to measure non-intrusively by a current clamp without the need to modify the existing structure or electrical connection.

An example of open coil current recorded from two different CBs manufactured by different vendors is shown in Figure 2.7. While the overall shape varies depending on the CB type and manufacturer, certain characteristics are similar. The current rises immediately after the power supply voltage is connected and continues to increase until the first current peak. At this point, the plunger starts to move, generating an electromagnetic force inside the coil, which causes the current to decrease, until it reaches a valley. As the plunger continues its movement, it initiates the actuation of the operating mechanism. Finally, the auxiliary circuit interrupts the coil current flow, which decreases to zero eventually. More details on coil current characteristics can be found in the literature [32, 33].

2.5.2 Dynamic Contact Resistance

The dynamic contact resistance measurement inspects the resistance across CB terminals during opening and closing operations, enabling the detection of issues in the contacts [56, 37, 36, 57]. In particular, the instances of main and arcing contact separation or closing are visible and also it is an indirect evaluation of the travel curve and the wear of the arcing contacts. It is commonly used in routine time-based inspection and maintenance in substations. However, it can only be measured intrusively, when CB is disconnected from the grid, indicating that long-term continuous condition monitoring with dynamic contact resistance is not feasible.

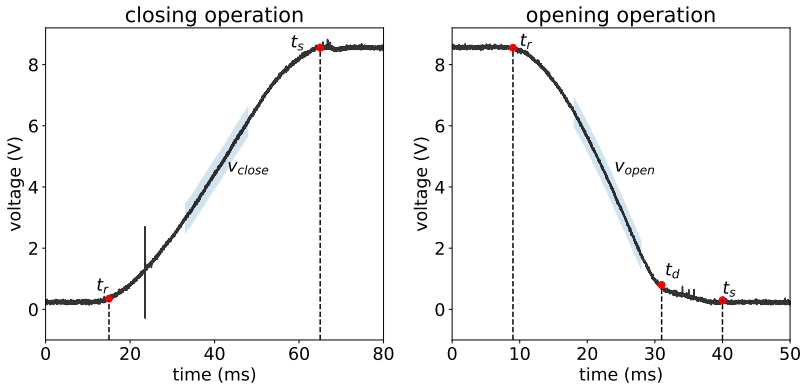


Figure 2.8: Example travel curves of opening and closing operations from an HV GCB. The positions O and C denote the open and closed positions, respectively, while the slope of the curve represents the contact travel speed. Key timing parameters marked here for assessing CB condition are detailed in Section 7.3.4.

2.5.3 Travel Curve

The travel curve tracks the movement of contacts over time and reveals potential problems with the operating mechanism or the mechanical connection to the contacts. It is typically measured with a transducer and is commonly employed during periodic, time-based inspections [58]. An example of a travel curve recorded during both opening and closing operations is shown in Figure 2.8, where $t = 0$ is when the trigger is sent. The y-axis represents the contact position, while the slope of the curve indicates the contact travel speed.

The time instant t_r in Figure 2.8 indicates the reaction time, marking the start of the CB movement, while t_s corresponds to the stop time, when the CB motion stops. For opening operations, an additional time instant t_d represents the moment when the damper is reached, resulting in a larger vibration amplitude.

Travel curves are widely used across various CB types as they capture a wide range of potential failure modes associated with the operating mechanisms and contacts. Although the travel curve is considered a useful condition indicator, continuous monitoring with travel curve sensors is often impractical due to the complexity and intrusiveness of the sensor installation requirements [58, 34, 59].

2.5.4 Operating Timing

Operating timing tests are conducted to examine the critical time parameters during opening or closing operations [60]. For instance, the time between sending a command signal and separation or touching of the arcing contacts are denoted opening time and closing time. Specifically, the opening time is defined as the duration from the trigger signal to the separation of the arcing contacts. Similarly, the closing time represents the interval from the trigger signal to the moment the contacts make contact [61].

Both opening and closing time can be determined by connecting a low-voltage DC source across the contacts, if a CB is disconnected from the grid. When the CB is in the closed position, the voltage measured between contacts equal to $0\,\mathrm{V}$, because the contacts touch each other. In contrast, when the CB is in the open position, the voltage between the contacts equals the source voltage, as the contacts are separated. An example of opening and closing time measurements is shown Figure 2.9.

Besides opening and closing times, other timing parameters such as the timing when the auxiliary switches open and closed, and the time point when contact starts to move or stop can be found depending on CB types. These timing parameters can also be found using a travel curve. These timing tests are commonly used in routine inspections, but the CB has to be disconnected from the grid.

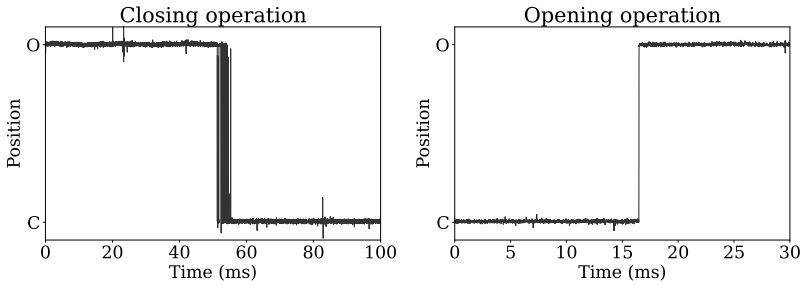


Figure 2.9: Example timing measurement of closing and opening operations from an HV CB using a low-voltage source. Positions O and C denote the open and closed positions, respectively. A low voltage across the contact can be measured in the open position, while no voltage can be measured in the closed position. In this case, the closing time is approximately $50\,\mathrm{ms}$ (with contact bouncing prohibiting precise determination), and the opening time is approximately $16\,\mathrm{ms}$.

2.5.5 Vibration and Acoustic Signals

Opening and closing operations involve movement of a large number of CB components and result in complex vibration and acoustic patterns. Therefore, recording vibration and acoustic signals can reflect potential anomalies or faults in operating mechanism [62, 23]. An example vibration and acoustic signals of an HV CB during opening and closing operations is shown in Figure 2.10, recorded from an accelerometer and a microphone.

Since vibration and acoustic sensors, such as accelerometer or microphone, can be installed without affecting the integrity or functionality of the CB. They enable continuous condition monitoring without the need to disconnect the CB from the grid. This makes them a superior alternative to traditional methods such as dynamic contact resistance or travel curve measurement, which are often intrusive and impractical for real-time or long-term condition monitoring with CBs remaining connected to the grid. However, vibration and acoustic signals are prone to be noisy, sensitive to sensor installation location, and difficult to interpret. As a result, these measurements are not yet part of routine inspections.

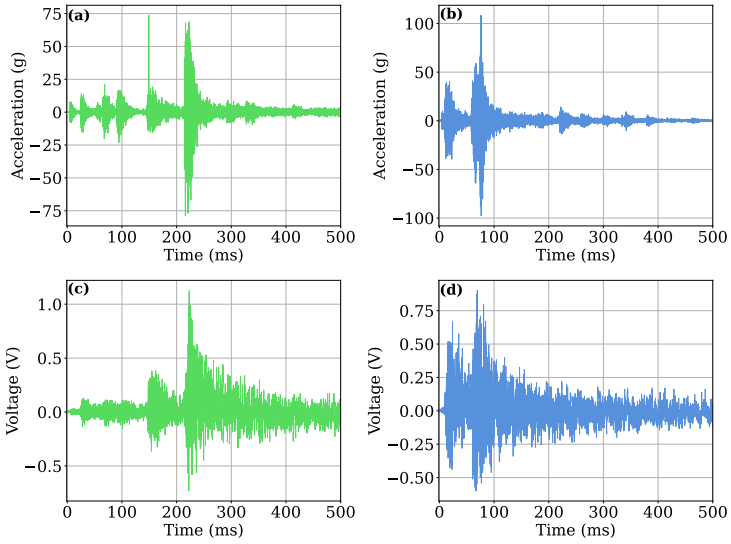


Figure 2.10: Example vibration and acoustic measurements: (a) vibration, closing operation (b) vibration, opening operation (c) microphone, closing operation (d) microphone, opening operation. Signals were measured using an accelerometer and a microphone from an HV CB in a substation.

3 Overview of Data-driven Condition Monitoring Approaches

Parts of this section are based on the publication [15].

This chapter provides a brief overview of commonly used data-driven methods for condition monitoring, applicable not only to CBs but also to other systems.

3.1 Overview

A fundamental prerequisite for applying data-driven condition monitoring is the availability of data collected from monitoring systems. It is essential to first determine which data should be collected and which sensors are necessary for capturing the important information.

Once the data is collected, the initial step is typically fault detection. This involves identifying data samples with irregular distributions that deviate from the healthy data distribution [63], indicating a potential fault condition. Once a fault is detected, the faulty samples should be further investigated and diagnosed. Traditional fault diagnostics problems are usually formulated within a supervised learning framework, where labels are available [64, 65]. However, in real-world applications, including condition monitoring of CBs, an unknown number of faults could occur and ground-truth labels are unavailable or incomplete. Therefore, fault diagnostics tasks can be reformulated into fault segmentation tasks in an unsupervised way due to the lack of labels [50]. Fault segmentation focuses on discriminating various fault types without identifying the cause of faults, e.g., which component is faulty.

The distinctions between fault detection, segmentation, and diagnostics are summarized in Figure 3.1. The interpretability level increases through these stages. Fault detection identifies samples that deviate from the healthy data distribution, fault segmentation differentiates between various fault types, and fault diagnostics provides details about specific fault causes or components involved. Each stage adds additional information and explanation about potential fault types. Notably, these processes are not sequential; condition monitoring data can serve as input to any of these stages independently, depending on the application.

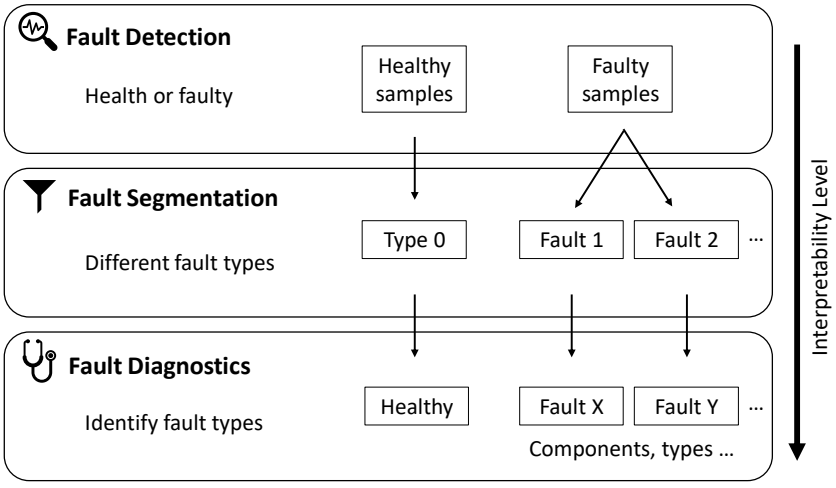


Figure 3.1: Scope of fault detection, segmentation, and diagnostics, modified from [47]. Fault detection aims to identify faulty samples from healthy samples. Fault segmentation differentiates between various fault types without diagnosing them. Fault diagnostics goes a step further by identifying the specific fault types such as identifying faulty components. Condition monitoring data can serve as input to any of these stages independently, depending on the application.

3.2 Anomaly and Fault Detection

Depending on the definition, fault detection is sometimes referred to as anomaly detection. In this work, the terms are defined in **Definitions & Terminology** and summarized as follows: not every anomaly indicates a fault, but every fault is considered an anomaly. More comprehensive discussions on fault and anomaly detection can be found in relevant review papers [4, 66].

Fault detection models can handle a wide range of input data types, such as images [67, 68] and time-series signals [69]. These models require only healthy data for training, allowing them to learn the underlying distribution that characterizes healthy conditions [66, 70]. Samples that significantly deviate from this learned healthy distribution are identified as anomalies. This approach assumes that all healthy samples are similar and are drawn from a single, consistent distribution.

These models can be either supervised or unsupervised, depending on data availability and application requirements. In practice, ground-truth fault labels are rarely available, making supervised methods difficult to apply. In addition, supervised methods require ground-truth fault labels to be complete and representative of all possible fault types. Otherwise, any unknown or unseen fault type is likely to be misclassified or not detected. To better reflect the real-word CB monitoring scenarios, this work focuses on unsupervised methods, where healthy data are assumed to be available while fault labels are rare or absent.

These anomaly detection models can be divided into several categories, including similarity-based [71], reconstruction-based [72, 73, 74], one-class classification-based [75, 76], knowledge distillation [77, 78, 67], and generative adversarial networks (GAN) [79, 80]. This work focuses on the first two categories, which are detailed below.

3.2.1 Similarity-based Methods

An effective technique for detecting anomalies, particularly in univariate time series, without the need of large dataset is similarity-based methods. These methods can also be extended to multivariate time series or even high-dimensional data such as images. The core idea is to define a similarity metric, such as Euclidean distance, to quantify the difference between a healthy sample and new incoming sample. If a new sample exhibits significant dissimilarity from the healthy sample, it is likely to be anomaly.

3.2.2 Reconstruction-based Methods

Parts of this section are based on the publication [48].

Reconstruction-based method, which uses models trained on healthy data to learn healthy data distribution, is one of the most common anomaly detection approach [4]. When anomalous data are input, these models output higher reconstruction errors compared to healthy data. Autoencoders (AE), for example, learns the distribution of input data and reconstructs the input data by encoding inputs into a latent space while preserving important information, and then decode it back to its original form [74].

3.3 Fault Segmentation

Fault segmentation aims to distinguish different fault types without requiring explicit fault diagnostics. After a fault is detected, identifying the affected component or fault type becomes essential. However, in real-world applications, ground-truth fault labels are often unavailable, making supervised methods impractical.

As a result, unsupervised clustering methods are commonly used for fault segmentation to uncover underlying fault patterns within data samples. The commonly used unsupervised clustering methods such as K-means clustering, which partitions data in to a pre-defined number of clusters K by minimizing the distance between each sample and its assigned cluster centroid. Another method ordering points to

identify the clustering structure (OPTICS) does not require a pre-defined number of clusters and instead identifies clusters based on their density and proximity. Each method offers advantages depending on the data distribution. They are useful for condition monitoring cases where no fault labels are available.

3.4 Fault Diagnostics

Once a fault is detected, the next step is fault diagnostics, where faulty samples should be further investigated and diagnosed. Traditionally, fault diagnostics is usually formulated within a supervised learning framework, where labeled data samples corresponding to the know fault types are available. In this case, the model can learn mappings between data and specific faults. Beside these models, inspecting statistical features of the faulty samples can also be used for fault diagnostics, because these features often have clear physical interpretations. Additionally, explainable artificial intelligence (XAI) methods can be applied to identify which parts of inputs contributed most to the decision of the models.

3.4.1 Explainable Artificial Intelligence

Parts of this section are based on the publication [15].

The realm of XAI addresses the well-known challenge of black-box models in machine learning, aiming to explain and understand the rationale behind model predictions, making their decision process more transparent and fostering user trust [81]. The XAI techniques can be applied to fault diagnostics for identifying potential fault types.

The explanation and interpretability are particularly crucial in high-stakes engineering applications including CBs with potential impacts on safety, availability, and costs [82, 83]. When a model is not inherently interpretable, such as linear models or small decision trees, post-hoc explainability is employed. This involves generating explanations for an already trained back-box model.

4 State of the Art in CB Condition Monitoring

4.1 Condition Monitoring on Circuit Breakers

Parts of this section are based on the publication [14].

Condition monitoring is a crucial approach to ensuring and increasing machine reliability. Effective condition monitoring signals should reflect the machine's condition, either partially or comprehensively, while the condition monitoring system itself should not affect the machine performance. Although condition monitoring systems are routinely used in various applications, such as rotating bearings and jet engines, their application is still limited in the field of CBs.

Traditional time-based maintenance strategies have long been used for CBs, where regular inspections are carried out at fixed time intervals to ensure their functionality. This approach was used in 1984 in a USA utility [84] and remains common practice today [20, 8]. However, these strategies are time-consuming and expensive [58], because CBs need to be disconnected from the grid for safety reasons, leading to longer down times. In addition, the presence of field experts on site is required [53].

During time-based inspections, various measurements are usually taken to assess CB condition. However, these assessments are performed every few years and only when the CB is disconnected from the grid. Data collected is limited to scheduled inspections rather than continuous monitoring throughout its lifetime. Since these inspections and data collected are performed only at discrete intervals, previous research has primarily focused on identifying features for distinguishing different fault types and performing fault diagnostics. However, the features effective for diagnostics might not be suitable for continuous monitoring due to varying degradation trajectories over time.

Recently, the advance in machine learning (ML) and artificial intelligence (AI) techniques, as well as the decreasing cost of sensors and data storage, has made condition monitoring of CBs increasingly feasible [85]. In contrast, implementing such a condition monitoring system for HVCBs was considered economically impractical in the 1990s [86]. As a result, utilities gradually shift from time-based maintenance strategy toward more advanced condition-based approaches, where optimal maintenance schedule can be found based on real-time condition monitoring data.

4.2 Condition Monitoring Signals of Circuit Breakers

*Parts of this section are based on the publication*s [28, 14].

As mentioned in Section 2.5, today's commonly used CB inspection and condition monitoring methods to ensure their functionality involve measuring the travel curve [34, 35], static and dynamic contact resistance [36, 37, 57], and the coil and motor current [32, 33], as well as performing timing tests [34, 59]. This section describes the literature related to measured signals used in this work including coil current (Section 4.2.1), travel curve (Section 4.2.2), acoustic signals (Section 4.2.3), and vibration signals (Section 4.2.4).

4.2.1 Coil Current

Fault diagnostics is a main focus in the literature, where features are extracted from coil current signals to distinguish between various fault types [87, 33, 32]. Since coil current signals reflect only the condition on the initial movement of the CB, they are often combined with other condition monitoring signals to enable more comprehensive condition assessments. For example, combining coil current and vibration signals has been used for fault diagnostics using CNN and self-attention mechanism [88]. Apart from fault diagnostics, RUL prediction based on coil current signals has also been explored, such as using PCA and LSTM for a VCB [89]. However, most existing studies involving coil current are limited to fault diagnostics with artificially introduced faults.

4.2.2 Travel Curve

Travel curve measurements track the movement of the contacts and are commonly used during routine inspections as part of time-based maintenance. Similar to coil current signals, most studies on travel curves focus mainly on fault diagnostics involving artificially introduced faults. For instance, five fault types were generated, and their corresponding travel curves were used to train a supervised fault diagnostics model capable of differentiating among them [90]. Similarly, another study proposes a fault diagnostics model based on simulated signals. By combining coil current and travel curves, four different artificially introduced fault types were classified [35]. As with coil current signals, the existing literature on travel curves is also limited to supervised fault diagnostics approaches rather than tracking the change of CB condition over time.

4.2.3 Acoustic Signal

Acoustic signals, specifically those captured by microphones, offer a potential way of monitoring CB condition. While these signals have been used for partial discharge detection and localization [91], research on using acoustic signals for assessing CB condition remains limited.

A key advantage of using microphone is its ease of installation, as typically no mounting on the CB structure is required, but the collected signals may be more sensitive to environmental noise compared to vibration signals. An acoustic signal recorded from a new operation was compared with a template healthy operation to detect anomalies on an HVCB [39], demonstrating the feasibility of using acoustic signals in stroke time estimation. In addition, fault diagnosis was performed using fast Fourier transform (FFT) obtained from acoustic measurements for a VCB in a laboratory and GCB in a substation [38]. A custom-built data acquisition box equipped with a microphone was used to identify different fault types, including iron core jamming, loose components, and pushing rod jamming. The data was transmitted via LoRa wireless communication, and a multi-class SVM method was applied to features extracted from the microphone signals for fault classification with an accuracy of more than 90% [92].

4.2.4 Vibration Signals

Condition monitoring of CBs using vibration signals was mentioned back in the CIGRE 1988 Session [43], but numerous problems were identified mainly because of the need to process complicated non-stationary signals. Another work from the same year concludes that using a combination of time- and frequency-domain features from vibration signals is promising for CB mechanical condition monitoring [93]. Later, a method was proposed to distinguish different artificially introduced faulty conditions on HVCBs by extracting features using vibration signals with four HVCBs from different manufacturers [94]. These preliminary vibration analysis in the 1980s conclude that vibration analysis is promising for long-term condition monitoring, capable of identifying CB mechanical faults, but requires more understanding on the collected signals.

Later in the 1990s, techniques for condition monitoring using vibration signals were extensively investigated. For example, the impact of accelerometer installation locations, attachment methods, spring load conditions, and repeatability on the collected vibration signals was investigated [95, 96]. Inspired by speech recognition tasks, similar approaches that were applied to speech recognition were applied to CB vibration. Fault diagnostics was achieved by comparing similarity between different measurements with dynamic time warping (DTW) method [96].

With the advance in computation power, works focus on more extensively searching important features as well as mode decomposition from vibration signals. For instance, more than hundreds vibration features were extracted and reduced to four-dimension condition maps for fault diagnostics, where in this work the use of Artificial intelligence (AI) was also mentioned [97]. Similarly, identifying various faulty conditions on oil and puffer CBs under both energized and de-energized cases was shown to be feasible by using vibration signals [98]. In addition to developing a fault diagnostic system, this works investigate the long-term repeatability of CBs by comparing features extracted from vibration signals [99]. It was

found that the vibration patterns can differ even among CBs of the the same model, due to variations in manufacturing and installation processes. An advanced algorithm based on DTW was proposed to detect mechanical anomalies in CB operating mechanisms [100].

Later, conventional machine learning methods such as support vector machine (SVM) and decision tree (DT) start to gain popularity. They have also been applied in the field of CB condition monitoring. For instance, one-class support vector machine (OCSVM) was used for mechanical fault diagnostics of HVCBs based on features extracted from vibration signals [101]. Wavelet analysis was applied on vibration signals with a simple neural network (NN) for classifying different fault types [102]. In addition, a modified gradient boosting-based method using time domain vibration features was proposed to distinguish different faulty conditions [42].

Deep learning became popular around the 2010s across different fields [103, 104], where models are able to learn complicated representations and discover patterns hidden in high-dimensional data. In terms of CB condition monitoring, deep learning models are suitable for non-stationary vibration signals due to their high dimensionality. For instance, time-frequency images were used as inputs to CNN for assessing the opening damper condition [105]. A combination of CNN-based U-Net and capsule network (CapsNet) [41] and a 1D-CNN with CapsNet [106] are proposed for CB mechanical fault diagnosis with a small sample size.

However, most previous CB research on vibration signals has focused mainly on fault detection and diagnostics using synthetically induced faults by recording data with multiple operations for each fault type in a laboratory. These studies typically employ a supervised binary or multi-class classification framework, with the main goal being to demonstrate that algorithms can differentiate between different fault types or between healthy and faulty states using features extracted from vibration signals. However, this approach does not permit monitoring of gradual degradation or aging over time. While fault detectability is usually the primary criterion, it does not address the ability to detect faults early, track their evolution, or even perform fault prognosis. This method can only distinguish between discrete healthy and faulty states, without capturing the evolution of degradation over time, which is an important requirement in practice.

4.3 Data-Driven Approaches for CB Condition Monitoring

Parts of this section are based on the publication [15].

Data is prerequisite for condition monitoring systems. This section details the literature on procedures after monitoring data is collected.

4.3.1 eXplainable Artificial Intelligence (XAI)

A common post-hoc XAI method is feature attribution, which assigns an importance score to each feature to explain the model's prediction. Feature attribution method can be divided into three main categories: occlusion-based, gradient-based, and propagation-based [107]. Occlusion-based (or perturbation-based) methods measure how the prediction will change if certain features are missing or corrupted [108]. Gradient-based methods [109, 110] compute the model's gradients at a given input sample with respect to each input feature. A large gradient indicates that the input feature is important for the output prediction. Lastly, propagation-based methods [111, 112] utilize propagation rules similar to the backward propagation used during neural network training to propagate the output predictions back to the input features. Attribution methods such as Class Activation Maps (CAM), Grad-CAM, Integrated Gradients, Shapley Additive explanations (SHAP), LIME and Layer-wise Relevance Propagation (LRP) have been applied to fault diagnosis based on time-domain [113, 114, 115, 116], frequency-domain [117, 118, 119] and time-frequency domain signals [120, 121, 122].

In the field of CB, the SHAP method has been applied to a CNN model with time-frequency spectrograms extracted from the vibration signals as inputs to explain the artificially introduced faults, in a supervised learning setting [123].

While these methods are overwhelmingly applied in supervised classification or regression settings, attributions can also be obtained in the cases of anomaly detection [124, 125] and clustering, using a classifier mimicking the clustering's decision boundary [126]. The present work focuses on the unsupervised setting, which has not been explored for CB applications.

Finally, there are multiple other ways to explain machine learning models. While attribution methods rely on low-level input features, decisions can be explained by higher-level concepts [127, 128]. Other types of explanation are case-based reasoning and explanation by examples, sometimes called prototypes [129, 130], and counterfactual explanations [131], *i.e.*, finding a small change that would lead to a different model outcome. For instance, the work [132] utilizes counterfactual explanations for interpretable fault diagnosis.

4.3.2 CB Condition Monitoring

Existing literature on condition monitoring for CBs primarily focuses on fault diagnostics using supervised learning, often relying on artificially introduced faults, but only limited works focus on fault detection and segmentation. These fault diagnostics studies can be categorized into three main directions: signal analysis, machine learning (ML), and deep learning (DL)-based [62]. First, the signal analysis method extracts statistical features from time-domain [42], frequency-domain, or time-frequency domain. Then, the extracted features are used to distinguish between different faulty conditions. Second, the ML-based methods utilize similar extracted features, but train classifiers to discriminate between the faulty samples. For instance, an OCSVM classifier is used with Wavelet transform features to first detect faults and then a supervised SVM classifier is trained to distinguish jam fault of the iron core, base screw looseness, and lack of lubrication [101].

DL-based methods have the advantage of the absence of a feature extraction step, where the DL algorithm is able to learn features by itself during training. For example, vibration signals are transformed into 3D time-frequency images by Hilbert-Huang transform and a 2D-CNN model is used to assess seven different damper conditions [105], or they are transformed into 2D time-frequency spectrograms by continuous wavelet transform and a deep convolutional generative adversarial network is used for data augmentation, increasing the amount of faulty samples, and a 2D-CNN model based on 2D time-frequency spectrograms is used to distinguish between different fault types [133]. A U-Net with CapsNet is proposed to identify five different fault types [41]. Attention mechanisms and few-shot transfer learning techniques are employed for CB fault diagnostics to overcome the data scarcity challenge, which arises due to CBs' infrequent operations [134].

Besides supervised experiments with artificially introduced faults, an effective strategy to monitor CB conditions is through run-to-failure experiments. The condition over time and degradation trajectories are tracked through run-to-failure experiments, which continuously monitor the system's aging and degradation processes. In these experiments, a test unit is continuously operated, with or without maintenance, until it ultimately fails. Typically, features are extracted from the recorded time-series signals, each reflecting the condition of subsystems or components. The degradation trajectory of each feature varies depending on the condition of its corresponding component and failure mode. This approach is particularly popular in bearing studies, where various run-to-failure bearing datasets [135, 12, 11] are publicly available, as well as in jet engines [136, 137]. However, in the field of CBs, only a limited number of run-to-failure experiments have been conducted in the laboratory [28, 29, 30], but none of these datasets are publicly available.

In addition, only limited work further analyzes downstream tasks such as fault detection or prognosis. For example, a CB prognostic system based on SF_6 gas density has been proposed to anticipate lockout time for CBs in substations [138]. In addition, run-to-failure tests were performed on two medium-voltage CBs in a laboratory to study mechanical failure prognosis and anomaly detection using travel curves [139]. In terms of fault prognosis using vibration signals, they were used to study degradation due to the high number of operations and detection of anomalies for fault prognosis [30]. Similarly, a long-term mechanical endurance test was performed on a high-voltage CB with more than 40 000 operations, where vibration features extracted from the first and the last operations were investigated [29].

4.4 Research Gaps

Despite over 30 years of research, CB condition monitoring systems currently deployed in substations still rely on directly observable physical parameters such as gas filling pressure, or in some cases, no condition monitoring system is used at all. The use of more advanced signals such as vibration or acoustics is not yet common practice and is not part of routine maintenance procedures in substations.

The challenges to the wider adoption of condition monitoring systems with advanced signals are due to the lower interpretability compared to traditional features, making it difficult for utilities to react when deviations are observed. In addition, the cost-benefit justification for installing such monitoring infrastructure and its own lifetime remains uncertain. Therefore, it is important to enhance the interpretability of advanced condition monitoring signals or adopt a data-driven approach that learns the distribution of healthy conditions and detects anomalies based on deviations from this healthy distribution.

In this work, several research gaps are addressed given the state-of-the-art discussed in this chapter. These main research gaps that this work aims to solve are summarized as follows and the detailed definition of the aim of this work is in Chapter 5.

Research gaps

1. Currently, no widely validated method exists that enables reliable condition monitoring systems for CBs in real-world applications.

2. Continuous monitoring of CB degradation is essential to assess condition of CBs. However, most existing studies focus on artificially introduced faults, ignoring the continuous aspect of degradation. The long-term trends of various features extracted from different condition monitoring signals, as introduced in Section 2.5, remain largely unexplored.

3. In supervised learning, ground-truth labels are available during the training process, while in practice, such labels are typically unavailable. Despite this limitation, it remains crucial to infer potential fault components or fault types without having access to labels.

4. In practical applications in substations, only non-intrusive measurement techniques are possible since the monitored CBs have to remain connected to the grid. However, it is unclear whether non-intrusive signals provide the same useful information as those obtained using intrusive methods.

5. The transferability of a condition monitoring framework from one CB to another, either from the same type or across different CB types, has not been explored.

6. Signals collected in substations typically contain higher noise levels than those collected in laboratory settings. Therefore, the feasibility and robustness of methods developed using data collected in laboratory environments must be validated with data collected in substations.

7. Developing a comprehensive CB condition monitoring framework with only limited data available that integrates advanced condition monitoring parameters and data-driven methods remains challenging due to general data scarcity and uncertain transferability between CBs and environments.

5 Aim and Structure of this Work

5.1 Aim of this Work

Based on the research gaps identified in Section 4.4, it is evident that the strong need for effective CB condition monitoring systems exists. Therefore, the aim of this work is to address these gaps and ultimately develop a CB monitor system for real-world applications. The aim of this work is summarized as follows.

Aim of this work

1. Identify sensors and key features for continuous CB condition monitoring and extract key features from non-intrusively measured signals such as vibration signals that capture degradation trajectories and compare their performance

2. Compare condition monitoring signals and extracted features collected under laboratory conditions with and without current interruption and validate the feasibility of collecting signals during the current interruption process

3. Develop a condition monitoring framework that requires only limited healthy data for training, without the need for faulty data or ground-truth fault labels, using first data collected in a laboratory and then validated on data collected in substations

4. Design and deploy data acquisition system in a substation and evaluate the transferability of the proposed condition monitoring framework from laboratory data to real-world applications with mechanical and electromagnetic noise

5.2 Structure of this Work

To develop a reliable condition monitoring framework for CBs, data is the prerequisite. Most existing methods rely mainly on datasets with artificially introduced faults, which represent discrete fault states, rather than tracking the continuous degradation of CB conditions over time. To address this gap, run-to-failure experiments were conducted in a laboratory environment without current interruption, focusing on the operating mechanism, which is the main cause of CB failure. These experiments were carried out across different types of CBs to ensure broader applicability, including two HV GCBs (**Section 6.5**), one MV VCB (**Section 6.1**), and one MV GCB (**Section 6.3**).

Besides run-to-failure experiments, this work investigates the possibility of further identifying specific fault types after fault detection, even in the absence of labeled data during the development phase. To validate this unsupervised approach, a dataset with artificially introduced faults (**Section 6.6**) was utilized. Unlike existing studies that rely on supervised learning with predefined fault types, an unsupervised method was developed. This approach better reflects the real-world conditions, where fault labels are typically unavailable and only data from healthy operations are accessible.

Based on the data collected in the laboratory, a condition monitoring framework is proposed, comprising three modules. Depending on the data availability, different modules can be applied to assess the CB condition. A requirement of applying these modules is healthy baseline data, which can be obtained from data collected immediately after commissioning or following maintenance activities.

- **Feature-based (Section 7.3)**: This module utilizes statistical features, where degradation patterns become visible if aging components influence the extracted features. These extracted features often have direct physical interpretations, enabling the identification of potentially faulty components, but domain knowledge is needed to know what features to extract and interpret the deviation. Only

a small number of healthy samples are required to establish a baseline that represents healthy operating conditions.

- **Similarity-based (Section 7.4)**: By comparing new signals against a healthy baseline, the degree of similarity or deviation between the new measurement and the healthy template is used as an indicator of CB condition. Unlike Module A, which relies on a small set of features to represent the entire recorded signals, this module utilizes the entire recording, offering a more comprehensive overview on CB health, but with reduced interpretability and higher computational requirements.
- **ML-based (Section 7.5)**: This module employs an unsupervised machine learning (ML) approach, using only healthy data during training. The goal is to detect deviations from the learned distribution of healthy conditions and to segment faulty samples into different clusters. Subsequently, faulty samples are further diagnosed with an explainable artificial intelligence (XAI) technique, providing insights into their possible causes. Unlike the first two modules, which require only a small number of healthy data samples, this module requires a large volume of data to effectively learn the healthy distribution.

The three modules are not mutually exclusive and can be used together, depending on the data availability. Details of the proposed framework, including module-specific methodologies (**Section 7.3, 7.4, 7.5**), underlying assumptions (**Section 7.1**), and limitations (**Section 7.7**), are discussed in **Chapter 7**.

To deploy the monitoring framework developed using laboratory data into real-world applications, it is essential to investigate the transferability from the laboratory environment to substations (**Section 6.8**). This includes analyzing factors that may affect signal quality such as the impact of current interruption on vibration signals and the presence of EMI commonly encountered in substations.

Ultimately, the deployment of the condition monitoring system in substations is elaborated in **Section 6.7**. A tailor-made IoT box is developed to reliably collect data in substations. It must be capable of detecting CB switching events and triggering data recording whenever the monitored CBs operate. The recorded data is then uploaded to the cloud for further analysis.

The results for applying this framework on data collected in the laboratory and in substations for each module individually and as an integrated framework are summarized in **Chapter 8**. Finally, the discussions and conclusions of the proposed condition monitoring framework are presented in **Chapter 9** and **Chapter 10**.

6 Experimental Setup and Dataset

This chapter outlines the experimental setup used to collect condition monitoring data from CBs. In total, 11 CBs with varying operating mechanisms and rated voltages are investigated. An overview of these CBs and their corresponding datasets is summarized in Table 6.1. Detailed descriptions of each CB, including its experimental setup, are presented in the subsequent sections of this chapter. For reference purposes, the CB name in Table 6.1 is utilized throughout this thesis to denote each CB.

Table 6.1: Overview of all CBs under investigation in this work. Sec.: Section number in this thesis; F?: run-to-failure (✓) or not (✗); Lab.: laboratory, Sub.: substation; Load?: with (✓) or without (✗) current interruption;

Sec.	CB Type	CB Name	F?	Where	Load?
6.1	MV VCB	VCB1	✓	Lab.	✗
6.2	MV VCB	VCB2	✗	Lab.	✓
6.3	MV GCB†	GCB1	✓	Lab.	✗
6.4	MV OCB†	OCB1	✗	Lab.	✗
6.5	HV GCBs	GCB2, 3	✓	Lab.	✗
6.6	HV GCB	GCB4	✗‡	Lab.	✗
6.7	HV GCBs	GCB5, 6, 7, 8	✗	Sub.	✓

†: CB decommissioned from a substation after decades of service
‡: artificially introduced faults

Run-to-failure experiments were conducted on selected test CBs in a laboratory environment to replicate natural mechanical aging and degradation processes, instead of artificially introducing faults. Details of run-to-failure experiments for VCB1 are provided in Section 6.1, while Section 6.5 covers the run-to-failure experimental setup on GCB2 and GCB3. The run-to-failure on GCB4, decommissioned from a substation is discussed in Section 6.3.

Four HV GCBs in a substation are monitored with vibration sensors, a microphone, and two coil current sensors, as described in Section 6.7. To compare signals under conditions with and without current interruption, data from VCB2 was collected, with its experimental setup detailed in Section 6.2. In addition, a dataset containing artificially introduced fault conditions on GCB4 was utilized to evaluate the fault segmentation and diagnostic capabilities of the proposed framework, as discussed in Section 6.6.

Each CB was equipped with different sensors, which record different signals and are summarized in Table 6.2. The selection of sensors varied across CBs, depending on the specific experimental conditions, and is detailed in the following sections in this chapter.

Table 6.2: Overview of signals collected on the CBs (✓: collected; ✗: not collected). TC: travel curve; CC: coil current; Vib.: vibration; Mic.: microphone; CS: contact separation; Aux: auxiliary switch; MC: motor current; HSC: high-speed camera. Intrusive?: measure intrusively (✓), non-intrusively (✗).

	TC	CC	Vib.	Mic.	CS	Aux.	MC	HSC
Intrusive?	✓/✗*	✗	✗	✗	✓	✗	✗	-
VCB1	✗	✓	✓	✗	✓	✗	✓	✗
VCB2	✗	✗	✓	✗	✗	✗	✗	✗
GCB1	✗	✓	✓	✓	✓	✓	✗	✗
OCB1	✗	✗	✓	✗	✓	✗	✗	✓
GCB2, 3	✓	✓	✓	✓	✓	✓	✓	✗
GCB4	✗	✗	✓	✓	✗	✗	✗	✗
GCB5, 6, 7, 8	✗	✓	✓	✓	✗	✗	✗	✗

* Travel curve sensors can be measured intrusively or non-intrusively.

6.1 MV Vacuum Circuit Breaker - Run-to-Failure

This section is based on the experimental setup section in publication [28].

The test object is an ABB VD4 Type 3612-16 spring-operated VCB with rated voltage of $36\,\mathrm{kV}$ built in 2013 intended for indoor installation in air-insulated switchgear. The spring is charged via a $230\,\mathrm{V}$ AC motor with a charging time of approximately $10\,\mathrm{s}$. The VCB can be operated manually by pressing the open and close buttons in the front panel and also by sending electric signals to the open and close coils. Figure 6.1 shows the test VCB in the laboratory with three poles arbitrarily named as pole A, B, and C.

In this work, we perform a run-to-failure experiment on the VCB without current load and without any preventive maintenance in between. The experiment starts when the spring is fully unloaded and the VCB is in its open position. A single close and open operation is performed in sequence of close-$30\,\mathrm{s}$-open-$3\,\mathrm{min}$. The experiment is controlled by the device LabJack T7 and data are recorded using TiePie digital oscilloscope. The data are recorded with sampling rate of $300\,\mathrm{kS/s}$ and length of $200\,\mathrm{ms}$.

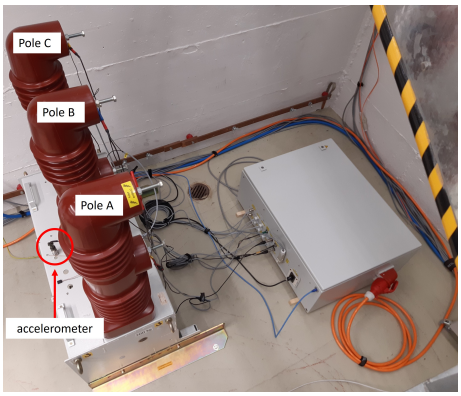


Figure 6.1: Experiment setup in the laboratory with the VCB on the left. Three poles are arbitrarily named as pole A, B, and C. The accelerometer is installed on the enclosure of the operating mechanism.

The test VCB has already performed 2442 open-close operations when the experiment started. The operation number is defined as the number of performed open operations and is shown on the counter on the front panel. The VCB experiences a fatal failure, which is caused by friction in the operating mechanism after around five months of continuous operations. In total, 26243 open and close operations are performed. For each operation, we recorded open and close coil current, opening and closing time, vibration signals, and motor charging current. The dataset is publicly available for further research activities [140].

To measure the VCB opening and closing times, a contact separation measurement is implemented. We connect a low DC voltage of $9\,\mathrm{V}$ between contacts. When the VCB is in its open position, a voltage difference can be measured between contacts. When it is in its closed position, there is no voltage difference. To prevent a short circuit of the low-voltage source in closed position, a $10\,\mathrm{k\Omega}$ series resistor is installed. This measurement is the ground-truth of closing time because it enables to infer precisely when the contacts touch each other.

To measure vibration signals, an accelerometer 786A (Wilcoxon Sensing Technologies) is installed on the drive enclosure fixed with mounting stud next to pole B because this position is close to the drive and also easy to mount as shown in Figure 6.1. It is a piezoelectric accelerometer with single direction, sensitivity of $100\,\mathrm{mV/g}$, and frequency response range of $0.5\,\mathrm{Hz}$ - $14\,\mathrm{kHz}$. This sensor is chosen because vibration signals from mechanical parts usually have a frequency lower than $10\,\mathrm{kHz}$ [141]. The recording vibration direction is perpendicular to the ground.

A thorough examination of the vibration signals revealed that the accelerometer was improperly wired, deviating from the specifications outlined in the sensor manual. This results in corrupted signals in the frequency domain and inaccurate vibration amplitude readings. Therefore, the recorded signals are

not viable for frequency domain analysis or for converting voltage readings to acceleration values using sensor's sensitivity. Nonetheless, the dataset is still suitable to investigate anomaly detection algorithms proposed in the framework of this work.

6.2 MV Vacuum Circuit Breaker - Current Interruption

The spring-operated VCB used in this experiment is part of a synthetic test circuit for thermal interruption testing [142]. An accelerometer was thread mounted on the CB to investigate the impact of current interruption on the recorded vibration signals. Unlike the run-to-failure experiments, only a limited number of load operations were performed to compare differences in vibration signals. Because current interruption is involved, only non-instructive measurements were feasible. The peak current interrupted reached approximately $2\,\mathrm{kA}$.

Trigger signals were sent simultaneously to both the CB and the TiePie oscilloscope. The vibration signals were recorded using a piezoelectric accelerometer 350C04 (PCB Piezotronics, range $\pm\ 5000\,\mathrm{g}$, sensitivity $1\,\mathrm{mV/g}$, and frequency response range of $0.4\,\mathrm{Hz}$ to $10\,000\,\mathrm{Hz}\ \pm\ 1\,\mathrm{dB}$) with a sampling rate of $120\,\mathrm{kS/s}$ and a total sampling duration of $1\,\mathrm{s}$. The accelerometer was connected to a $24\,\mathrm{V}$ DC power supply from batteries and a constant current diode J509 (Linear Integrated Systems) limiting the supply current to $3\,\mathrm{mA}$.

6.3 MV Gas Circuit Breaker - Run-to-Failure

To investigate the possibility of expanding the lifespan of CBs beyond their predefined limits set by manufacturers or utilities, a run-to-failure experiment was conducted on a decommissioned three poles medium-voltage SF_6 CB that had been in service at a substation. The spring-operated CB was manufactured by BBC in 1979 with an SF_6 filling pressure of $6\,\mathrm{bar}$ absolute and has a rated voltage of $16\,\mathrm{kV}$ and was installed in a substation for decades before being decommissioned and sent to the laboratory for testing.

The run-to-failure experiment was conduced under no-load conditions using a sequence of C-$3\,\mathrm{min}$-O-$3\,\mathrm{min}$ by sending trigger signals to open and close coils using LabJack T7. To ensure that each operation was performed with fully loaded springs, the motor was charging after every open operation, as well as every close operation. Data was recorded using TiePie digital oscilloscopes at a sampling rate of $360\,\mathrm{kS/s}$, and a sampling length of $300\,\mathrm{ms}$ (12-bit resolution). Additionally, the pressure was monitored using a PSD-4 pressure sensor (WIKA) during the entire run-to-failure process.

Two accelerometers, M352A60 (range $\pm\ 500\,\mathrm{g}$, sensitivity $10\,\mathrm{mV/g}$) and 353B14 (range $\pm\ 1000\,\mathrm{g}$, sensitivity $5\,\mathrm{mV/g}$) (both from PCB Piezotronics), with different measurement ranges and sensitivity were installed for measuring vibration signals in different locations as shown in Figure 6.2 to investigate the impact of sensor placement. Both accelerometers were supplied with $24\,\mathrm{V}$ DC power supply and constant current diodes J509 (Linear Integrated Systems), limiting the supply current to $3\,\mathrm{mA}$.

Two $10\,\Omega$ shunt resistors were installed to measure open and close coil currents. In addition, a low voltage was connected two both sides of contacts for contact separation measurement. Similarly, a low voltage source was connected to two auxiliary switches for timing measurement.

6.3.1 IoT Box

This CB was also used to test an IoT box designed for monitoring CBs in substations. The IoT box is configured to connect with four sensors: open and close coil current sensors, a accelerometer for vibration measurement, and a microphone, as shown in Figure 6.3. The sampling rate is $100\,\mathrm{kS/s}$ for vibration and microphone signals and $10\,\mathrm{kS/s}$ for coil currents with an adjustable sampling length. Further details on the IoT box is detailed in the literature [143, 144].

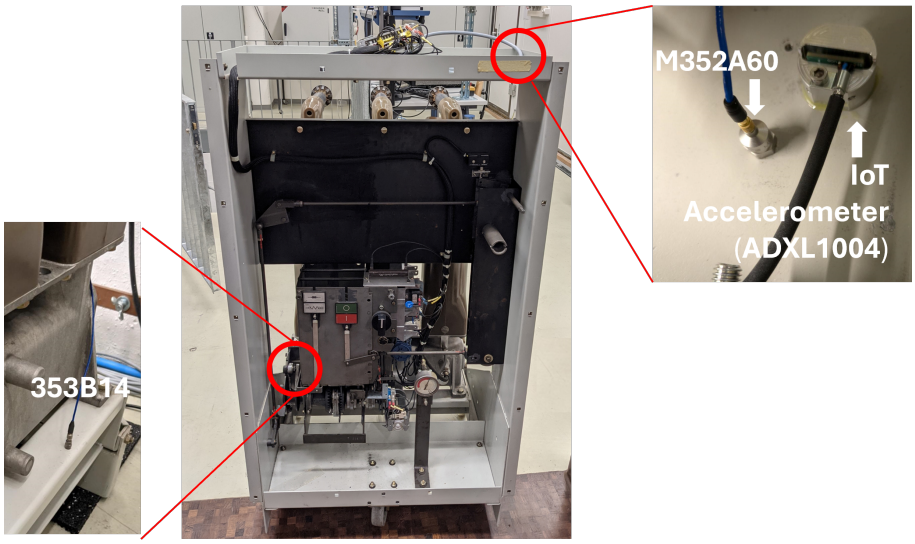


Figure 6.2: Two vibration sensors installed in different locations: an accelerometer 353B14 installed close to the operating mechanism and M352A60 on the top of the CB case.

The prototype of the IoT box was installed during the middle of run-to-failure experiments for validating the prototype with the microphone placed $40\,\mathrm{cm}$ from the operating mechanism and $40\,\mathrm{cm}$ height. Later, after the validation, the IoT box is installed in a substation, as described in Section 6.7.

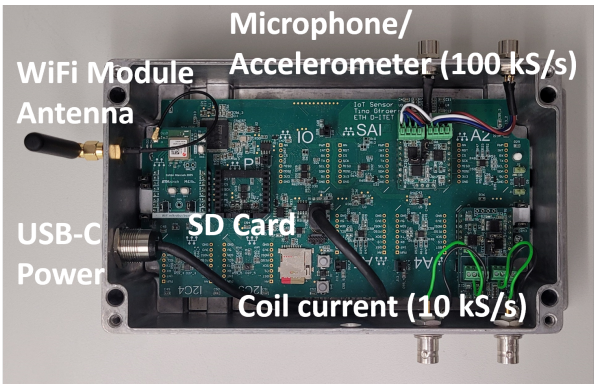


Figure 6.3: IoT box 2.0 powered by USB-C with WiFi module, SD card storage, and four sensors (microphone, accelerometer, and two coil current sensors) connected with different sampling rate.

6.4 MV Oil Circuit Breaker - High-speed Camera

The purpose of investigating this CB is to investigate the vibration signals and the corresponding movements of the CB components. Even though this CB is an oil CB, not a VCB or GCB, it was investigated due to the good visibility of the operating mechanisms. The high-speed camera was used to record opening and closing operations under high frame rate for analyzing motion of the CB.

The spring-operated MV oil CB manufactured by Sprecher & Schuh, with rated voltages of $16\,\mathrm{kV}$ had been in service for several decades before being decommissioned and transferred to the laboratory. The CB uses two separate springs: one for opening and another for closing operations. After a closing operation, the closing spring is recharged by a motor operating at $110\,\mathrm{V}$ DC, while the opening spring is automatically recharged by the mechanical motion of the closing operation.

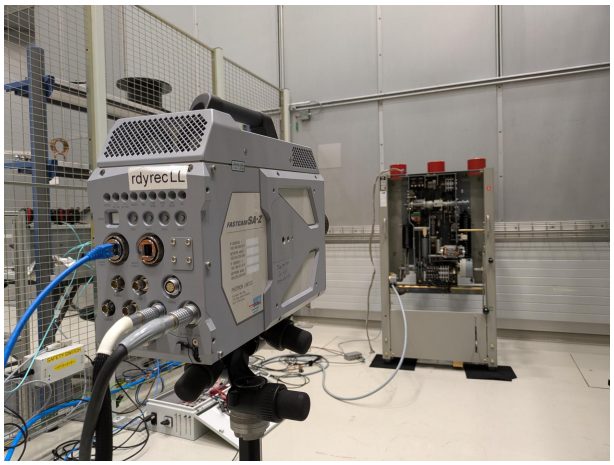


Figure 6.4: Experimental setup with a high-speed camera focusing on the operating mechanisms of the test oil CB with its front panel open for detailed observation. The components in operating mechanisms are marked in Figure 2.4.

The CB was operated with its front panel open to allow direct observation of the operating mechanisms. A high-speed camera (FASTCAM SA-Z, Photron) was used to record no-load switching operations, as shown in Figure 6.4. No run-to-failure experiment was conducted in this setup but only a few opening and closing operations. The camera was positioned approximately $3\,\mathrm{m}$ from the CB, and an accelerometer M352A60 (range $\pm 500g$, sensitivity $10\,\mathrm{mV/g}$, PCB Piezotronics) was thread mounted near the operating mechanism. The camera recorded at two frame rates: $500\,\mathrm{FPS}$ and $2000\,\mathrm{FPS}$. Due to the limited field of view of the camera, multiple switching operations were recorded, each with the camera focused on different regions of the CB to capture all relevant components.

Vibration signals were acquired with a TiePie oscilloscope at a sampling rate of $50\,\mathrm{kS/s}$ with a duration of $500\,\mathrm{ms}$. A LabJack T7 sent synchronized trigger signals to the oscilloscope, the high-speed camera, and the CB's open or close coil. This setup enabled precise frame-by-frame correlation between the recorded vibration signals and the video, allowing identification of the mechanical components responsible for distinct high-amplitude vibration events.

6.5 HV Gas Circuit Breakers - Run-to-Failure

This section is based on the experimental setup section in the publication [14].

The run-to-failure experiment was performed on two identical $300\,\mathrm{kV}$ gas-insulated CBs (GCB2 and GCB3) without any artificially introduced faults, allowing the CBs to operate until a failure occurred. However, both CBs had already undergone a significant number of operations prior to this investigation. As a result, it was anticipated that fewer additional operations would be required to reach failure compared to using new CBs. In addition, we exchanged the gas filling from $\mathrm{SF_6}$ to $\mathrm{CO_2}$, to rule out the possibility of $\mathrm{SF_6}$ leakage during the run-to-failure experiment. The operating mechanism was not modified, despite the fact that the mechanical pressure build-up inside the CBs and the resulting forces acting on the operating mechanism differ between $\mathrm{SF_6}$ and $\mathrm{CO_2}$, due to their different thermodynamic and transport properties. We expected that operating the CBs out of the specifications would lead to accelerated, yet still gradual, aging. This way, we hoped to come closer to real-life aging, compared to introducing artificial faults.

The run-to-failure experiments were conducted under no-load conditions, meaning only mechanical switching occurred and no current was interrupted. Additionally, no maintenance was performed throughout the experiment. Even though CBs are typically switched under load in substations, no-load experiments were chosen because conducting run-to-failure tests under load would cause significant erosion

of both the nozzle and contacts. This requires frequent examinations and replacements after only a few operations, depending on the current level and materials used. Furthermore, the previous work demonstrated that vibration measurements remain unaffected by the arc during the interruption process in spring-operated SF_6 CBs [145].

Both CBs were operated during regular working hours over several months, with each test series starting with the CB in its open position. On each measurement day, a series of closing and opening operations was performed, following a sequence of C-$15\,\mathrm{s}$-O-$4\,\mathrm{min}$. This resulted in idle times of four to five minutes between most operations, with occasional pauses lasting several hours to even days. To mitigate the electromagnetic noise generated when the motor starts and stops during the charging process, we installed a relay to control the motor's charging cycle. Unlike typical CBs that initiate motor charging immediately after open operations, the motor in this experiment only starts after a command is sent. In this way, we ensured that the recorded vibration signals were solely from the switching operations, without interference from vibrations caused by the motor charging process.

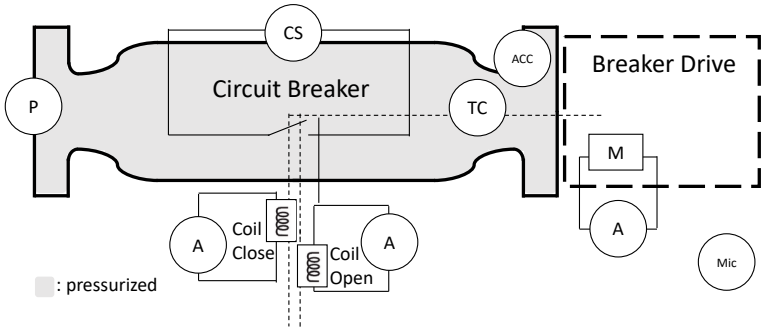


Figure 6.5: Simplified schematic of the CB run-to-failure experimental setup: for each opening and closing operation, data are collected by the installed sensors. Acc: accelerometer (vibration sensor); TC: travel curve transducer; A: current sensor (shunt or current clamp); M: motor; CS: contact separation measurements; Mic: microphone; P: pressure sensor.

The CBs were triggered using an electrical signal from a custom control box built with a LabJack T7 which sent a trigger signal to solid-state relays that controlled the CB coils, powered by a $110\,\mathrm{V}$ DC supply. The simplified schematic of the experimental setup is shown in Figure 6.5, where both CBs were configured identically. Data was recorded using TiePie digital oscilloscopes at a sampling rate of $360\,\mathrm{kS/s}$, with a sampling duration of $300\,\mathrm{ms}$, and a 12-bit resolution. The gas pressure inside CB interruption chamber was continuously monitored using a PSD-4 pressure sensor (WIKA), and the laboratory temperature was maintained within a range of $\pm 1°C$. During the experiment, the gas pressure fluctuated within a range of $40\,\mathrm{mbar}$, corresponding to the observed temperature variations. Therefore, any significant influence from pressure and temperature on the results can be excluded. Used and shown are on approximately the last 500 operations before failure for both CBs, with the operations numbered in reverse order. Operation number 0 corresponds to the failure event. The run-to-failure dataset from GCB2 is publicly available for further research [146].

An example of the first $60\,\mathrm{ms}$ and $120\,\mathrm{ms}$ signals collected during opening and closing operations, respectively, is plotted in Figure 6.6, including contact separation signals (blue), coil current (orange), vibration signals (green), and travel curves (purple). The signals are normalized for visualization purposes. The contact separation signal was measured by applying a low voltage source across the contacts. When the CB is in the closed position, the voltage between contacts drops to $0\,\mathrm{V}$, because the contacts touch each other. In contrast, when the CB is open, the voltage between the contacts equals the source voltage, as the contacts are separated. A $10\,\mathrm{k\Omega}$ resistor was added in series to the voltage source to avoid short circuit. The rated opening time for the CBs is less than $20\,\mathrm{ms}$ and the closing time is less than $55\,\mathrm{ms}$. The travel curve was measured with a transducer kit (Megger) with a $9\,\mathrm{V}$ DC supply. For measuring coil currents, two $10\,\Omega$ shunt resistors were installed - one for the open coil and the other for the close coil. Note that even though measuring current with a shunt resistor is considered an intrusive measurement method, coil current can also be measured non-intrusively with a current clamp.

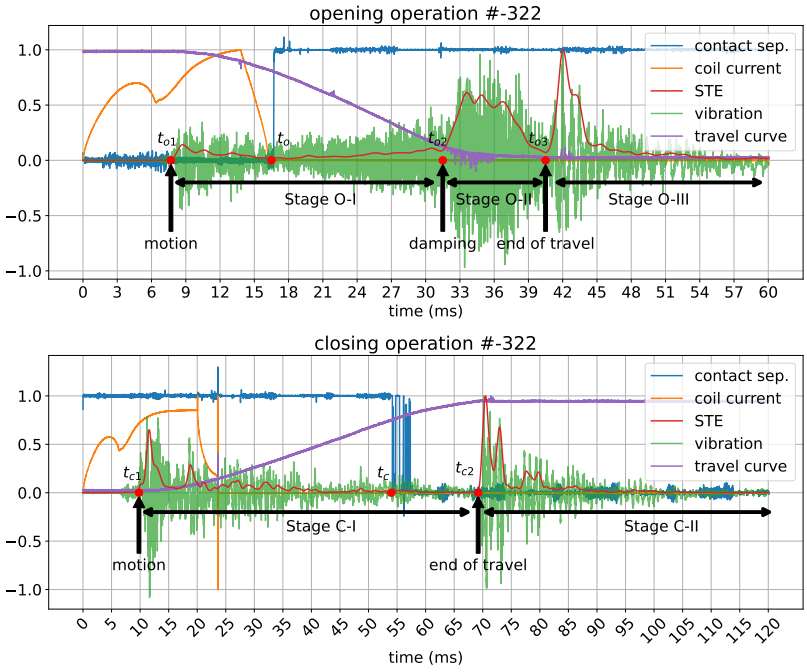


Figure 6.6: Example signals (normalized) collected during opening (top) and closing (bottom) operation # -322 (meaning 322 operations prior to failure) from GCB2, labeled with the corresponding stages and key moments, determined from the travel curve and contact separation measurement. The signals include contact separation measurement (contact sep.) (blue), coil current (orange), vibration (green), travel curve (purple), and the STE determined from the vibration signals (red). The signals are normalized for visualization purpose.

The vibration signals for GCB2 were recorded with a piezoelectric accelerometer M352A60 (PCB Piezotronics) thread mounted on the CB, as suggested in the literature, to get better signals compared to glue or magnetic mount [100]. It has a measurement range of $\pm 500\,\mathrm{g}$, sensitivity of $10\,\mathrm{mV/g}$, and frequency response range of $5\,\mathrm{Hz}$ to $60\,000\,\mathrm{Hz}$ ($\pm 3\,\mathrm{dB}$). It measures acceleration only in one direction, which is in the same direction as the direction of contact travel. The installation location was chosen with the consideration that it could be installed directly in substations without needing to disconnect the CBs from the grid. The accelerometer was powered by a $24\,\mathrm{V}$ DC supply and a constant current supply by connecting to a constant current diode J509 (Linear Integrated Systems), which limited the supply current to $3\,\mathrm{mA}$.

The measurement range of oscilloscopes for vibration signals was set to $\pm 2\,\mathrm{V}$, equivalent to $\pm 200\,\mathrm{g}$. This range was chosen based on the vibration signals recorded during the first few operations. The noise level was below $10\,\mathrm{mV}$. With a 12-bit resolution, the smallest detectable increment was approximately $0.98\,\mathrm{mV}$, which corresponds to $0.098\,\mathrm{g}$. The peak vibration amplitudes for both opening and closing operations are both around $1.3\,\mathrm{V}$ or $130\,\mathrm{g}$, below the sensor measurement range of $500\,\mathrm{g}$. Note that only the vibration recorded from GCB2 is presented in this work.

6.6 HV Gas Circuit Breaker - Fault Injection

Parts of this section are based on the publication [15].

The experimental object was an HV GCB operated by a spring-operated mechanism [147], as shown in Figure 6.7. The experiment on the CB was conducted under no-load conditions, meaning only mechanical operations without interrupting any current. To monitor the CB's mechanical dynamics, three piezoelectric accelerometers were installed in three different directions, including horizontal, vertical, and axial, between aluminum mounting bases and the surface of the spring drive structure. The mounting bases have been glued to the drive structure with LOCTITE, and the vibration sensors were tightly screwed to the mounting bases as shown in Figure 6.7 and Figure 6.8. In addition, a microphone was placed one meter from the drive. Sensor details, including model number, sensitivity, measurement range, and frequency range, are summarized in Table 6.3. The installation of these sensors does not affect the integrity or functionality of the test CB as the data are collected non-intrusively. The data were recorded at a sampling rate of $100\,\mathrm{kS/s}$ and a sampling length of $2\,\mathrm{s}$ with two National Instruments boards directly operated with the LabView environment.

Table 6.3: The four sensors used in the experiment, all from PCB Piezotronics. (Acc.: piezoelectric accelerometers; Hor.: horizontal; Ver.: vertical; Axi: axial; Mic: microphone.) The three vibration sensors were installed in three directions with respect to the operating mechanism.

Sensor	Model	Sensitivity	Range	Frequency Range
Hor. Acc.	352A60	$10\,\mathrm{mV/g}$	$\pm 500\,\mathrm{g}$	$5\,\mathrm{Hz}$ to $60\,\mathrm{kHz}$ ($\pm 3\,\mathrm{dB}$)
Ver. Acc.	M352C18	$10\,\mathrm{mV/g}$	$\pm 500\,\mathrm{g}$	$0.35\,\mathrm{Hz}$ to $25\,\mathrm{kHz}$ ($\pm 3\,\mathrm{dB}$)
Axi. Acc.	353B14	$5\,\mathrm{mV/g}$	$\pm 1000\,\mathrm{g}$	$0.35\,\mathrm{Hz}$ to $30\,\mathrm{kHz}$ ($\pm 3\,\mathrm{dB}$)
Mic.	378B02	$50\,\mathrm{mV/Pa}$	$137\,\mathrm{dB}$	$3.75\,\mathrm{Hz}$ to $20\,\mathrm{kHz}$ ($\pm 2\,\mathrm{dB}$)

It is important to note that only 'open' operations were considered in this work, as they are associated with the grid current interruption performance, and therefore, these operations are considered to be more critical. For spring-related faults, under normal conditions, 'normal' spring tension was set as per the high-voltage CB specification, while 'high spring' spring tension was increased to 110%, and 'low spring' spring tension was reduced to 90%. Similarly, for damper-related faults, the kinematic viscosity of the damper oil was modified. Under normal conditions, the kinematic viscosity was set at $200\,\mathrm{mm^2/s}$. For the faults labeled as 'degraded damper 100' and 'degraded damper 120', the kinematic viscosities were adjusted to $100\,\mathrm{mm^2/s}$ and $120\,\mathrm{mm^2/s}$, respectively.

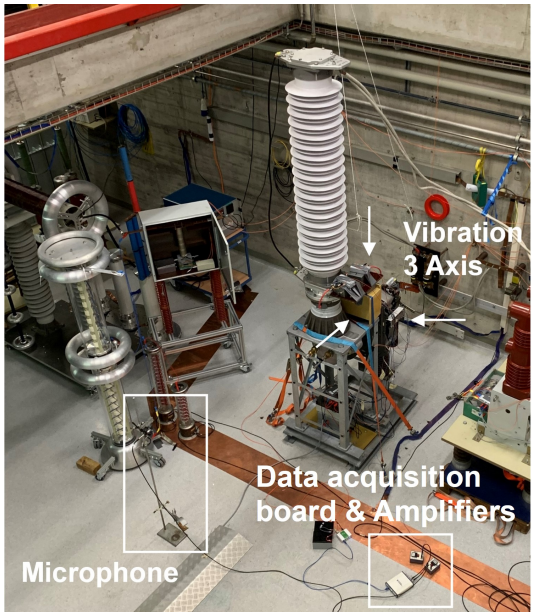


Figure 6.7: Experimental setup with the test CB, the installation location of microphone, vibration sensors, and the data acquisition board and amplifiers.

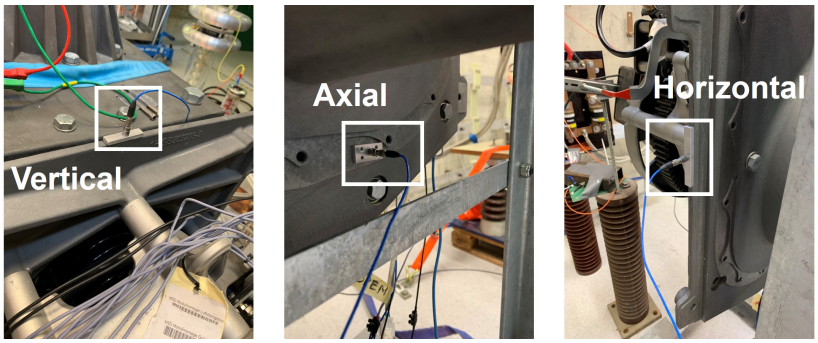


Figure 6.8: Installation locations of three vibration sensors (piezoelectric accelerometers) as depicted in Table 6.3, adhesive mounted with LOCTITE in three directions with respect to the operating mechanism.

Table 6.4: Spring and damper conditions in the dataset. Only Condition #1 is considered as healthy, while all others are faulty. Two sub-conditions from Condition #2 (nSdD100 and nSdD120) are combined into nSdD and other two from condition #5 (lSdD100 and lSdD120) are lSdD.

Condition #	Spring	Damper	Notation	# samples
1	normal	normal	nSnD	60
2	normal	degraded 100 degraded 120	nSdD100 nSdD120	30 30
3	high	normal	hSnD	96
4	low	normal	lSnD	65
5	low	degraded 100 degraded 120	lSdD100 lSdD120	29 30

6.7 HV Gas Circuit Breakers - Substation

To validate the feasibility of the proposed CB condition monitoring framework in substations, two versions of IoT boxes were installed to monitor four $132\,\mathrm{kV}$ SF_6 HV GCBs (GCB5, GCB6, GCB7, and GCB8) connected to two transformers at a substation. These CBs (two phases per bay) are operated weekly, alternating between two bays to switch the active transformer. Therefore, only magnetizing currents were present during switching, rather than the typical kilo-ampere load currents.

Non-intrusive sensors were connected to the IoT boxes, including: an accelerometer for vibration measurements (ADXL1004), a microphone for acoustic signals (IMP23ABSU), and two current clamps for measuring open and close coil currents in the control cabinet, as displayed in Figure 6.9.

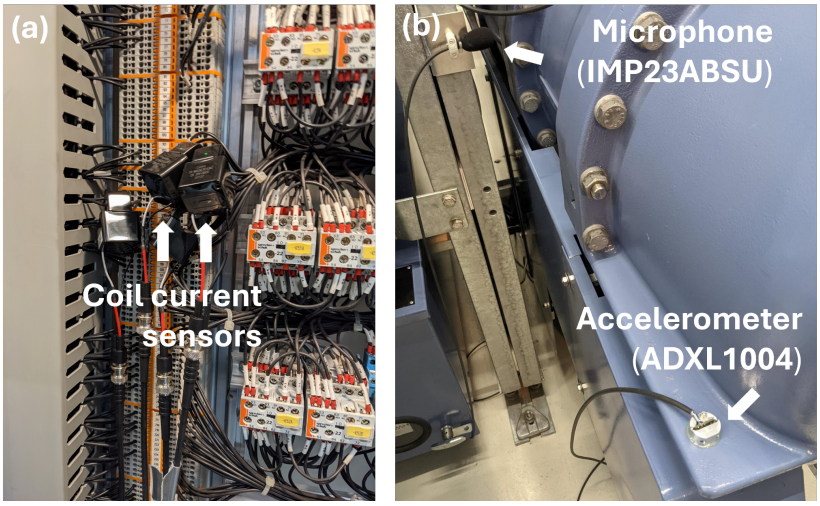


Figure 6.9: Sensors installed for monitoring $132\,\mathrm{kV}$ CBs in the substation: (a) two coil current sensors, one for open and one for close (b) microphone and accelerometer.

In the first version of the IoT box, an oscilloscope was used for data acquisition and a Raspberry Pi is used for data transmission via WiFi. Signals are collected from the sensors when the CB operates, with a trigger set to $0.2\,\mathrm{V}$ on two coil current channels. The sampling rate is set to $120\,\mathrm{kS/s}$ and sampling length $1\,\mathrm{s}$. Pre-sample ratio is set to 10% to capture the coil current before triggering, meaning $100\,\mathrm{ms}$ before trigger signals and $900\,\mathrm{ms}$ after trigger is captured. The collected data are saved locally on a USB stick and also automatically uploaded to the cloud (ETH Polybox). The overview of the experimental setup in the substation is illustrated in Figure 6.10.

Two types of cables including shielded coaxial cables (LAPP 2170000/1) and multi-wire cables with 4-pin connectors (SAC-4P-100,0-PUR/SH-0,25, Phoenix Contact 1535794) were used. While the IoT box itself (the enclosure housing, the PCB inside, and data acquisition system) is unshielded, the wiring setup ensures signal integrity. The vibration sensor and microphone are directly connected to the PCB via the multi-wire cables, whereas coil current sensors are connected using the coaxial cables. In addition, the shield of the multi-wire cables is attached to the PCB ground and connected securely to the enclosure using metallic cable clamps.

The second version of IoT box was tailor-made for CB monitoring applications and has been validated in the laboratory with MV SF_6 CB as mentioned in Section 6.3 and shown in Figure 6.3. Same sensors and cables were used for this IoT box, but instead of a USB stick for local data storage, a micro SD card is used. More details on the second version of IoT Box are discussed in Section 6.3.1.

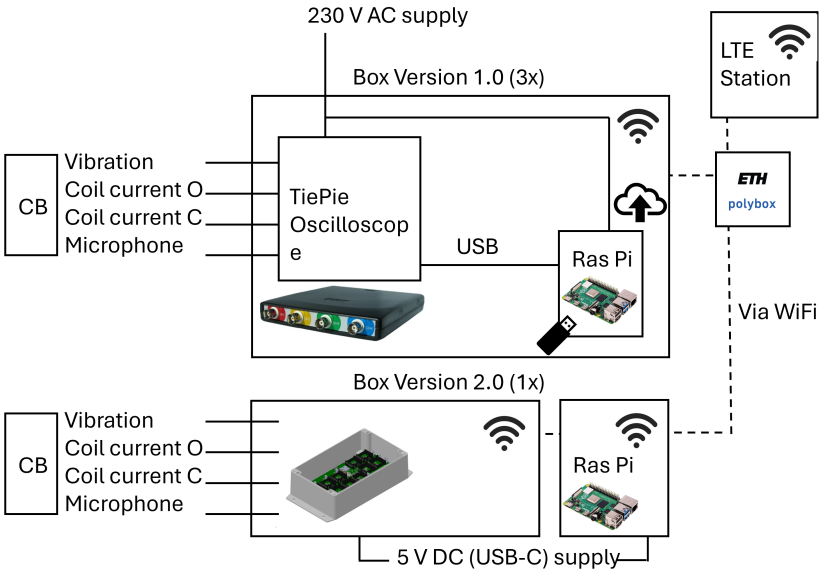


Figure 6.10: Experimental setup schematic. Dashed lines represent data transmission via WiFi, while sold lines are wired connections. When the CB switches, the box is triggered by the open or close coil current signals. Then signals from four sensors are collected and then uploaded to the cloud via WiFi. Coil current O/C: coil current open/close.

6.8 Influence of Operating Conditions

The goal of this work is to develop a condition monitoring framework assuming only healthy data available. However, the distribution of healthy data may change depending on the operating conditions. Therefore, this section investigates factors that can affect recorded signals, leading to variations even under healthy conditions. The analysis focuses on non-intrusive signals, and considers the following scenarios:

- with and without current load (Section 6.8.1),
- vibration sensor mounting position and orientation (Section 6.8.2),
- idle time between operations (Section 6.8.3),
- CB fixation (Section 6.8.4),
- spring load conditions (Section 6.8.5),
- laboratory and substation (Section 6.8.6).

6.8.1 With and Without Current Load

Several studies have investigated the influence of current load on CB vibration signals. For instance, vibration signals of a VCB operated with currents ranging from $0\,\mathrm{kA}$ to $35\,\mathrm{kA}$ were analyzed, and no apparent differences were observed [148]. Similarly, a study on a VCB during short-circuit operations with currents between $15\,\mathrm{kA}$ and $35\,\mathrm{kA}$ analyzed the vibration signals in the frequency domain and also reported no distinct changes [149].

To validate, vibration signals recorded during both opening and closing operations of a VCB used in a synthetic test circuit as explained in Section 6.2, with and without current, are shown in Figure 6.11. By visual inspection, no noticeable differences can be observed, and the extracted key moments are also

similar. Despite limited operation data, this suggests that for the VCB, the presence of current has little to no impact on vibration signals.

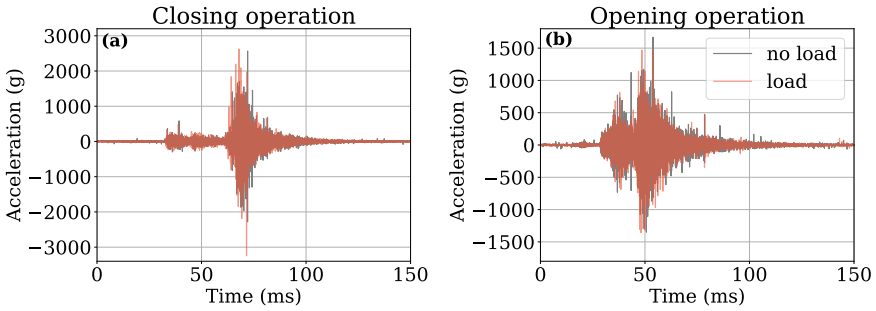


Figure 6.11: Vibration signals recorded with and without current interruption during (a) closing operation (b) opening operation, with a peak current approximately $2\,\mathrm{kA}$. No noticeable difference in key moments and vibration amplitudes can be found.

Although no significant changes are observed in VCBs, vibration characteristics may still vary depending on CB types. For instance, for GCBs, the pressure build-up during switching process changes when short-circuit current is present, which can affect vibration signals. Literature reports that in self-blast CBs, the opening speed can be reduced under load conditions due to the temporary arc-induced gas flow blockage [54]. Similarly, the travel curve of a puffer CB recorded with and without current load starts to deviate after contact separation as a result of different pressure build-up dynamics [150].

In summary, vibration patterns in VCBs appear to remain unchanged, or only slightly affected, by the presence of current. In contrast, GCBs exhibit more pronounced changes in vibration patterns due to changes in pressure build-up. For practical applications, the current level and CB type can be incorporated as an additional input to detect conditional anomaly.

6.8.2 Vibration Sensor Mounting Position and Orientation

The installed position of the vibration sensor plays an important role in determining information that can be extracted and has been analyzed for different CB types in the literature [141, 96]. The recorded vibration signals are influenced by the interaction of various CB components made from materials with different acoustic properties that affect vibrations propagation. In addition, various mounting techniques such as magnet mounting, threaded stud, and adhesive, are available and can impact the quality and characteristics of the signals [151, 23].

This section investigates the impact of vibration sensor positioning using the MV SF_6 CB dataset introduced in Section 6.3. Two accelerometers, M352A60 and 353B14 (PCB Piezotronics), were thread mounted at different positions. The accelerometer M352A60 was mounted on the top of the CB, an easily assessable location, while sensor 353B14 was placed at the bottom, near one of the poles and close to the operating mechanism, as shown in Figure 6.2. Both sensors were mounted to measure vibration signals in the same direction, perpendicular to their mounting surfaces.

The recorded vibration signals for both sensors and for both opening and closing operation are shown in Figure 6.12(a) and (b). The vibration envelopes show distinct patterns for both sensors recorded in different locations. First, the measured peak vibration amplitude on the top of CB is lower than $100\,\mathrm{g}$ for closing operation and lower than $50\,\mathrm{g}$ for opening operation. In contrast, the vibration amplitude collected from the sensor installed at the bottom closer to the operating mechanism has a peak amplitude of higher than $300\,\mathrm{g}$ for closing operation and $150\,\mathrm{g}$ for opening operation. In addition, several transient acoustics events associated with the operating mechanism movement are visible in signals recorded at the bottom. These events are damped as they travel through the CB structure to the top, making them not identifiable in signals collected by the sensor installed on the top.

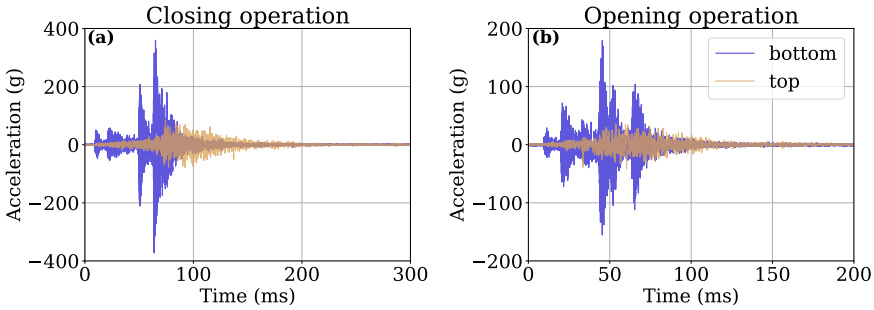


Figure 6.12: Vibration signals recorded simultaneously from accelerometers installed in different positions as shown in Figure 6.2 during (a) closing operation (b) opening operation.

In addition to sensor positions, the orientation of vibration sensors was investigated on an HV GCB by installing three sensors in different orientations, including vertical, horizontal, and axial as shown in Figure 6.8, during an opening operation under healthy conditions. The measured vibration signals are plotted in Figure 6.13 with a peak amplitude in the axial direction exceeded $500\,\mathrm{g}$, while the peaks of the other two directions remained below $200\,\mathrm{g}$. When plotted together, the three signals have similar shapes, differing mainly in amplitudes. In this case, the signals captured in axial direction appears to have the most information because of its distinct patterns, which better distinguishes key events during operating from noise. In contrast, signals in horizontal direction with the lowest amplitude of all may be limited to extract the same information.

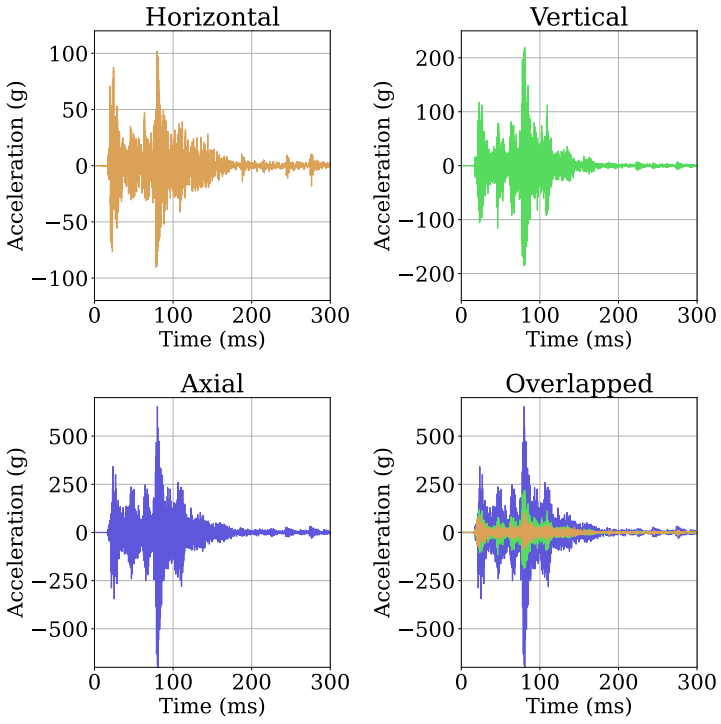


Figure 6.13: Vibration signals recorded simultaneously from three accelerometers installed in different orientations: horizontal, vertical, and axial, as shown in Figure 6.8 during an opening operation and the overlapped of the three signals to compare their shapes.

From this simple analysis, the significance of sensor position and orientation for capturing useful in-

formation is evident. Placing vibration sensors close to the vibration source, typically the operating mechanism, allows for more distinguishable transient events in recorded signals. However, close to the vibration source higher vibration amplitudes occur, requiring sensors with a high measurement range of even up to $10\,000\,\mathrm{g}$ [62] and increasing costs. Although the optimal sensor position and orientation changes depending on the type and design, a general suggestion is to install vibration sensors close to the operating mechanism while maintaining practical measurement ranges and in an orientation that has more distinct shapes with a suitable mounting surface.

6.8.3 Idle Time between Operations

Idle time refers to the interval between two consecutive operations during which the CB remains inactive. Due to the change in friction forces and the property of lubricants within moving components over time, the mechanical behavior after a longer idle time has different patterns. As a result, these operations with longer idle time can be falsely detected as anomalies. This effect is particularly pronounced in CBs with hydraulic operating mechanisms, where closing times have been observed to increase by up to $2\,\mathrm{ms}$ when the idle time is longer than $100\,\mathrm{h}$ [6].

In this section, the impact of idle time on hydromechanical spring-operated puffer CBs, as introduced in Section 6.5, is investigated. Three time-domain features, t_{c1}, t_{c2} and RMS, from closing operations are extracted, as shown in Figure 6.14. The feature t_{c1} marks the instant when the CB motion starts, t_{c2} marks the end of the contact travel (bottom of the Figure 6.6), and RMS represents the vibration energy during the closing operation.

The data from the run-to-failure experiments are divided into two groups with approximately 20 operations each based on their idle times. The first group contains operations with idle times longer than one hour, extending up to several days. The other groups are operations with only a few minutes of idle time.

A clear distinction across all three features is observed between operations with long and short idle times. Operations with longer idle time show a delayed motion start (longer t_{c1}), earlier contact stop (shorter t_{c2}), and reduced vibration energy (lower RMS) compared to operations with shorter idle times. Even though operations with long idle time show distinct vibration patterns, CB still switches reliably, which implies that the condition monitoring framework should take idle time into account to avoid false alarms.

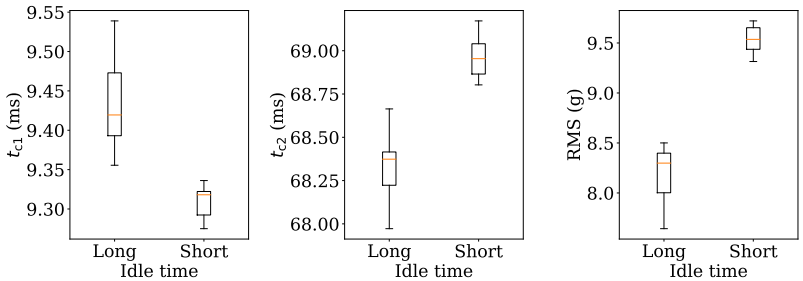


Figure 6.14: Three time-domain features, t_{c1}, t_{c2} and RMS, from closing operations under long and short idle times. The group "long" has idle time longer than one hour, while the group "short" has idle times of only a few minutes. All three features show clear difference between the groups, indicating that idle time affects CB vibration patterns.

6.8.4 CB Fixation

Change in the installation configuration of a CB can affect the measured vibration signals. This section analyzes the MV SF_6 CB introduced in Section 6.3 under two different installation and fixation conditions. First, the CB was placed freely on the floor without any fixation. Later, the same CB was fixed with

screws to the floor. The RMS of these two conditions are plotted in Figure 6.15 with 50 operations in each condition.

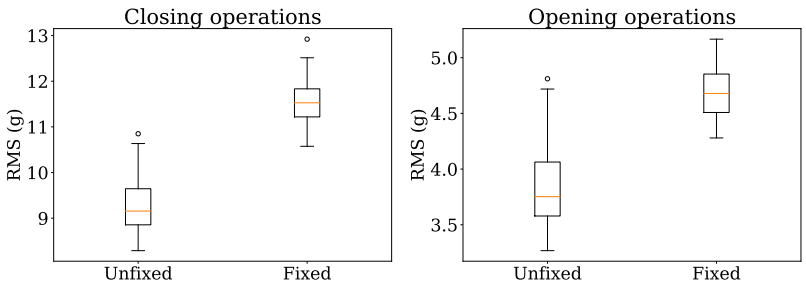


Figure 6.15: RMS of vibration signals for opening and closing operations when the CB unfixed and fixed to the ground using screws. In both types of operations, fixation results in higher RMS values compared to the unfixed condition. Each group contains 50 operations.

Fixing the CB to the floor results in higher RMS for both opening and closing operations. This suggests that if multiple CBs from neighboring bays are mounted on the same supporting frame, changes in one CB could influence the vibration signals of adjacent CBs. In addition, even for the same CB, changes in fixation methods, for instance, during maintenance work, can change vibration patterns. As a result, these operations may lead to false faults detections within the monitoring framework.

6.8.5 Spring Load Conditions

Typically CBs can perform an open-close-open (O-C-O) sequence of operations without reloading the spring between operations. However, it has been observed that the signals recorded with operations performed under different spring load conditions can have different patterns. Specifically, the second opening operation in the sequence, the one without fully-loaded spring, tends to have a longer opening time [96].

This section investigates the impact of spring load conditions on the opening operations using the MV SF_6 CB introduced in Section 6.3. A total of 12 opening operations with a fully loaded spring and 11 with a partially loaded spring were performed. Three selected time-domain features, opening time, peak, and RMS, were extracted for comparison. The distribution of these features under each condition is visualized using box plots, as shown in Figure 6.16.

Operations with a fully loaded spring exhibit shorter opening time, all below $48\,\mathrm{ms}$, whereas those with partial loaded spring have longer opening times, exceeding $49\,\mathrm{ms}$. The peak vibration values for fully loaded operations exhibit a wider range and higher mean, while partial loaded operations have lower mean peak values. In contrast, the RMS values for partial loaded operations are more scattered, showing higher variability in RMS value compared to fully loaded operations.

The spring load condition affects CB operations, influencing features such as opening time, peak amplitude and RMS of vibration signals. As a result, operations performed under different spring load conditions may be detected as anomalies, but these deviations do not indicate actual faults. To avoid such false alarms, the condition monitoring framework should account for the spring load state. This can be achieved by incorporating spring load indicators, which typically use a set of contact pins connected to a relay that automatically disconnects the motor when the spring is fully loaded. Alternatively, visual spring indicators are commonly available on the CB panel, such as the one shown in Figure 6.17 for the MV SF_6 CB.

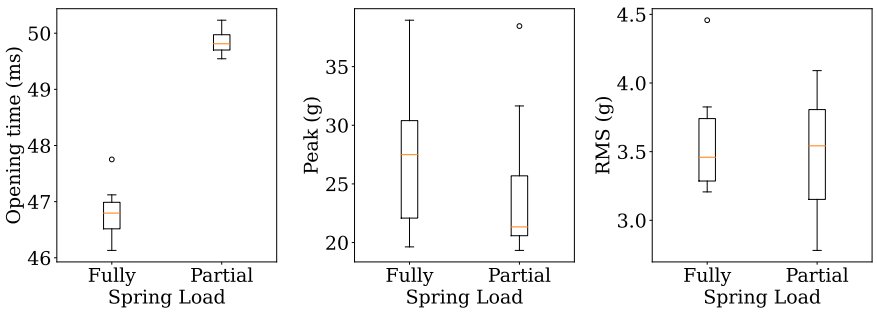


Figure 6.16: Three time-domain features, opening time, peak, and RMS for opening operations under fully and partial loaded spring conditions.

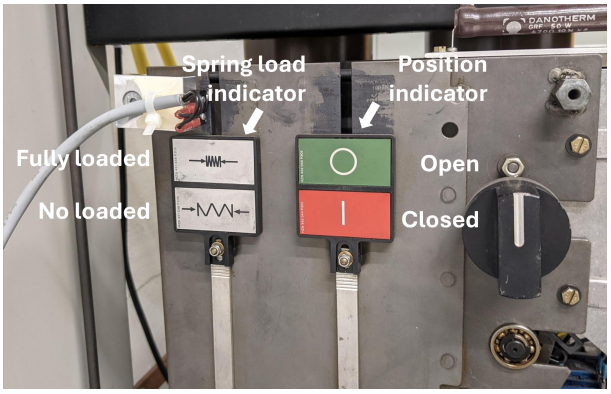


Figure 6.17: Spring load indicator and position indicator on the MV SF_6 CB introduced in Section 6.3. Typically a panel with a small window is installed for indication, as highlighted in the red rectangular box. In this case, the CB is in open position and the spring is fully loaded.

6.8.6 Laboratory and Substation

This section analyzes the signals collected in the laboratory and in the substation environments, which is typically considered to contain higher mechanical and electromagnetic noise. Based on the data collected in a substation as described in Section 6.7, we have not observed significantly higher noise levels in the substation compared to the laboratory environment. The noise level measured on the vibration signals in the laboratory is $\pm 0.37\,\mathrm{mV_{RMS}}$, while in the substation, it is $\pm 0.87\,\mathrm{mV_{RMS}}$, using the same sensors and data acquisition systems. The higher noise level in the substation is because of the measurement range setting of the data acquisition system. Due to the different vibration range of different CB, the range is set to $\pm 400\,\mathrm{mV}$ in the laboratory, whereas in the substation, it is set to $\pm 800\,\mathrm{mV}$, which inherently results in approximately twice the noise level.

While the noise levels are similar, we observed an electromagnetic interference (EMI) spike in the substation vibration signals during closing operations. The spike, which occurs after CB motion starts as shown in Figure 2.10(a), at approximately $150\,\mathrm{ms}$), may be related to the electric breakdown that initiates the current flow and was not observed during the no-load tests in the laboratory. While for the case of no-load test in the laboratory, we also observe some EMI spike caused by the inrush current of the motor when the charging process starts. Despite this difference, the performance of the proposed framework should remain unaffected by the noisy environment when sensors and data acquisition systems are properly shielded.

7 Proposed Condition Monitoring Framework

The proposed condition monitoring framework is developed based on the data collected from Chapter 6 and involves three modules: feature-based (Section 7.3), similarity-based (Section 7.4), and machine learning (ML)-based (Section 7.5). The details of the framework are discussed in this chapter.

7.1 Assumptions

The proposed monitoring framework relies on several assumptions. First, it is assumed that the initial N operations after commissioning or maintenance represent a healthy state and can serve as a baseline template for comparison. These operations are expected to have consistent and similar measured signals. It is further assumed that faulty conditions result in changes in these signals. Therefore, any deviation from the healthy baseline may indicate a potential anomaly, either due to a change of operating conditions, as described in Section 6.8, or the presence of a fault. In addition, the framework assumes that long-term changes observed in the recorded signals are attributed to degradation of the CB itself, rather than to sensor drift or deterioration of the data acquisition system.

7.2 Overview

An overview of the proposed framework is shown in Figure 7.1, which consists of three modules that are not exclusive and can be used simultaneously. The framework treats opening and closing operations separately because of their distinct operating characteristics. The selection of modules depends on the availability of healthy data from the monitored CB. It is assumed that N healthy operations data are available. A minimum number of healthy operations, denoted as N_1, is required for the framework to be applicable. When $N \geq N_1$, both feature- and similarity-based modules can be used, while for data-driven ML-based module more data (a minimum of N_2 operations, $N_2 > N_1$) are required.

Feature-based module utilizes statistical features to characterize the CB condition. This module has low computational cost and high interpretability, as each feature corresponds to a physical meaning, for example, the RMS value of vibration signals corresponds to the vibration energy. However, reducing high-dimensional time series data into a lower-dimensional feature space leads to information loss.

As a result, similarity-based module is introduced to preserve the entire recorded signal information by calculating the similarity between new measurements and healthy baseline samples. Various similarity metrics are applied not only to raw time-domain signals but also to their time-frequency representations, which are useful for non-stationary signals such as vibration and acoustic signals.

Data-driven ML-based module explores the capability of learning the distribution of healthy conditions by training ML models using solely healthy data. This module requires the highest computation cost and the largest volume of training data among the three modules. However, it offers the highest potential for recognizing complex patterns and deviation from healthy status. A comparison of module characteristics is summarized in Table 7.1.

Table 7.1: Comparison of module characteristics. F-based: feature-based; S-based: similarity-based; Green: good, Yellow: moderate, Red: poor.

Module	F-based	S-based	ML-based
Computational cost	Low	Medium	High
Complex pattern recognition	Low	Medium	High
Interpretability	High	Low	Medium
Data requirement	Low	Low	High

Each module provides an assessment of the CB condition, either healthy or anomalous. These individual assessments are then integrated into a unified evaluation of the CB condition. Note that an anomaly

indicates a deviation from the healthy condition observed before, but it does not necessarily mean a faulty condition. Such anomalies may be caused by changes in operating conditions, including variations in idle time, spring load conditions, or recent maintenance activities, as discussed in Section 6.8. To address this, an anomaly verification block is incorporated at the final stage of the framework. This component helps distinguish between true anomalies that may indicate faulty conditions, and conditional anomaly caused by changes in operating conditions.

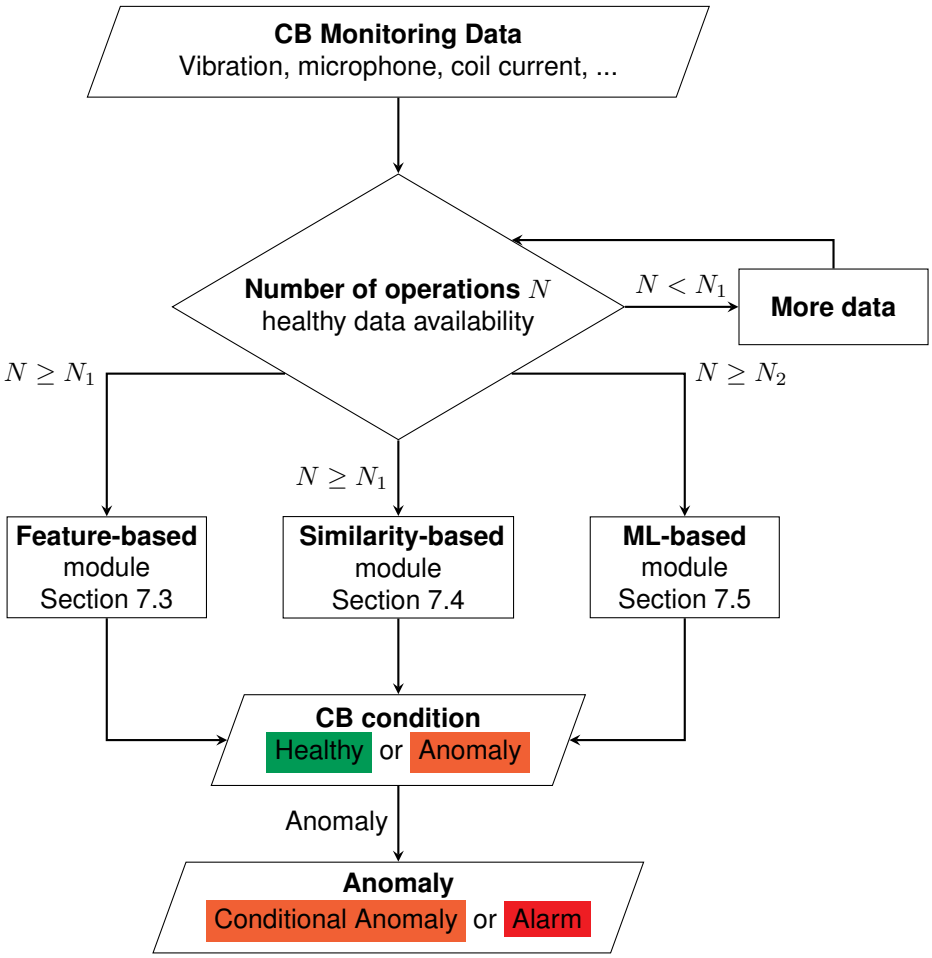


Figure 7.1: Overview of the proposed CB condition monitoring framework with three modules. Opening and closing operations are analyzed separately. When the number of healthy operations N exceeds the first threshold N_1, both the feature-based and similarity-based modules can be utilized. If N further increases beyond the second threshold N_2, the ML-based module can also be used. Conditional anomalies are anomalies caused by changes in operating conditions, as discussed in Section 6.8.

7.3 Feature-based Module

The goal of this module is to identify features that are suitable for continuous condition monitoring of CBs. These features should provide insight not only into the overall health status of the CBs but also into condition of specific components. Features can be direct physical measurements from sensors, such as gas pressure, or values calculated from the measurements such as gas leakage rate [20].

Traditionally, thresholds of some features that represent a healthy state are provided by CB manufacturer, e.g. filling pressure, number of switching operations, ambient temperature, etc.. However, thresholds for more advanced signals, such as features extracted from vibration signals, are not available as they are not commonly used monitoring parameters. Therefore, in this module, we propose using the first N_1 operations after commission or maintenance activities, assuming these operations are in a healthy state, as a baseline to define acceptance feature ranges.

The selected features, such as statistical features and timing parameters, usually offer physical interpretations of the condition of CB components and are detailed below. Additional features beyond those discussed in this section may also be explored to capture a broader range of potential failure modes, in particular when combining with domain knowledge.

7.3.1 Identification of Key Moments and Operation Stages

The key moments represent important timing events during the CB operation that provide insight into condition of various components such as springs, dampers, and contacts. These moments are extracted from the operational process and serve as critical features and timing parameters for CB condition monitoring. In this section, an example of identifying key moments on a MV OCB and an HV GCB is presented. While different CB designs lead to distinct operational characteristics, and thus different key moments, the identification procedure remains consistent across designs.

MV Oil Circuit Breaker - High-speed Camera

This section investigates the key moments in vibration signals and the corresponding CB component movements, using high-speed camera footage and accelerometer data as described in Section 6.4. Example vibration signals for both opening and closing operations and the key moments are shown in Figure 7.2(a) and (b). The associated components are identified in Figure 7.2(c), where those involved in the closing operation are marked in orange and those involved in opening operation are marked in white. The number of these components marked in Figure 7.2(c) corresponds to the number of identified key moments. For instance, the component labeled white 1 represents the open coil and latch, which operates at the key moment t_{c1} and results in high vibration amplitude.

The duration of vibration for opening operation is shorter compared to closing operation but with high amplitude above $500\,\mathrm{g}$. For closing operations, six key moments (t_{c1} to t_{c6}) are identified in Figure 7.2(a). Based on high-speed camera video, the first key moment t_{c1} around $5\,\mathrm{ms}$ corresponds to the initial movement of the closing latch, marked as 1 in orange in Figure 7.2(c). The subsequent key moments, t_{c2} and t_{c3} ($15\,\mathrm{ms}$ and $53\,\mathrm{ms}$), correspond to the rotation and stop of the connected linkages, marked as 2 and 3. The motor starts to charge the closing spring at approximately $66\,\mathrm{ms}$. Key moment t_{c4} at around $77\,\mathrm{ms}$ is associated with the stop of the linkage, marked as 4. At t_{c5} (around $90\,\mathrm{ms}$), the entire mechanism comes to a stop, resulting in the highest vibration amplitude, which is not related to a specific component and thus not shown in Figure 7.2(c). The rotation of component 6 from charging mechanism leads to a high amplitude at key moment t_{c6} around $115\,\mathrm{ms}$. The vibration signals beyond this point are caused by the motor rotating and the spring charging process and appear in a periodic pattern.

Selected frames from the high-speed camera are shown in Figure 7.3, with the top row showing a closing operation focused on the upper part of the CB and the bottom row focused on the lower part. Each row corresponds to one closing operation. In Figure 7.3(a) and (d), the CB is in the open position, with the opening spring on the left of the image discharged and the closing spring on the right of the image charged (stretched). When a command signal is sent to a close coil, the closing latch moves at

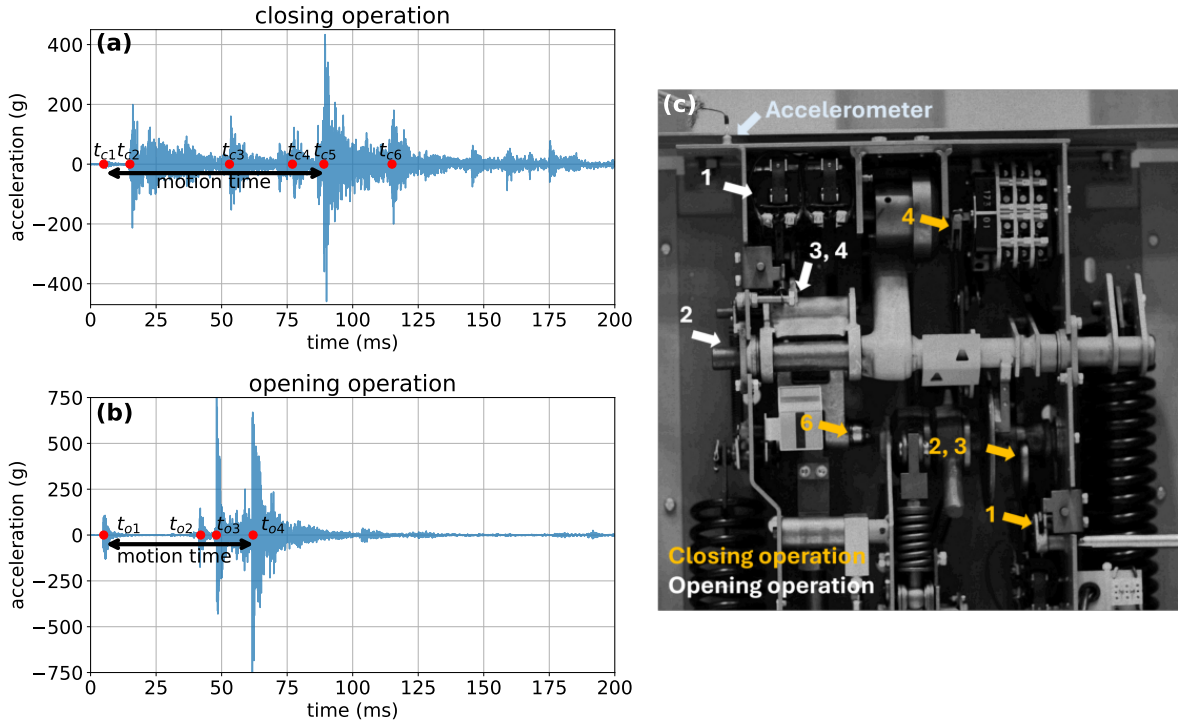


Figure 7.2: The first $200\,\mathrm{ms}$ of vibration signals recorded from (a) closing and (b) opening operations of OCB1, with their corresponding key moments identified. (c) Components marked in orange are associated with closing operations, while those marked in white correspond to opening operations. The number of these components matches the number of identified key moments, except for t_{c5} and the orange 5 (not shown in the figure), which represents the stop of CB motion rather than a single component. The accelerometer was mounted on the top of the CB.

approximately $5\,\mathrm{ms}$, and initiates the closing operation. The closing spring releases the stored energy, the closing spring shorten from Figure 7.3(a) to (c), while simultaneously charging the opening spring (stretched). In addition, the position indicator movement is visible through the rotation of the shaft from showing open (—) to close (|).

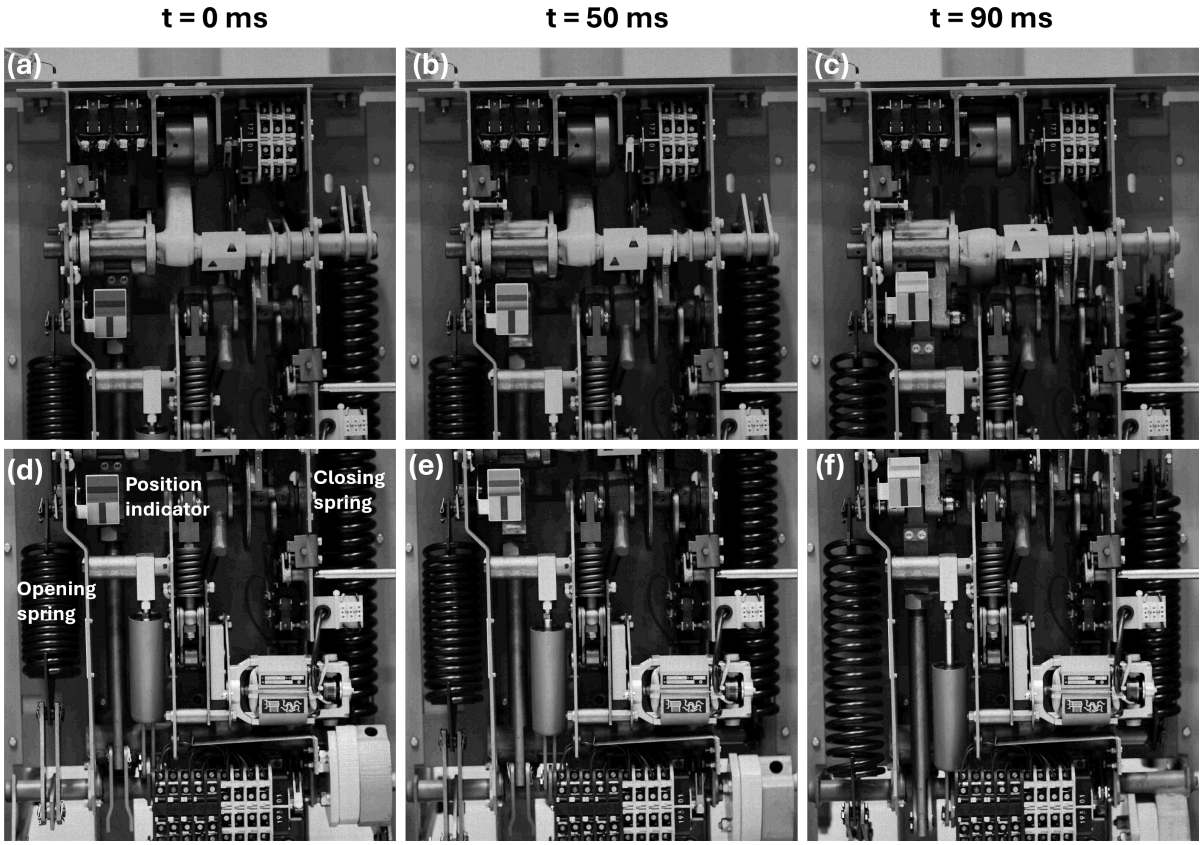


Figure 7.3: The recorded frames from the high-speed camera during closing operations. The upper three (a), (b), and (c) are from the same operation with the focus on the upper part of the CB, while the lower three (d), (e), and (f) are from another operation, focusing on the lower part. Each column corresponds to the frame from the same time, where (a) and (d) are from $t = 0\,\mathrm{ms}$, (b) and (e) from $50\,\mathrm{ms}$ and (c) and (f) from $90\,\mathrm{ms}$. The opening spring on the left of the image is charged during the closing operation, while the closing spring is charged using a motor after the closing operation. The position indicator changes from open (—) to close (|).

For opening operations, four key moments (t_{o1} to t_{o4}) are identified in Figure 7.2(b). The operating mechanisms for opening operation located mostly on the left side in Figure 7.2(c). The first key moment t_{o1} corresponds to the initialization of the open latch connected to the open coil, marked as 1 in white in Figure 7.2(c). The second key moment t_{o2} at $40\,\mathrm{ms}$ occurs when the main shaft rotates, marked as 2 in white. The third key moment t_{o3} at $48\,\mathrm{ms}$ is the upward rotation of a shaft-connected component until it hits the top. The fourth key moment t_{o4} at $61\,\mathrm{ms}$ is the counter-rotation of this component after impact. In summary, the first key moment t_{o1} reflects the condition of the open latch, while the other three can reflect the condition of the main shaft.

As with the closing operations in Figure 7.3, frames from the high-speed camera for opening operations are shown in Figure 7.4. In Figure 7.4(a) and (d), the CB is in the closed position, with both opening and closing springs charged (stretched). Two open coils are visible at the top left of Figure 7.4 (a), from where the opening operation is initiated. When an open command is sent, the open latch engages, releasing the stored energy in the opening spring and the contact separates. In Figure 7.4(e), the opening spring on the left has shorten, releasing its energy. Figure 7.4(b) shows the rectangular component above the

position indicator rotates upward, occurs around at the key moment t_{o3}.

These correlations between the vibration signals and the high-speed camera footage were established through visual, frame-by-frame inspection. As a result, the high-amplitude vibrations could originate from components outside the camera's field of view or from reflected vibrations caused by earlier events. The purpose of this section is to clarify the physical meaning of the identified key moments, as any changes in any of these moments may indicate anomalies in the CB's condition. In addition, this also allows for potential fault diagnostics to explain potential anomalies based on the vibration signals.

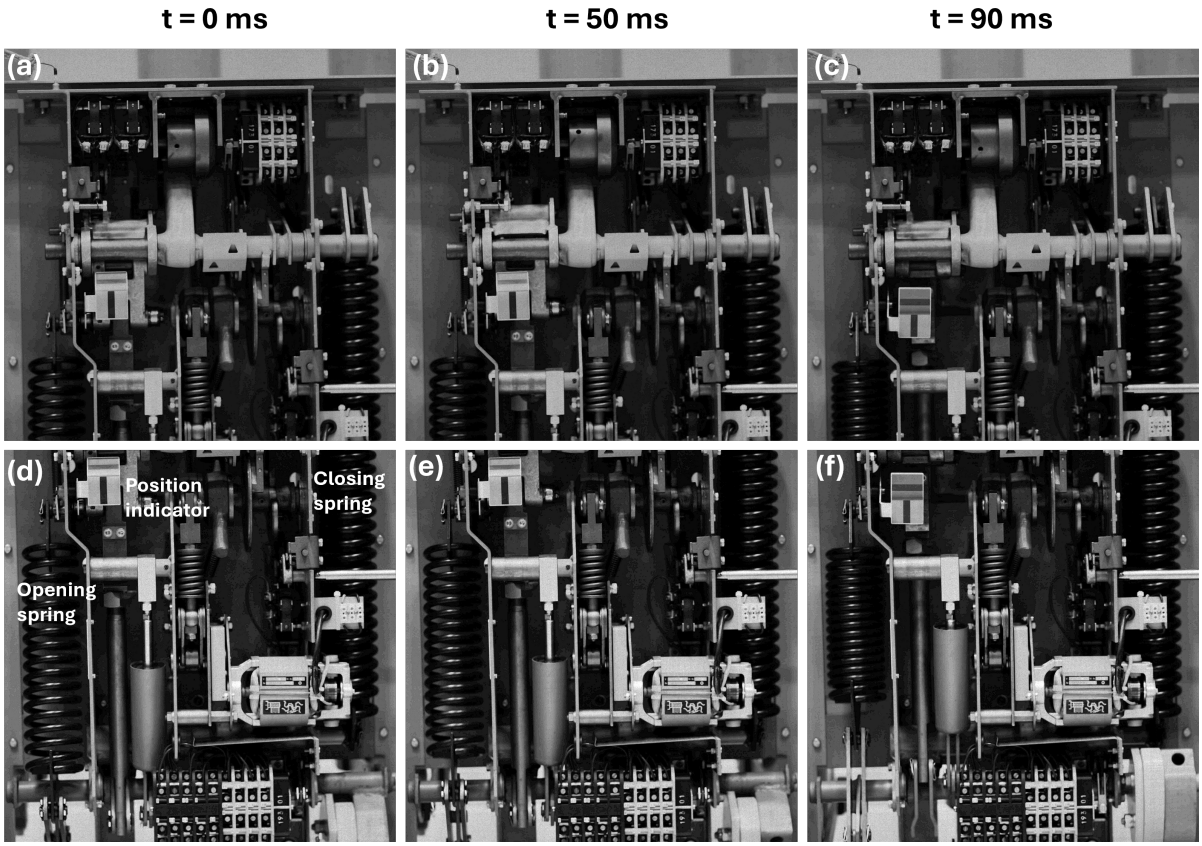


Figure 7.4: The recorded frames from the high-speed camera during opening operations. The upper three images (a), (b), and (c) are from the same operation with the focus on the upper part of the CB, while the lower three (d), (e), and (f) are from another operation, focusing on the lower part of the CB. Each column corresponds to the frame from the same time, where (a) and (d) are from $t = 0\,\mathrm{ms}$, (b) and (e) from $50\,\mathrm{ms}$ and (c) and (f) from $90\,\mathrm{ms}$. During the opening operation, the opening spring releases its energy and shortens its length, while the closing spring remains charged. The position indicator changes from close (|) to open (—).

HV Gas Circuit Breakers

Parts of this section are based on the publication [14].

Opening and closing operations can be divided into various stages based on the movement of the contacts. For instance, opening operations of an HV puffer CB can be divided into different stages: (i) the CB is in the closed position; (ii) after the initiation of the opening operation (i.e., when the trip signal is sent), the opening coil is activated, and the contacts start to move; (iii) in this stage, the main contact first separate, followed by the arcing contacts, and a switching arc is initiated. At one of the subsequent current-zero instances, the arc is extinguished, and the current is interrupted. Once the contacts have

separated sufficiently to withstand recovery voltages, the motion is decelerated by a damper, and (iv) finally, the motion stops completely.

In this work, the opening operation is segmented into three stages: motion (O-I), described as (ii) above, damping (O-II), corresponding to (iii) above, and the end of travel (O-III), corresponding to (iv) above. An example of normalized recorded signals for both opening and closing operations with various stages is depicted in Figure 6.6. The time 0 is defined as the instant of receipt of trigger command at the CB control unit (i.e., the instant of initiation of opening or closing). The decrease in the travel curve signals around $8\,\mathrm{ms}$ indicates the start of stage O-I, where the puffer volume and the tulip contacts begin to move. The initiation moment of stage O-I is marked as the first key moment t_{o1}, where the contact travel distance is around 1% of the total travel distance. During this stage, the travel curve maintains a constant slope, indicating that the contacts separate at a constant speed. The second stage, O-II, is the damping stage, starting from key moment t_{o2}, where the contacts' travel distance is approximately 90% of the full travel length. During this stage, the damper is activated, resulting in a decreasing travel speed. For example, for our test CB, the velocity drops to less than $1\,\mathrm{m/s}$ within a few milliseconds. The third stage, O-III, begins at the key moment t_{o3} and represents the moment when the contacts stop moving and reach their end position, corresponding to 99% of the stroke. At this point, the travel distance reaches its maximum, and the travel curve signal stabilizes, implying that the CB is fully open, no longer moving, and the vibration amplitude has diminished.

Conversely, the closing operation contains only two stages: motion (C-I) and the end of travel (C-II). From the travel curve depicted in Figure 6.6, the motion is initiated at around $10\,\mathrm{ms}$, denoted as key moment t_{c1}, where the travel distance is approximately 99% of the total travel distance. The slope of the travel curve, indicating travel speed, starts to increase, and the puffer and tulip contacts accelerate toward the pin contact. The second stage, C-II, begins at the key moment t_{c2} and marks the end of travel at 1% of the stroke, when the contacts stop in their final closed position. Beyond this point, the travel curve signal remains constant, and vibrations gradually die out as the closing operation is completed. To mitigate measurement noise typically present in travel curve signals, a moving average filter with a window size of 150 samples is applied to smooth the raw data.

The key moments are extracted not only from the travel curve (intrusively measured) but also from the vibration signals (non-intrusively measured). The first step involves extracting the short-time energy (STE), which effectively highlights the signal envelope and is commonly used in speech applications [152, 153, 154]. To compute the STE for a given vibration discrete-time signal $x(n)$, where n represents the number of the sampling point, the total energy E is defined as the sum of the squared signal values:

$$E = \sum_{n=-\infty}^{\infty} x^2(n). \tag{1}$$

As the name STE suggests, instead of analyzing the entire signal, it is divided into small segments. The STE is then calculated within these segments using a moving window, and is expressed as follows:

$$\mathrm{STE}(m) = \sum_{n=-\infty}^{\infty} x^2(n) w^2(m-n) \tag{2}$$

where $w(m)$ represents the window function, and m is the sample number. The choice of window function imparts different characteristics to the analysis. In this case, the Hamming window [155], which is widely used in speech recognition, is used for its fast amplitude decay outside the passband in the frequency response and its low computational cost [148]. An example of an STE signal calculated from the vibrations during opening and closing operations is plotted in red in Figure 6.6.

The key moments coincide with a sudden increase in STE signals calculated from vibration signals, caused by the acceleration and deceleration of the contacts, as illustrated in Figure 6.6. To detect these abrupt changes, a specialized detection algorithm has been developed, which is summarized in Algorithm 1. This algorithm was previously used for detecting the closing time of MV VCBs [28, 148] and

has been extended in this work for high-voltage CBs, covering both opening and closing operations, and additional key moments.

To enhance detection accuracy, the signals are truncated between n_{start} and n_{end}, corresponding to the region where the desired key moments are most likely to occur. A pre-defined sample point n_0 is used for initializing the threshold; the first threshold is calculated within the time interval from n_{start} to $n_{\text{start}}+n_0$. The algorithm continuously checks if the value of a new data point exceeds a pre-defined threshold θ, which is equal to the mean μ plus three times the standard deviation σ. If not, the new point is considered when calculating the new threshold. To reduce false positives caused by noise or spikes, the detection is considered valid only if at least L consecutive data points exceed the threshold. If a key moment is detected, the algorithm returns its timestamp; otherwise, it returns -1, indicating that no key moment was found.

Algorithm 1 Key Moments Identification Algorithm

1: $x \leftarrow x_{n_{\text{start}}:n_{\text{end}}}$
2: $n \leftarrow n_0$
3: $P \leftarrow 0$
4: **for** $n \leftarrow n_0$ to $n_{\text{end}} - n_{\text{start}}$ **do**
5: Calculate the threshold $\theta = \mu + 3\sigma$ from $|x_{0:n}|$
6: **if** $|x(n)| \geq \theta$ **then**
7: $P \leftarrow P + 1$
8: **else**
9: $P \leftarrow 0$
10: **end if**
11: **if** $P > L$ **then**
12: Key moment = $n - P$
13: go to step 17
14: **end if**
15: **end for**
16: Key moment $\leftarrow -1$
17: **return** Key moment

The first three opening and closing operations from the experiments, during which the CB was considered healthy, were used as a baseline to determine the proper range of hyperparameters for Algorithm 1.

7.3.2 Vibration and Acoustics Features

Time domain features are commonly extracted from vibration signals as indicators to characterize or to distinguish between different faults, as noted in the literature [62, 42, 156]. We consider a vibration time-series signal $x(t)$, where $0 \leq t < T$ and T is the total recording length. Two time domain features are demonstrated, as they are commonly used in vibration analysis and offer clear interpretability. The first feature is the peak, defined in Equation (3), which represents the maximum amplitude observed during the entire recording. This peak value serves as an indicator of potential shock events.

$$\text{peak} = \max(|x(t)|) \tag{3}$$

The second feature, root-mean-square (RMS), is defined in Equation (4). It reflects the energy contained within the vibration signals. In contrast to the peak, which targets localized events, RMS provides a measure of the entire vibration event, capturing the global vibration characteristics.

$$\text{RMS} = \sqrt{\frac{1}{T}\sum_{t=1}^{T} x^2(t)} \tag{4}$$



These two features are computed not only over the entire vibration recording but also for each stage of both opening and closing operations. Stage-specific features calculations offer deeper insights into the evolution of vibration characteristic, highlighting condition changes in individual CB components over time. The start and the end times for each stage are extracted from the vibration signals with STE and Algorithm 1, as shown in Figure 6.6. The end of stage C-II is set to $120\,\mathrm{ms}$, and for stage O-III to $60\,\mathrm{ms}$, because beyond these points, the vibration signals are mostly damped.

Beside these two features, more features that are commonly used for vibration analysis are considered as shown in Table 7.2, but other features are more difficult to interpret.

Table 7.2: Statistical features and the corresponding formula

#	Feature Name	Formula
0	mean	$\frac{1}{T}\sum_{t=1}^{T} x(t)$
1	peak	$\max(\lvert x(t)\rvert)$
2	RMS	$\sqrt{\frac{1}{T}\sum_{t=1}^{T} x^2(t)}$
3	kurtosis	$\frac{\frac{1}{n}\sum_{i=1}^{n}(x_i-\bar{x})^4}{\left(\frac{1}{n}\sum_{i=1}^{n}(x_i-\bar{x})^2\right)^2}$
4	skewness	$\frac{\frac{1}{n}\sum_{i=1}^{n}(x_i-\bar{x})^3}{\left(\frac{1}{n}\sum_{i=1}^{n}(x_i-\bar{x})^2\right)^{3/2}}$
5	peak to peak	$\max(x(t)) - \min(x(t))$
6	variance	$\frac{1}{T}\sum_{t=1}^{T}(x_t - \mathrm{mean})^2$
7	crest factor	$\frac{\mathrm{peak}}{\mathrm{RMS}}$
8	wave factor	$\frac{\mathrm{mean}}{\frac{1}{T}\sum_{t=1}^{T}\lvert x_t\rvert}$
9	impulse factor	$\frac{\mathrm{peak}}{\frac{1}{T}\sum_{t=1}^{T}\lvert x_t\rvert}$
10	margin factor	$\frac{\mathrm{peak}}{\left(\frac{1}{T}\sum_{t=1}^{T}\sqrt{\lvert x(t)\rvert}\right)^2}$

7.3.3 Coil Current Features

Parts of this section are based on the publication [14].

Even though coil current patterns vary from CB type to type, as shown in Figure 2.7, the extracted features remain similar. A total of seven features are extracted from the coil current signal recorded during opening operations, as shown in Figure 7.5. Since the coil current profile during closing operations is similar to that of opening operations, the same feature extraction approach is applied to both.

The coil current rises in the initial phase the power supply voltage to the coil is connected and continues to energize until the first current peak i_1 is reached. At this point, the plunger starts to move, inducing an electromagnetic force inside the coil, which causes the current to decrease, until it reaches a valley at i_2. At time t_2, the plunger keeps moving, initializing the actuation of the operating mechanism. This actuation consumes the stored energy in the drive, causing the current to increase again until it peaks at i_3. Finally, the auxiliary switch opens at t_3, cutting off the current, which decreases to zero by t_4. These features characterize conditions such as coil windings and operating mechanisms.

7.3.4 Travel Curve Features

Travel curve, as discussed in Section 2.5.3, records contact position with respect to time, and thus reflects the condition of contact. Features extracted from travel curve including contact reaction time t_r, contact stop time t_s, and the contact travel speed for open and close $v_\mathrm{open}, v_\mathrm{close}$, as shown in Figure 2.8

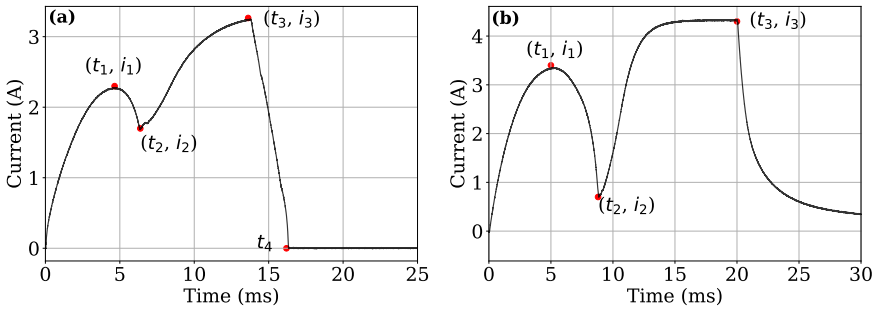


Figure 7.5: Example open coil current signals with seven features (i_1, i_2, i_3, and t_1, t_2, t_3, t_4) from (a) an HV GCB and (b) a MV GCB. The feature t_4 in the case of (b) the MV GCB is difficult to identify because it decays gradually rather than a distinct transition.

and again here in Figure 7.6 for better reference, where $t = 0$ is when the trigger signals to the CB is sent. For opening operations, an additional feature, damping time t_d, is extracted to determine the damper condition. The contact reaction time t_r is defined as the time from trigger to the time when contacts start to move. The contact stop time t_s is the time when contacts stop. The speed of contacts are calculated based on the slope of the travel curve using highlighted region in Figure 7.6.

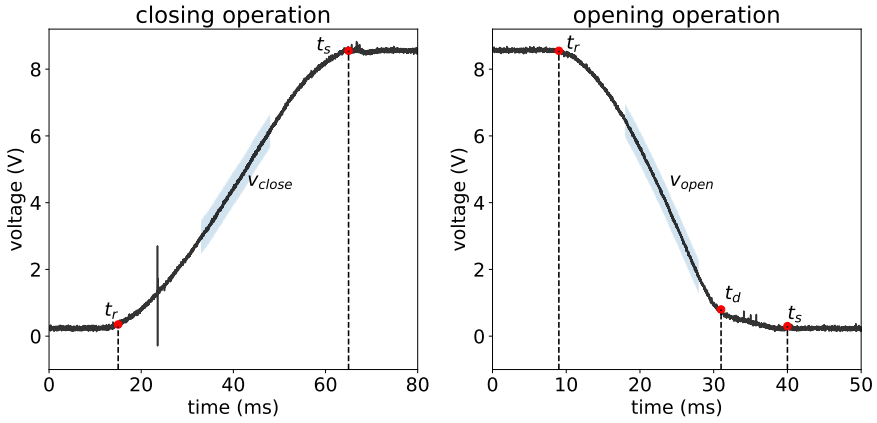


Figure 7.6: Example travel curve signals with corresponding features from an HV GCB. t_{r}: reaction time, t_{s}: stop time, t_{d}: damping time, v_{close}: closing speed, v_{open}: opening speed.

7.3.5 Motor Charging Time

In spring-drive CBs, a motor recharges the spring after each operation to prepare for the next operation. Monitoring the motor charging time can therefore provide insight into the condition of both the motor and potentially also the spring. To measure this charging time, a low-cost microphone MAX4466 was used.

An example of a recorded microphone signal for a charging process is shown in Figure 7.7 and the charging duration to be calculated. Alternatively, EMI spikes caused by motor starting and stopping can be used to estimate the charging time.

7.3.6 Operating Timing Features

Parts of this section are based on the publication [14].

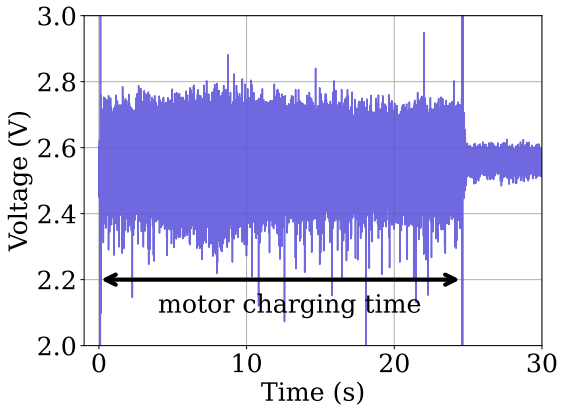


Figure 7.7: Example of motor charging signals recorded with a low-cost microphone, showing a charging time of approximately $25\,\mathrm{s}$. The charging time can be calculated by segmenting the interval from higher to lower signal levels.

Operating timing features including opening time, t_o, and closing time, t_c. If the CB is disconnected from the grid, these two time parameters can be determined with a low-voltage source as shown in blue in Figure 6.6. However, it is an intrusive measurement method and not feasible when the CB is connected to the grid. The opening time t_o and closing time t_c presented in this work are obtained from the contact separation measurement as the experiment is performed under no-load condition.

Similar to the opening and closing time, the opening and closing instants of auxiliary switches can also be used as features for monitoring the condition of CBs. Similarly, these timings can be measured with a low-voltage source. The primary function of auxiliary switches is to indicate the CB position. While this measurement does not directly capture the exact opening and closing time, it provides an indirect estimation. Since auxiliary switches are typically connected indirectly via some linkage mechanism to the contact, this measurement can be done non-intrusively, depending on the CB design. Besides the opening and closing times and the auxiliary switch timing, the key moments described in Section 7.3.1 are also consider as operating timing features in this work.

7.4 Similarity-based Module

Parts of this section are based on the publication [14].

This similarity-based module assesses the condition of CB by comparing newly acquired signals with a set of healthy template signals. It is assumed that the first few operations after commissioning or maintenance are in a healthy state and can serve as reference templates. Another assumption is that the data are time-synchronized, meaning that recordings should always start at the same reference point, typically a trigger signal sent from a control unit.

A greater deviation from these healthy templates may indicate potential degradation or anomalies. Unlike the feature-based module, this module leverages the entire high-dimensional time series or time-frequency spectrograms, rather than using only a limited number of features to represent the whole signal.

To quantify the similarity between two operations, various metrics that capture different aspects of the data are proposed. These metrics are divided into two categories: the first focuses on finding similarity directly between time series signals, while the second evaluates similarity in the time-frequency representations.

7.4.1 Time Series Similarity

For one-dimensional time series similarity, the inputs are time series signals recorded from sensors such as vibration or acoustic data. Given a time series signal $x(t)$, a straightforward approach to measuring similarity is to compute the point-by-point difference using Euclidean distance. Assuming the query signal $\boldsymbol{x_q}(t)$ and the healthy reference signal $\boldsymbol{x_h}(t)$ are synchronized and share the same sampling rate, their similarity can be expressed using Euclidean distance as:

$$\mathrm{S_E}(\boldsymbol{x_q}(t), \boldsymbol{x_h}(t)) = \sqrt{\sum_{t=1}^{T} (\boldsymbol{x_q}(t) - \boldsymbol{x_h}(t))^2} \tag{5}$$

where T is the recording length.

The similarity can also be calculated with cosine similarity, which measures the similarity between two vectors. It is defined in Equation (6), where the numerator represents the dot product of the two vectors and the denominator is the product of their magnitudes. In this case, time series signals are treated as high-discretional vectors. The cosine similarity ranges from -1 and 1, where 1 indicates perfect similarity, 0 implies orthogonality between the two vectors, and -1 means two vectors are in opposite directions.

$$\mathrm{S_C}(\boldsymbol{x_q}(t), \boldsymbol{x_h}(t)) = \frac{\boldsymbol{x_q}(t) \cdot \boldsymbol{x_h}(t)}{\|\boldsymbol{x_q}(t)\| \|\boldsymbol{x_h}(t)\|} \tag{6}$$

Due to the highly non-stationary characteristics of vibration or acoustic signals, pre-processing methods such as filtering or smoothing are recommended to achieve a more reliable quantification result. In contrast, for signals with lower frequency content, such as coil current or travel curves, such pre-processing is not needed.

7.4.2 Spectrogram Similarity

Several metrics have been proposed to quantify the similarity between images [157] such as mean square error (MSE) and structural similarity index measure (SSIM) [158]. In this case, instead of taking the one-dimensional time series, a two-dimensional time-frequency spectrogram is used as input, meaning that the frequency domain information is also considered.

First, the pixel-wise MSE is used to quantify the spectrogram similarity, averaged over the entire spectrogram. Assuming a spectrogram has dimensions $d_f \times d_t$, where d_f is the number of frequency bins and d_t is the number of time bins, the pixel-wise MSE between the query new spectrogram $\boldsymbol{M_q}$ and the healthy spectrogram $\boldsymbol{M_h}$ is calculated as:

$$\mathrm{S}_{\mathrm{MSE}}(\boldsymbol{M_q}, \boldsymbol{M_h}) = \frac{1}{d_f d_t} \sum_{i=1}^{F} \sum_{j=1}^{T} \left(\boldsymbol{M_q}(i,j) - \boldsymbol{M_h}(i,j)\right)^2 . \tag{7}$$

The MSE between two spectrograms can potentially be used for fault diagnostics by identifying the time-frequency region that shows high deviations. These regions are likely to be related to the faulty components.

Besides MSE, SSIM is introduced to measure the similarity in terms of human visual perception [158]. Unlike MSE that estimates pixels independently, it considers the inter-dependencies between pixels. In addition, SSIM also considers luminance, contrast, and structure. The mean intensity of a given spectrogram $\boldsymbol{M}$ is:

$$\mu_M = \frac{1}{N} \sum_{i=1}^{N} \boldsymbol{M_i}, \tag{8}$$

where N is the total number of pixels. Similarly, the variance σ_M^2 is:

$$\sigma_M^2 = \frac{1}{N} \sum_{i=1}^{N} (\boldsymbol{M_i} - \mu_M)^2. \tag{9}$$

The SSIM between the query and the healthy spectrograms $\mathrm{SSIM}(\boldsymbol{M_q}, \boldsymbol{M_h})$ can be written as:

$$\mathrm{SSIM}(\boldsymbol{M_q}, \boldsymbol{M_h}) = \frac{(2\mu_x\mu_y + C_1)(2\sigma_{xy} + C_2)}{(\mu_x^2 + \mu_y^2 + C_1)(\sigma_x^2 + \sigma_y^2 + C_2)} \tag{10}$$

where C_1 and C_2 are constants added to avoid instability when $\mu_x^2 + \mu_y^2$ or $\sigma_x^2 + \sigma_y^2$ is close to zero. Commonly used values are $C_1 = 0.01$ and $C_2 = 0.03$, which are also used in this work.

Table 7.3: Similarity metrics and signals used for the similarity-based module. TC: travel curve, CC: coil current, vib.: vibration, mic.: microphone.

Metrics - time series	TC	CC	vib.	mic.
Euclidean distance	✓	✓	✓	✓
Cosine similarity	✓	✓	✓	✓
Metrics - spectrogram	**TC**	**CC**	**vib.**	**mic.**
MSE	✗	✗	✓	✓
SSIM	✗	✗	✓	✓

7.5 Machine Learning-based Module

Parts of this section are based on the publication [15].

When more data are available ($N > N_2$), the ML-based module can be utilized, which consists of three steps as shown in Figure 7.8. The first step is to train a convolutional autoencoder (CAE) for fault detection, which learns the healthy data distribution. In the second step, fault segmentation, samples are grouped into various clusters, and the pseudo-labels are created. In the third step, an additional classifier is trained with the pseudo-labels obtained from the fault segmentation step for XAI-guided fault

diagnostics to provide explanations for the segmented faults, supporting domain experts in diagnosing different fault types.

7.5.1 Convolutional Autoencoder (CAE)

The time-series vibration or acoustic signals are first converted into time-frequency spectrograms $\boldsymbol{x}$ as inputs to the convolutional autoencoder (CAE). Given a training dataset $\mathcal{D}_{\text{train}} = \{\boldsymbol{x}_0, \boldsymbol{x}_1, \ldots, \boldsymbol{x}_N\}$ consisting of $N+1$ healthy time-frequency spectrograms, the objective is to learn the distribution of healthy data and detect faults in the test dataset $\mathcal{D}_{\text{test}}$, which may contain both healthy and faulty data. The CAE, a variant of the vanilla autoencoder (AE), is commonly used for tasks such as signal denoising and dimensionality reduction. Unlike the vanilla AE, which uses fully-connected layers, the CAE employs convolutional layers. As illustrated in Figure 7.8, the CAE consists of two main components: the encoder $E_{\theta_e}(\cdot)$ and the decoder $D_{\theta_d}(\cdot)$. The parameters θ_e and θ_d represent the model parameters of the encoder and the decoder, respectively. The encoder compresses the input data into a latent space while retaining essential information, and the decoder reconstructs the original data from these latent features. The CAE is trained on the healthy data to minimize the loss $\mathcal{L}_{\text{CAE}}$, defined as:

$$\mathcal{L}_{\text{CAE}} = \frac{1}{N+1} \sum_{i=0}^{N} (\boldsymbol{x_i} - \hat{\boldsymbol{x_i}})^2 \tag{11}$$

where $\hat{\boldsymbol{x_i}}$ is the reconstructed spectrogram from the training sample $\boldsymbol{x_i}$, and both $\hat{\boldsymbol{x}}_i$ and $\boldsymbol{x}_i$ share the same dimensions:

$$\hat{\boldsymbol{x_i}} = D_{\theta_d}\left(E_{\theta_e}(\boldsymbol{x_i})\right). \tag{12}$$

7.5.2 Fault Detection and Segmentation

The fault is detected by calculating the residual (reconstruction error) based on the CAE trained solely on healthy data, which means that any deviation from healthy results in a higher residual. Consider an input spectrogram $\boldsymbol{x_i} \in \mathbb{R}^{H \times W \times C}$, where H is the spectrogram height, W the width, and C is the number of sensors. The residual $\boldsymbol{r_i}$, which has the same shape as the input spectrogram, is defined as:

$$\boldsymbol{r_i} = \boldsymbol{x_i} - D_{\theta_d}(E_{\theta_e}(\boldsymbol{x_i})) = \boldsymbol{x_i} - \hat{\boldsymbol{x_i}} \tag{13}$$

where $\hat{\boldsymbol{x}}_i$ is the reconstructed spectrogram.

The fault detection identifies faults as samples with residuals exceeding a pre-defined threshold τ. This threshold is calculated based on the residual of the healthy samples in the training dataset $\mathcal{D}_{\text{train}}$, specifically using their mean μ and standard deviation σ, as described in Equation (14):

$$\tau = \mu + 3\sigma. \tag{14}$$

In our case, the residual $\boldsymbol{r}$ has dimensions $H \times W \times C$. To represent the residual for each sample, we calculate an average over all dimensions, as defined in Equation (15). A fault in the test dataset $\mathcal{D}_{\text{test}}$ is detected when $\bar{r} \geq \tau$.

$$\bar{r} = \frac{1}{HWC} \sum_{j=1}^{H} \sum_{k=1}^{W} \sum_{l=1}^{C} |r_{jkl}| \tag{15}$$

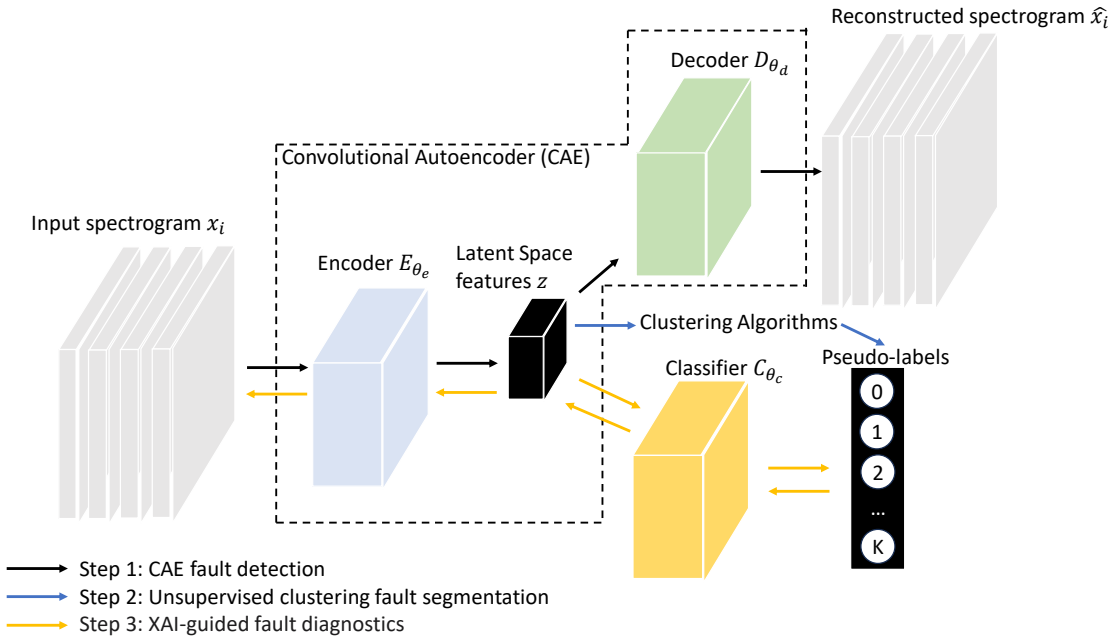


Figure 7.8: Overall proposed framework. In step 1 (fault detection), a convolutional autoencoder (CAE) is trained on the training dataset $\mathcal{D}_{\text{train}}$ containing only healthy data. The discrepancy between the input and reconstructed spectrograms is used to detect faults in the test dataset $\mathcal{D}_{\text{test}}$. In step 2 (fault segmentation), the latent space features in the test dataset $\mathcal{D}_{\text{test}}$ are clustered using clustering algorithms, creating corresponding pseudo-labels. In step 3 (fault diagnostics), an additional classifier $C_{\theta_c}(\cdot)$ is introduced to identify potential fault types based on cluster explanations and is trained using the input latent space features with the generated pseudo-labels as targets. An XAI method is applied to trace the output predictions back to the input spectrograms, providing interpretability and enabling the identification of potential fault types by domain experts.

where H is the spectrogram height, W the width, and C is the number of sensors. Note that a fixed threshold is used here under the assumption that CBs are operated infrequently, unlike industrial bearings or jet engines, and thus the healthy condition remains stable over time. Factors such as environmental conditions or interrupted current levels are more likely to influence the distribution of healthy data. For instance, seasonal temperature fluctuations can affect the gas pressure inside CB interruption chambers, thereby impacting contact motion. However, the deviations from faulty to healthy samples are higher than from healthy to healthy under different operation conditions. One way to cope with these deviations within healthy conditions is to include these conditions (such as room temperature, gas pressure, and interrupted current level, etc.) as input features in the framework, allowing the healthy distribution to be dynamically adjusted.

The fault segmentation is achieved through unsupervised clustering methods. It is important to note that the proposed framework is generic and can be used with any clustering method. In this work, we will demonstrate the approach using K-means clustering, density-based algorithm OPTICS (Ordering Points To Identify the Clustering Structure) [159], and SOM (Self-Organizing Maps) [160, 161]. The number of clusters only has to be specified explicitly for K-means but not for the other two methods. The inputs to the clustering methods are the latent space features $\boldsymbol{z_i}$ extracted from the trained CAE, as they provide a compressed representation of the input signals. These features, $\boldsymbol{z_i}$, can be represented as:

$$\boldsymbol{z_i} = E_{\theta_e}(\boldsymbol{x_i}). \tag{16}$$

where $E_{\theta_e}(\cdot)$ is the encoder. The dimensionality of these latent space features is a hyperparameter and can vary depending on the specific application.

7.5.3 XAI-guided Fault Diagnostics

In this step, an attribution-based XAI method is leveraged to generate explanations for each of the resulting clusters. We have adopted the Integrated Gradients (IG) technique in this work because it satisfies two desirable theoretical properties known as completeness and implementation invariance [162]. However, any other XAI technique may be used in our proposed framework.

IG aims to explain model predictions by computing gradients [110]. This method requires a baseline input, typically a black image for image attribution, representing the absence of features contributing to the output. Images are linearly interpolated between the baseline and the input image. Gradients are computed along this path to quantify the relationship between changes in pixel values and changes in the model's prediction. As a result, pixels that contribute more significantly to the model's prediction exhibit higher gradient values.

Typically, XAI is applied in supervised learning settings, where attribution is calculated from the prediction outputs to input features. However, in our unsupervised learning framework, we only have samples with healthy labels from the training dataset $\mathcal{D}_{\text{train}}$, with no information on fault types. To address this, we create pseudo-labels for the test dataset, which contains both healthy samples and various fault types, based on the clustering results.

To achieve this, we add a K-class classifier $C_{\theta_c}(\cdot)$ to the CAE, where K is the number of clusters, as depicted in Figure 7.8. This network takes as inputs the flattened features from the CAE latent space $\boldsymbol{z}$, and classifies them into K classes, as depicted in Equation (17). The weights of the encoder $E_{\theta_e}(\cdot)$ are frozen after training the CAE, with only the classifier $C_{\theta_c}(\cdot)$ being trained during this process. The parameters θ_c represent the classifier parameters.

$$\hat{\boldsymbol{y}} = C_{\theta_c}(E_{\theta_e}(\boldsymbol{x})) = C_{\theta_c}(\boldsymbol{z}) \tag{17}$$

The classifier $C_{\theta_c}(\cdot)$ is trained using samples from the test dataset $\mathcal{D}_{\text{test}}$ as inputs and the one-hot encoded cluster pseudo-labels $\boldsymbol{y} \in \{0,1\}^K$ assigned from the clustering results. The training process employs the softmax cross-entropy loss function, as illustrated in Figure 7.8 Step 3. Finally, IG is applied to this classifier to obtain feature attribution explanations for each test sample.

In this work, the average spectrogram of healthy samples is used as the baseline input in IG. However, due to the sparsity of the attribution maps, interpreting the raw maps remains challenging, even for domain experts. To enhance interpretability, max pooling operations are applied to refine the maps and generate a “diagnostics matrix". The diagnostics matrix has a lower temporal and frequency resolution, compared to the original attribution maps, making it more accessible for human interpretation due to its lower dimensionality. Each element in the matrix represents the max attribution value for a specific time-frequency region, facilitating a more intuitive fault diagnostics process.

7.6 Implementation Details

7.6.1 HV Gas Circuit Breaker - Fault Injection

Data Pre-processing

The signals from the four sensors are recorded simultaneously. Manual inspection revealed that most of the vibration signals are concentrated in the first $500\,\mathrm{ms}$, with vibrations damping out thereafter. Therefore, to reduce computational costs, only the first $500\,\mathrm{ms}$ were retained for analysis. For input into the CAE, log-Mel spectrograms, a type of time-frequency spectrogram, were extracted from the truncated signals, as Mel spectrograms have been proven effective in many applications such as detecting malfunctions in industrial machinery [163] and recognizing speech emotions [164]. Time-frequency spectrograms were used because they facilitate the extraction and analysis of information. They provide a two-dimensional representation of a signal, displaying both frequency and time information simultaneously. By converting a time-series signal into its time-frequency components, spectrograms make it easier to detect and analyze features that are not readily apparent in the time-domain alone.

Given the presence of multiple sensors, spectrograms from each sensor were concatenated channel-wise. This concatenation ensures that each pixel in the spectrogram contains comprehensive information at a specific time and frequency across all sensors, assuming synchronized data acquisition. As mentioned in Section 7.5.2, the input spectrogram has a size of $H \times W \times C$. In this case, H represents the number of frequency bins, W is the number of time bins, and C is the number of sensors. Specifically, the input dimensions were set to $128 \times 100 \times 4$ in this work. Example vibration signals in the vertical direction for Condition #1 to #5 and their corresponding Mel-spectrograms are shown in Figure 8.28. Note that the sample for Condition #3 shows low vibration amplitudes compared to samples with different conditions and is thus simple to recognize, whereas the other four conditions are challenging to distinguish visually.

Evaluation Metrics

Four metrics are used to evaluate the clustering performance with respect to the ground-truth labels. The first one is the adjusted Rand index (ARI) [165]. The ARI measures the similarity between two clustering results, offering a normalized score that adjusts for chance agreement. Specifically, it compares the clustering generated by the algorithm, denoted as $\mathcal{C}$, with a ground-truth clustering $\mathcal{K}$, where correct class assignments are known. The underlying Rand Index (RI) quantifies the agreement between these two clusterings by considering all pairs of elements and counting pairs that are either assigned to the same or different clusters in both $\mathcal{K}$ and $\mathcal{C}$. The ARI adjusts this measure to account for the chance grouping of elements, thus providing a more accurate assessment of the clustering validity. The RI is defined as follows:

$$\mathrm{RI} = \frac{a+b}{C_2^{n_{\text{samples}}}} \tag{18}$$

where a is the number of pairs of samples that are placed in the same cluster in both $\mathcal{K}$ and $\mathcal{C}$, and b is the number of pairs that are placed in different clusters in both clusterings. The denominator, $C_2^{n_{\text{samples}}}$ is the total number of possible pairs in the dataset and n_{samples} is the number of samples. The ARI is the

modified version of RI to correct for the chance grouping of elements. It is defined as follows:

$$\text{ARI} = \frac{\text{RI} - \mathbb{E}(\text{RI})}{\max(\text{RI}) - \mathbb{E}(\text{RI})} \tag{19}$$

where $\mathbb{E}(\text{RI})$ is the expected value of the RI under random classification. An ARI of 1 indicates perfect agreement between the two clustering results relative to chance, while an ARI of 0 suggests that the clustering is no better than random.

The other three metrics are the homogeneity score h, completeness score c, and v-measure v [166], which are commonly used in unsupervised clustering. The homogeneity score h (also known as purity) measures how well each cluster contains only data points from a single class. It is defined as:

$$h = 1 - \frac{H(\mathcal{C}|\mathcal{K})}{H(\mathcal{C})} \tag{20}$$

where $H(\mathcal{C})$ is the entropy of the data classes and $H(\mathcal{C}|\mathcal{K})$ is the conditional entropy of the classes given the cluster assignments. Similarly, the completeness score c measures how well all data points of a particular class are assigned to the same cluster. It is defined as:

$$c = 1 - \frac{H(\mathcal{K}|\mathcal{C})}{H(\mathcal{K})} \tag{21}$$

where $H(\mathcal{K})$ is the entropy of the cluster assignments and $H(\mathcal{K}|\mathcal{C})$ is the conditional entropy of the cluster assignments given the data. The v-measure v combines both homogeneity and completeness and is defined as:

$$v = \frac{2 \cdot h \cdot c}{h + c}. \tag{22}$$

All three metrics range between 0 and 1, with a score of 1 indicating perfect clustering results.

To quantitatively evaluate the SOM results, we also report internal metrics. Three metrics are used to validate that the SOM accurately represents the data distribution and has good topological organization [167]. These metrics include: quantization error, topographic error, and topographic product. Quantization error measures the average Euclidean distance error introduced when projecting data onto the SOM, while topographic error evaluates the neighborhood preservation of the projection (lower is better). The topographic product assesses the smoothness and preservation of neighborhood relations between the SOM map and the input space, where values closer to 0 are better.

For the performance of the XAI results, we utilize the concept of faithfulness [168], which measures how accurate are the features highlighted by the attribution explanations. To do so, faithfulness evaluation involves measuring the change in the classifier $C_{\theta_c}(\cdot)$ output when occluding the features selected by an explanation (typically replacing them with zeros). In our case, the features correspond to individual pixels in the spectrograms. First, in order to assess the quality of the explanations obtained with an attribution method (such as Integrated Gradients), we perform an attribution-based occlusion, where the features with the highest attribution values (the most important ones according to the XAI method) are occluded. Then, we perform a random occlusion, where sets of features are randomly selected and occluded. If the explanations are meaningful, attribution-based occlusion should lead to larger changes in the model output than random occlusion. As the spectrograms have a high dimension, features are not replaced one by one, but by groups for each channel. The modified spectrograms $\tilde{\boldsymbol{x}}$ are then fed into the trained encoder and classifier. For each occlusion, we compute the absolute difference in the classifier's outputs for the predicted class before and after the occlusion, as defined in Equation (23), for each sample. The outputs are taken from the last layer after applying the softmax activation function, providing insights into how the removed features impact the model's confidence in the prediction:

$$\Delta\text{prediction}(\boldsymbol{x}) = \left| C_{\theta_c}(E_{\theta_e}(\boldsymbol{x}))[\hat{y}] - C_{\theta_c}(E_{\theta_e}(\tilde{\boldsymbol{x}}))[\hat{y}] \right|, \tag{23}$$

where $\hat{y} = \arg\max C_{\theta_c}(E_{\theta_e}(\boldsymbol{x}))$ is the predicted class for the original input.

Model Architecture and Hyperparameter Settings

To calculate the Mel spectrogram, the number of Mel bands was set to 128, and the hop length was set to 501, resulting in a spectrogram for one operation with four sensors of size $128 \times 100 \times 4$. The CAE architecture is summarized as follows: the encoder $E_{\theta_e}(\cdot)$ consists of Conv2D $(16 \times 3 \times 3)$, Max Pooling (2×2), Conv2D $(8 \times 3 \times 3)$, Max Pooling (2×2), Conv2D $(1 \times 3 \times 3)$, Max Pooling (2×5). Here, Conv2D $(f \times f_x \times f_y)$ represents a 2D convolutional layer with f filters and a filter size of $f_x \times f_y$, and Max Pooling $(m_x \times m_y)$ represents the max pooling layer with a size of $m_x \times m_y$. Similarly, the decoder $D_{\theta_d}(\cdot)$ has the reversed architecture as the encoder $E_{\theta_e}(\cdot)$, but instead of 2D convolutional layers, it uses deconvolutional layers, and instead of max pooling layers, it uses 2D up-sampling layers. This architecture is selected from a grid search. With this architecture and the shape of input Mel spectrogram 128×100, the latent space has a dimension of 16×5. The activation functions in the CAE are all rectified linear units (ReLU), except for the final output layer, which uses a linear activation.

The classifier $C_{\theta_c}(\cdot)$ has a simple architecture comprising only one layer. The input layer is the flatten layer of the latent space with 80 neurons, which is the size of the flattened CAE latent space. The output is a fully connected layer with 5 neurons, representing one-hot encoded $K = 5$ clusters identified from K-means. The activation function is softmax, and no bias is applied in the classifier. To generate a diagnostics matrix, max pooling operations with a pooling size of (32, 20) are applied to the attribution maps, which have a same shape as the spectrogram. The diagnostics matrix, in this case, has a temporal resolution of five intervals (interval of $100\,\mathrm{ms}$) and a frequency resolution of four bands (low, mid-low, mid-high, high).

The CAE was trained for 300 epochs with a batch size of 8, using early stopping with patience of 10 epochs. The epoch indicates how many times the training data is fed through the model. The Adam optimizer [169] with $\beta_1 = 0.9$ and $\beta_2 = 0.999$, a learning rate of 0.001, and the mean squared error loss function were used. The CAE was trained only on the healthy data (Condition #1 - nSnD) defined in Table 6.4. A randomly selected 10% subset of the healthy data served as the validation dataset. The classifier $C_{\theta_c}(\cdot)$ was trained on the test dataset using the same training procedure as the CAE after fault segmentation step, but with categorical cross-entropy as the loss function.

For the unsupervised clustering analysis, the number of clusters K for K-means is set to 5 using elbow curve analysis, initialized with K-means++. For the OPTICS algorithm, the neighborhood size is set to 5 samples, and the distance parameter p is set to 2, corresponding to the Euclidean distance. Both K-means and OPTICS are implemented using scikit-learn. For the SOM, a 10×10 grid is used, with a Gaussian neighborhood function, a spread σ of 5, and a learning rate of 0.05. The SOM implementation is using the MiniSom [170], and performance metrics using SOMperf [167]. All clustering algorithms operated on the 80-dimensional latent space features extracted from the trained CAE.

7.6.2 HV Gas Circuit Breakers - Run-to-failure

ML-based module is applied on monitoring condition of the GCB2 using the vibration signals.

Data Pre-processing

The first $125\,\mathrm{ms}$ of the vibration signals are truncated, and Mel spectrograms are computed with a shape of $32 \times 352 \times 1$, as only one vibration sensor is used. These spectrograms captures time-frequency dependency and are used as inputs to the CAE.

Model Architecture and Hyperparameter Settings

The CAE architecture used for this case is as follows: the encoder $E_{\theta_e}(\cdot)$ consists of Conv2D $(4 \times 3 \times 3)$, Max Pooling (2×2), Conv2D $(1 \times 3 \times 3)$, Max Pooling (2×2). The decoder $D_{\theta_d}(\cdot)$ mirrors the encoder structure, replacing 2D convolutional layers with deconvolutional layers and max pooling with 2D up-

sampling. Rectified linear units (ReLU) are used for all activations except the final output layer, which is linear.

The CAE is trained for 100 epochs with a batch size 8, using early stopping with a patience of 10 epochs. The Adam optimizer is used with the same hyperparameter settings described in Section 7.6.1.

The first 50 samples from the run-to-failure experiments of GCB2 are considered healthy and used for training, the next 20 samples for validation, while the last 500 operations prior to failure are used for testing. The CAE is trained exclusively on healthy samples, and the residuals from the test samples should show increasing or decreasing trends that can be used as health indicators.

7.6.3 HV Gas Circuit Breakers - In Substation

One of the four monitored CBs, GCB6, is monitored with a different monitoring box with different sampling rate and data format, therefore, for convenience, only the other three GCBs are used for training the CAE. The number of samples used for train, validation and test are shown in Table 7.4. Two opening operations from GCB5 were discarded from the investigation because they were too close to preceding operations, resulting in shorten sampling lengths for the recorded signals.

Table 7.4: The number of samples used for train, validation, and test for the closing and opening operations of CBs in the substation. The dataset spans approximately one year of operation.

	GCB5	GCB7	GCB8	Total
	Closing			
Train	25	25	25	75
Val	3	3	3	9
Test	5	6	6	17
Total	33	34	34	101
	Opening			
Train	20	20	20	60
Val	2	4	3	9
Test	8	7	6	21
Total	30	31	29	90

Unlike the run-to-failure experiment in a laboratory, CBs in real-world applications typically switch infrequently. A data collected for approximately one year result in about 30 operations for each CB, as shown in Table 7.4. The training samples are assumed healthy. For closing operations, a CAE was trained on 75 samples and for opening operations another CAE was trained on 60 samples.

Data Pre-processing

Similar to the case in Section 7.6.1, only the first $500\,\mathrm{ms}$ of the vibration signals were used and converted into log-Mel spectrogram. Since only one vibration sensor is used, the spectrogram has only one channel. The input dimensions were designed to be $128 \times 120 \times 1$ to be used as inputs to a CAE.

Model Architecture and Hyperparameter Settings

The parameters used for constructing Mel spectrogram is the same as in Section 7.6.1. The CAE architecture is as follows: the encoder $E_{\theta_e}(\cdot)$ consists of Conv2D $(16 \times 3 \times 3)$, Max Pooling (2×2), Conv2D $(8 \times 3 \times 3)$, Max Pooling (2×2). The decoder $D_{\theta_d}(\cdot)$ has the reversed architecture as the encoder $E_{\theta_e}(\cdot)$, but instead of 2D convolutional layers, it uses deconvolutional layers, and instead of max pooling layers, it uses 2D up-sampling layers. The activation functions are all rectified linear units (ReLU), except for the final output layer linear. A CAE is trained on data collected during opening operations and another on closing operations. Both CAEs are trained with 30 epochs and a batch size of 16.

7.7 Summary and Limitations

The proposed monitoring framework consists of three modules, each capable of assessing independently the condition of a CB as either healthy or anomaly. This offers flexibility in application depending on the data availability. Typically, calibration on another CB is required to estimate the remaining useful life after an anomaly occurs. If the detected anomaly is not conditional anomaly such as those introduced in Section 6.8, the potential fault type can be inferred from domain knowledge of features from feature-based module or XAI from ML-based module.

A current limitation of the framework is the need to predefine key hyperparameters, such as the minimum number of healthy operations required N_1 to use feature-based and similarity-based modules, or to utilize ML-based module N_2. Setting these thresholds involves a trade-off, where too few operations may not be sufficient to capture the healthy distribution, while too many operations may already include early signs of degradation.

8 Application of the Proposed Framework

In this chapter, the results of applying the framework proposed in Chapter 7 to the datasets introduced in Chapter 6 are given. The results are organized according to the three modules of the framework: the feature-based module in Section 8.1, the similarity-based module in Section 8.2, and the ML-based module in Section 8.3. The summary of sections in this chapter is provided in Table 8.1.

Table 8.1: Summary of sections applying the three modules and the corresponding CBs presented in this chapter. Details about each CB is described in Table 6.1 and 6.2. F-based: feature-based, S-based: similarity-based.

	GCB1	GCB2, 3	GCB4	GCB5, 6, 7, 8	VCB1
F-based	8.1.2	8.1.1	-	8.1.4	8.1.3
S-based	8.2.2	8.2.1	-	-	-
ML-based	8.3.3	8.3.1	8.3.2	8.3.4	-

8.1 Feature-based Module

This section summarizes results when applying feature-based module on different CBs.

8.1.1 HV Gas Circuit Breakers - Run-to-Failure

Parts of this section are based on the publication [14].

In this section, we summarize the results of applying the feature-based module including key moments identification and the feature extraction from the last approximately 500 operations preceding a failure from two HV GCBs (GCB2 and GCB3) based on the run-to-failure experiments. The results obtained from GCB2 are plotted in gray, while those from GCB3 are shown in blue, except for Figure 8.1, where all results are from GCB2, with the key moments extracted from vibration signals depicted in gray and from the travel curve is green.

Key Moments Identification

The two key moments t_{c1} and t_{c2} from closing operations along with the three t_{o1}, t_{o2} and t_{o3} from opening operations identified from the STE of the vibration signals of GCB2 using Algorithm 1 (in gray) and from the travel curve (in green) are shown in Figure 8.1. For closing operations, the first key moment t_{c1}, extracted from the vibration signals, remains unchanged throughout the last 500 operations before failure, indicating that the initiation of contact motion exhibits no degradation during that period. In contrast, the second key moment t_{c2} shows a slight increasing trend, characterized by a positive slope with a linear fit. This suggests that the duration for the contact to come to a stop ($t_{c2} - t_{c1}$) increases with the number of operations, showing a potential indication of aging in components related to motion initialization.

Similarly, in open operations, the first key moment t_{o1}, extracted from the travel curve and vibration signals, remain unchanged. The second key moment t_{o2} shows a decreasing trend, indicating that the damper is not always reached at the same time. Similarly, the third key moment t_{o3}, extracted from the vibration signals, also exhibits a decreasing trend, implying that the contacts reach their end position faster and the entire duration of the contact travel ($t_{o3} - t_{o1}$) is shorter.

The key moments extracted from the vibration signals and the travel curve are not identical. This discrepancy arises from the challenge of precisely determining the instances when the contacts start and stop their movement, particularly around the closed position, such as t_{c1} and t_{o3}, where the transition points are corrupted by measurement noise. To address this, a compromise is made by considering 1% and

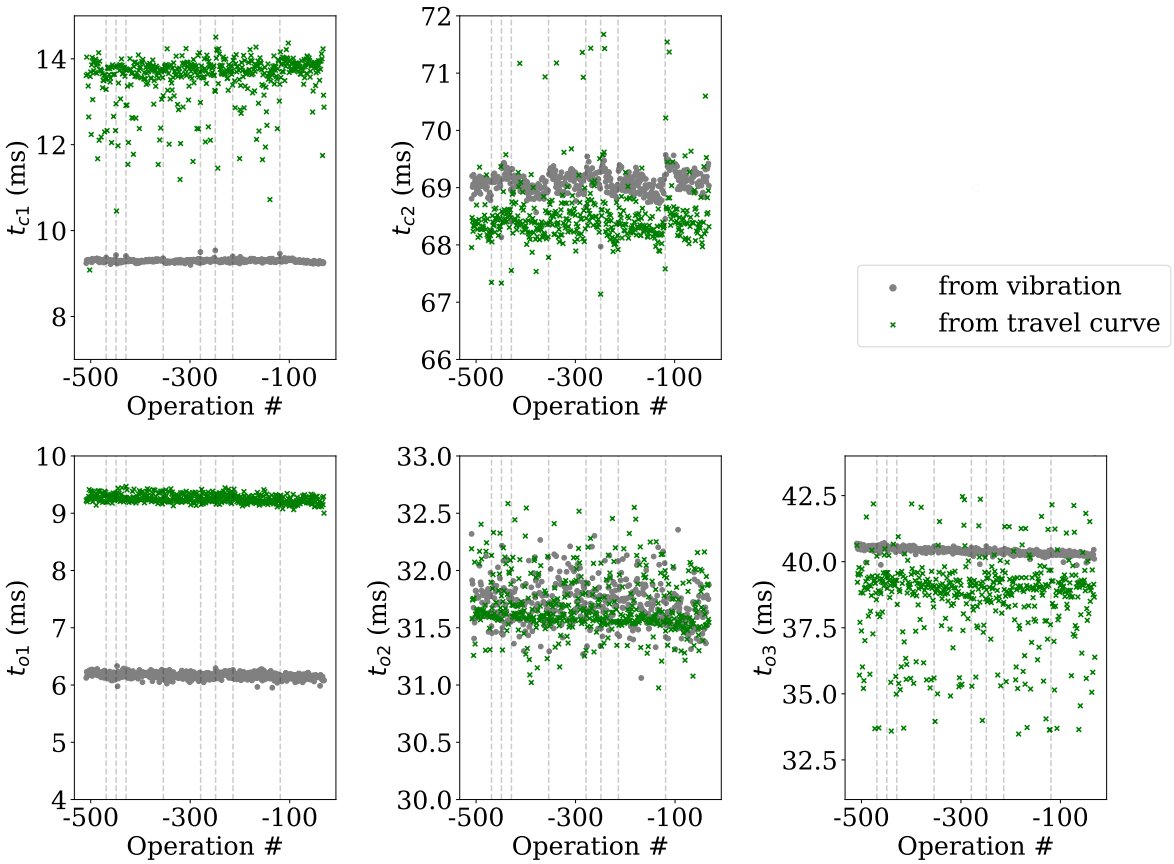


Figure 8.1: Key moments t_{c1}, t_{c2} during the closing operations and t_{o1}, t_{o2} and t_{o3} during the opening operations from GCB2 extracted from the vibration signals (gray) and the travel curve (green). The vertical dashed lines represent operations with idle time longer than one hour.

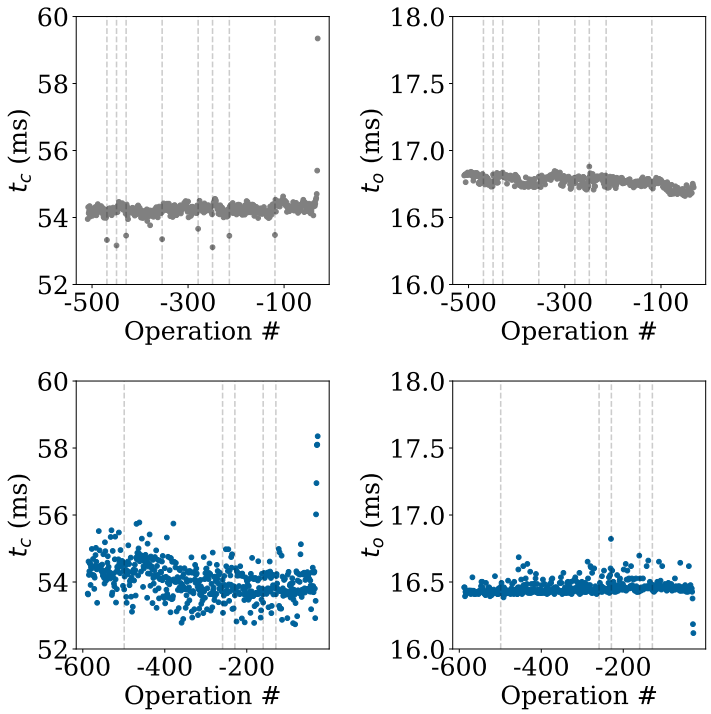


Figure 8.2: The closing time t_c and the opening time t_o extracted from the contact separation measurements for both GCB2 (gray) and GCB3 (blue). The last open operation for GCB2 has an opening time of $37\,\mathrm{ms}$, and for GCB3, it is $20\,\mathrm{ms}$. These two values are not plotted as they fall outside of the plot range. The vertical dashed lines represent operations with idle time longer than one hour.

99% of the stroke in the travel curve. The key moments t_{c1} and t_{o3} have lower variances of $0.001\,\mathrm{s}^2$ and $0.205\,\mathrm{s}^2$, respectively, when extracted from the vibration signals, compared to $7.462\,\mathrm{s}^2$ and $2.612\,\mathrm{s}^2$ from the travel curve. This indicates that identifying these key moments using the vibration signals is more robust and less sensitive to measurement noise than relying on the travel curve. These vibration-based key moments are used in the following section for segmenting different stages and extracting features, as they provide more robust results.

The other two timing parameters, opening and closing time, t_o and t_c, obtained from the contact separation measurements for both CBs are shown in Figure 8.2. Both remain nearly unchanged throughout most of the run-to-failure process until shortly before failure and change significantly in the last few operations, indicating anomalies and potentially early signs of failure. The closing time for GCB2 increases from $54\,\mathrm{ms}$ to $55\,\mathrm{ms}$ and then to even longer than $59\,\mathrm{ms}$. Similarly, for GCB3 closing time increases in the final few operations to more than $58\,\mathrm{ms}$. The opening time for GCB2 that is approximately $16.75\,\mathrm{ms}$ for most of the operations but suddenly increases to $37\,\mathrm{ms}$, while for GCB3 the opening time t_o shows a sudden decrease before failure and then increases to approximately $20\,\mathrm{ms}$, which is out of the range of Figure 8.2.

Note that some operations experience a faster t_c compared to others. These faster occurrences coincide with instances of longer idle time between operations, ranging from a few hours to a few days, as described in Section 6.8.3. Vertical dashed lines in Figure 8.2, also in Figure 8.1, mark operations with idle times longer than one hour. We denote this effect as the idle time effect, meaning that the first operation after a long idle time exhibits different patterns compared to others with shorter idle time. Additionally, a decreasing trend in t_c is visible between the dashed lines. However, the idle time effect does not play a role in the opening time t_o.

Features from Vibration Signals

The features 'peak' and 'RMS', extracted from the entire vibration recording length during opening and closing operations for GCB2, are shown in Figure 8.3. The peak vibration value for both operations remains within the range of approximately $90\,\mathrm{g}$ to $180\,\mathrm{g}$. The RMS values for both operations display an increasing trend. Notably, prior to failure, the RMS value reaches a level that was never observed when the CB was in a healthy state. While the aforementioned idle time effect is not noticeable for the peak values in either operation, it is apparent in the RMS values during close operations. In this case, operations with longer idle times have lower RMS values.

To gain a deeper understanding of the CB condition, features are extracted not only for the entire vibration duration but also for each stage during the opening operations. As depicted in Figure 8.4, the peak and RMS values do not display a specific trend during stages O-I and O-II, but they exhibit an increasing trend during stage O-III. This could suggest that as the CB degrades, the energy involved in the operation is higher, leading to stronger vibrations. In summary, by monitoring not only the entire vibration movement of the CB but also its individual stages, a more detailed assessment of the CB's condition can be achieved. This approach enables the identification of deviations from healthy operation and links them to specific components, facilitating clearer fault explanation, diagnostics, and even prognostic. In the run-to-failure experiments, the failure appears to be related to processes and components involved in the final stage of the opening operations.

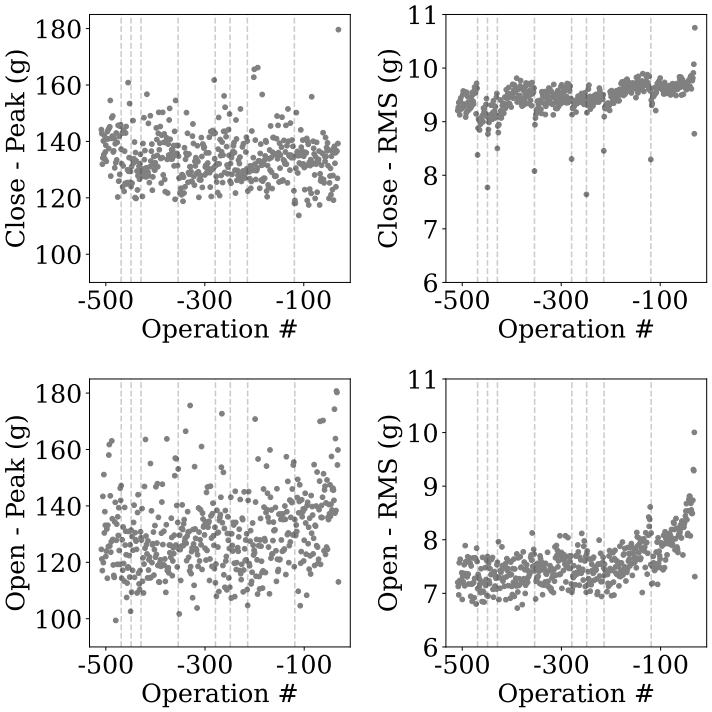


Figure 8.3: Vibration peak and RMS for both closing and opening operations during the entire recording length for GCB2. The vertical dashed lines represent operations with idle time longer than one hour. The RMS extracted for the opening operations show a continuous increasing trend.

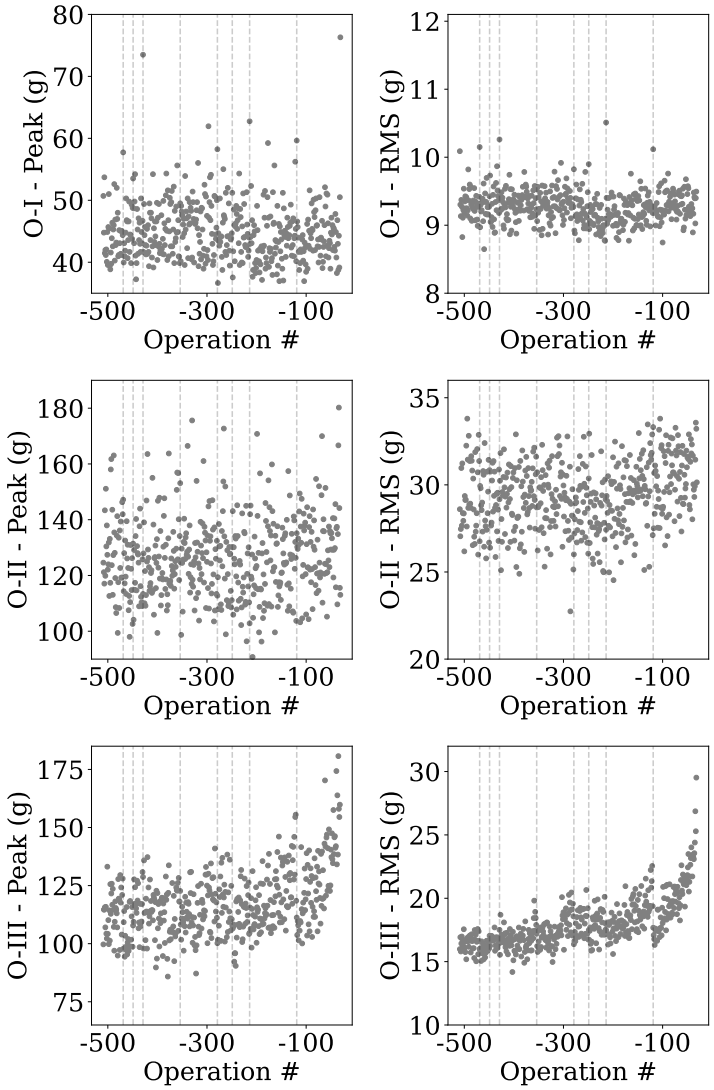


Figure 8.4: The features peak and RMS for opening operations for GCB2 per stage as defined in Figure 6.6 with the key moments extracted from the vibration signals. The vertical dashed lines represent operations with idle time longer than one hour.

Features from Coil Current Signals

Apart from the vibration features, the open coil current for both CBs during the first $30\,\mathrm{ms}$ from several operations before failure is shown in Figure 8.5. The current shape remains nearly identical for all operations up until the last few operations prior to failure. During these operations, the current waveforms are similar up to the first valley, with noticeable discrepancies emerging at the second peak. The second peak current decreases and occurs earlier as failure approaches. This implies that components involved in the initial phase (before approximately $10\,\mathrm{ms}$), such as the open coil itself, are likely still functioning properly. In contrast, the observed deviations after $10\,\mathrm{ms}$ can be faults in components related to the latter phase around the second peak.

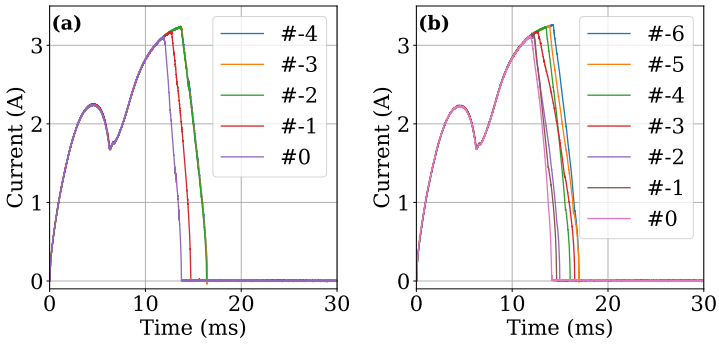


Figure 8.5: The first $30\,\mathrm{ms}$ of the open coil current during the last few operations before failure of (a) GCB2 and (b) GCB3. Both current signals exhibit the same patterns: the peak current decreases, and the time to reach the peak shortens.

The features, time to peak current and peak current, t_3 and i_3, for both GCBs are plotted in Figure 8.6. The features i_1 and i_2, which are not plotted, remain unchanged throughout the experiments, indicating that the condition of the coil do not encounter significant degradation for either CB. The feature t_3 remains unchanged at approximately $13.6\,\mathrm{ms}$ for GCB2 and $14.2\,\mathrm{ms}$ for GCB3 during the experiments, but it suddenly decreases to $12.5\,\mathrm{ms}$ for GCB2 and below $11\,\mathrm{ms}$ for GCB3 shortly before failure, following a similar trend to both opening and closing times. The feature i_3 clearly indicates the idle time effect for both CBs, with a decreasing trend after a long idle time. Similarly, the features i_1 and i_2, which are not shown in Figure 8.6, exhibit similar trends to i_3.

Notice that for GCB3, between approximately operation number -500 to -250, the current i_3 remains unchanged, unlike the other cases. This is likely due to the shorter idle time between these two operation blocks. The feature values tend to stabilize after a larger number of consecutive operations. In addition, the degradation trajectories of both CBs are similar, indicating that they may be affected by the same fault type. The remaining six features are not plotted due to space limitation, as they do not show distinct degradation trends.

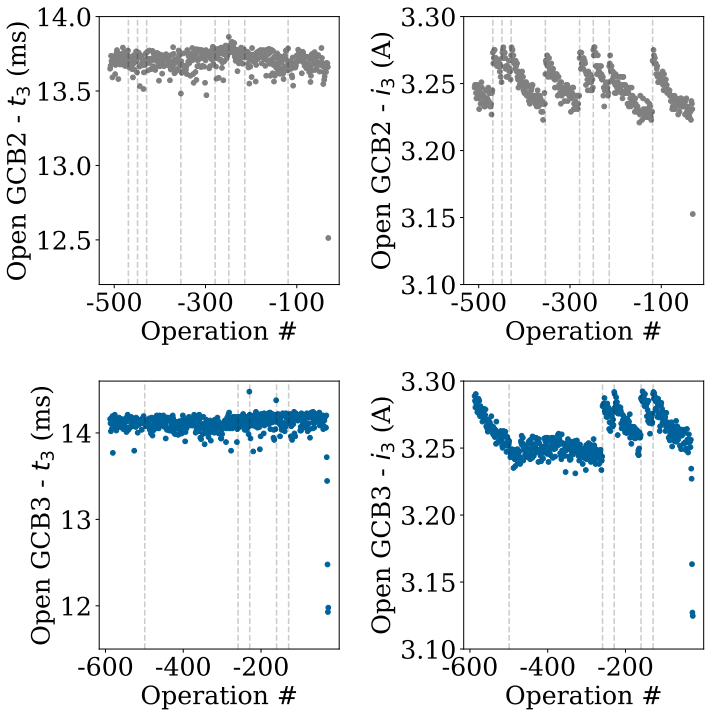


Figure 8.6: Open coil current features t_3 and i_3 for GCB2 (gray) and GCB3 (blue). Only two features instead of eight are shown here due to limit space. The feature t_3 remains unchanged during the run-to-failure process and only changes shortly before failure occurs for both GCBs. The idle time effect is dominant on the feature i_3 for both GCBs, with a decreasing trend after a long idle time. The vertical dashed lines represent operations with idle time longer than one hour.

Motor Running Time

The motor running time for charging the operating mechanisms for GCB3 after opening and closing operations over the last 1 000 operations is shown in Figure 8.7. In both cases, no clear increasing or decreasing trend is observed. Notably, the motor running time after opening operations shows low variability, with a standard deviation of only $0.23\,\mathrm{s}$, while the running time after closing operations shows approximately four times greater variation. Although some deviations are observed during the last 10 closing operations, they are insufficient to draw a definitive conclusion. Overall, motor running time does not appear to be a reliable indicator for this particular failure mode, which is not associated with the motor.

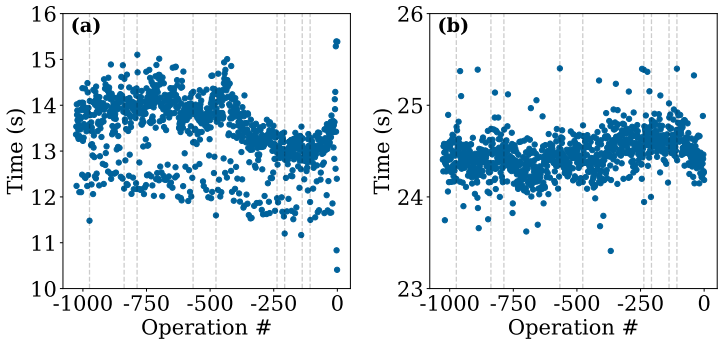


Figure 8.7: Motor running time for charging the operating mechanisms of GCB3 following (a) closing and (b) opening operations. The values appear scattered and fluctuating, making it difficult to draw clear inferences about CB condition. The vertical dashed lines represent operations with idle time longer than one hour.

Summary - Application of Feature-based Module on GCBs

Parts of this section are based on the publication [14].

The results obtained from run-to-failure experiments on two GCBs as discussed in Section 8.1.1 demonstrate that it is feasible to extract relevant condition information and infer both degradation dynamics and continuous changes in fault severity using signals measured non-intrusively. In addition, different stages of the opening and closing operations can be effectively segmented using either vibration or travel curve signals.

Features extracted from sensor recordings show varying degradation trajectories, which are summarized in Table 8.2 for closing and Table 8.3 for opening operations. These tables consist of five columns: feature name, CB number, signal type and whether this signal is measured intrusively, degradation trajectory type, and whether the feature is affected by long idle times between operations.

Table 8.2: Summary of the characteristics of the extracted features from the two run-to-failure experiments for closing operations.

Features	#GCB	Signals (Intrusive?)	Trajectory	Idle time
Closing operations				
t_{c1}	2	vib. (✗)/TC (✓)	III	✓
t_{c2}	2	vib. (✗)/TC (✓)	II	✓
t_c	2	CS (✓)	I	✓
t_c	3	CS (✓)	I	✗
peak - entire	2	vib. (✗)	III	✗
RMS - entire	2	vib. (✗)	II	✓
✓: yes; ✗: no; vib.: vibration; TC: travel curve; CC: coil current; CS: contact separation measurement				
Degradation types: I - sudden change before failure; II - continuous increasing/decreasing; III - no change				

The features are categorized into three types based on their degradation trajectories. The trajectories of Type-I features remain constant until a sudden change occurs shortly before failure, such as the open coil current feature t_3 and i_3, and opening and closing time t_c and t_o. These features are not suitable for predicting long-term degradation but can be used for fault detection. The trajectories of Type-II features show a continuous increasing or decreasing trend, making them ideal for condition monitoring. Their future trend is more predictable, allowing them to be used for both fault detection and prediction. Examples of this type include the vibration RMS of opening operations extracted from the entire recording length and the vibration peak and RMS from stage O-III, which reflect the CB's aging condition over time. The trajectories of Type-III features stay constant throughout the entire run-to-failure experiment, such as the vibration peak and RMS in stages O-I and O-II. These features do not show significant changes and are not suitable for fault detection or prediction, indicating that the failure is unrelated to the specific stages or components associated with these features.

In addition, some features are impacted by long idle time, where the first operation after extended idle time shows distinct patterns. This effect is particularly evident in the vibration RMS for closing operations and the i_3 feature in open coil current. As illustrated in Figure 8.4, the vibration RMS and peak values from stage O-III show an initial increase from operation numbers -190 to -110 and from -110 to 0, then a decrease after a long idle time of more than 24 hours, before increasing again until failure. This suggests that idle time plays a role in the CB operation, possibly because of friction in the operating mechanism or drive. The impact of idle time requires further investigation since CBs in real-world applications often operate with longer idle times of up to several weeks or months. If a machine learning model is developed based on an accelerated run-to-failure dataset without considering these effects, operations after long idle time could be falsely identified as anomalies and lead to false alarms.

For effective continuous CB condition monitoring and prognostics, the trajectories of features must fulfill the following criteria to reliably track CB's condition over time. First, the feature should be extracted

from non-intrusively measured signals to ensure practicality in real-world applications. Second, it should be Type-II features, showing a gradual and smooth increasing or decreasing trend, making it suitable for tracking degradation over time. Lastly, it should be unaffected by idle times between operations to avoid false alarms. As a result, the most suitable features for continuous CB monitoring are identified as the vibration peak and RMS during the opening operations in stage O-III, and the RMS for the entire recording length of opening operations, given the run-to-failure experiment data on two CBs. These features demonstrate consistent degradation trends and are robust to idle time effects. They are marked in bold in Table 8.3, including RMS - entire, peak - O-III, and RMS - O-III.

Table 8.3: Summary of the characteristics of the extracted features from the two run-to-failure experiments for opening operations.

Features	#GCB	Signals (Intrusive?)	Trajectory	Idle time
Opening operations				
t_{o1}	2	vib. (✗)/TC (✓)	III	✗
t_{o2}	2	vib. (✗)/TC (✓)	II	✗
t_{o3}	2	vib. (✗)/TC (✓)	III	✗
t_o	2	CS (✓)	I	✗
t_o	3	CS (✓)	I	✗
peak - entire	2	vib. (✗)	III	✗
RMS - entire	2	vib. (✗)	II	✗
peak - O-I	2	vib. (✗)	III	✗
peak - O-II	2	vib. (✗)	III	✗
peak - O-III	2	vib. (✗)	II	✗
RMS - O-I	2	vib. (✗)	III	✗
RMS - O-II	2	vib. (✗)	III	✗
RMS - O-III	2	vib. (✗)	II	✗
t_1	2	CC (✓, ✗*)	III	✗
i_1	2	CC (✓, ✗*)	III	✓
t_2	2	CC (✓, ✗*)	II	✗
i_2	2	CC (✓, ✗*)	III	✓
t_3	2	CC (✓, ✗*)	I	✗
i_3	2	CC (✓, ✗*)	I	✓
t_4	2	CC (✓, ✗*)	I	✗
i_4	2	CC (✓, ✗*)	III	✗
t_1	3	CC (✓, ✗*)	III	✗
i_1	3	CC (✓, ✗*)	III	✓
t_2	3	CC (✓, ✗*)	II	✗
i_2	3	CC (✓, ✗*)	III	✓
t_3	3	CC (✓, ✗*)	I	✗
i_3	3	CC (✓, ✗*)	I	✓
t_4	3	CC (✓, ✗*)	I	✗
i_4	3	CC (✓, ✗*)	III	✗
✓: yes; ✗: no; vib.: vibration; TC: travel curve; CC: coil current; CS: contact separation measurement				
Degradation types: I - sudden change before failure; II - continuous increasing/decreasing; III - no change				
*Coil current are measured intrusively with shunt resistors in the experiment, but can also be measured non-intrusively with a current clamp.				

8.1.2 MV Gas Circuit Breaker - Run-to-Failure

This section presents the results of the feature-based module applied to the MV GCB from the run-to-failure experiment comprising approximately 6 000 operations, as described in Section 6.3. The analysis covers timing parameters, key moments, and vibration and coil current features.

Timing Parameters and Key Moments Identification

The opening and closing times obtained from contact separation measurements are shown in Figure 8.8 (a) and (b). Both timing parameters exhibit a continuous increase of more than $10\,\mathrm{ms}$, along with some fluctuations throughout the experiment. These fluctuations are likely caused by variations in friction and grease redistribution, since no maintenance or lubrication was performed during the entire run-to-failure experiment. These two timing parameters are ideal indicators for reflecting CB condition as they exhibit a continuous increasing trend with the increase of operation numbers.

The CB experienced twice "does not open on command" failures, where it did not respond to an electrical opening command signal. The first occurred at operation #5812 and the second at #6361, as shown by the red dashed lines in Figure 8.8 (c) and (d), which zoom in to highlight the effects of failure and idle time on timing parameters. Following the first failure at operation #5812, the CB was opened manually by pressing the opening button on the front panel. This may suggest that the friction in the operating mechanism had increased to the point where electrical actuation was no longer sufficient. Manual intervention may have redistributed the grease or release the stuck mechanism, allowing further operations. However, such not operate on command failure poses significant risks in real-world applications, if a CB does not open on command during a short-circuit condition, it could lead to severe consequences.

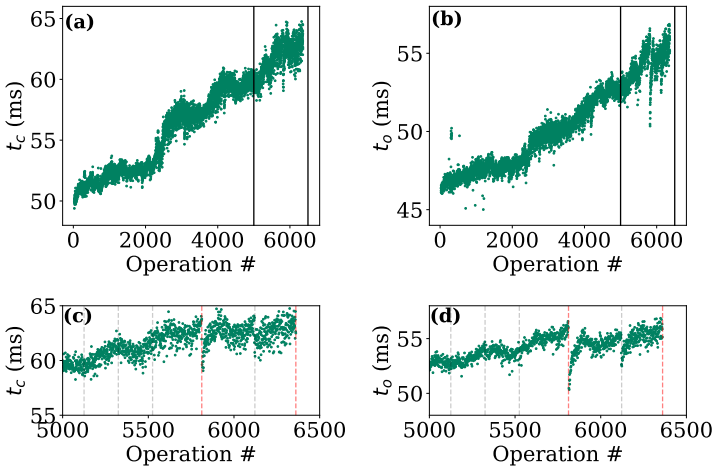


Figure 8.8: (a) The closing and (b) the opening time extracted from the contact separation measurements for MV GCB. (c) Zoom in of the closing and (d) opening time for the last 1500 operations, as marked between two vertical lines in Figure (a) and (b). The vertical dashed gray lines represent operations with idle time longer than one hour while dashed red lines indicate the failure "does not open on command".

An example of the first $150\,\mathrm{ms}$ of vibration signals from accelerometer 353B14 during an opening operation is shown in Figure 7.2(b), highlighting four key moments t_{o1} to t_{o4}. The evolution of these key moments across the entire run-to-failure experiment is shown in Figure 8.9.

A sharp decrease in t_{o1} and t_{o2} between operation #4600 and #4800 indicates a potential fault in components related to the initial phase of motion. This change occurs gradually over about 200 operations rather than abruptly, in contrast to the sudden feature changes observed after long idle periods. Meanwhile, t_{o4} shows a steady increase, following a trend similar to the opening time t_o in Figure 8.8.

During these 200 operations between operation #4600 and #4800, vibration patterns become increasingly distinct to those from the beginning, causing the key moment extraction algorithm (Algorithm 1) to fail in some cases and leading to some anomalies in Figure 8.9, particularly for t_{o3} and t_{o4}.

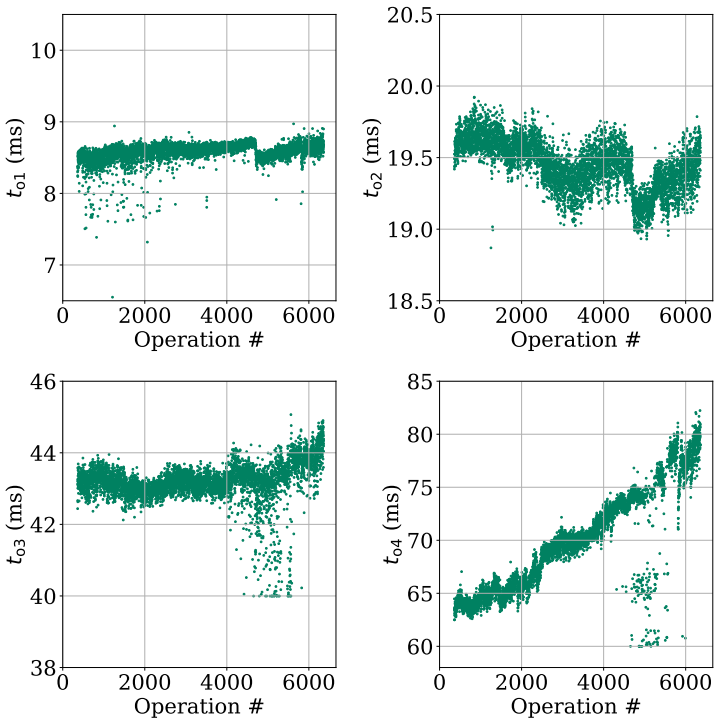


Figure 8.9: The four key moments t_{o1} to t_{o4} extracted from vibration signals collected by accelerometer 353B14 during opening operations in the GCB1 run-to-failure experiment. A change in key moment values between operations #4600 and #4800 causes the detection algorithm unable to determine some t_{o3} and t_{o4} values, resulting in abnormal key moment values in this range.

Features from Vibration Signals

To further investigate these changes, vibration signals for both closing and opening operations recorded every 1 000 operation during the run-to-failure experiment are plotted in Figure 8.10. For opening operations, the typical four key vibration events observed in the first 5 000 operations are disrupted around operation #5000, where additional events appear between $40\,\mathrm{ms}$ and $60\,\mathrm{ms}$. Interestingly, by operation #6000, the vibration pattern reverts to the four-event structure, but with lower amplitude.

For closing operations, vibration signals in the first 5 000 operations show two distinct high-amplitude segments with various timing and amplitude. However, in operation #6000, the first segment splits into several smaller events, and its onset time shifts, as shown in Figure 8.10. Such changes in vibration patterns indicate potential, whether additional, missing or shifted events, suggest potential anomalies in the operating mechanisms. When combined with domain knowledge, as discussed in Section 6.4 and 7.3.1 through high-speed camera investigation, these changes in vibration patterns can serve as effective indicators of CB condition.

Beyond visual inspection of the vibration signals in Figure 8.10 and analysis of timing parameters and key moments in Figure 8.8 and 8.9, statistical features were extracted to quantify changes in vibration signals. For clarity, only RMS values are presented here, as they show an interesting trend, while most other features remain unchanged or exhibit no clear pattern.

The RMS values from vibration signals acquired by accelerometer 353B14, positioned near the operating

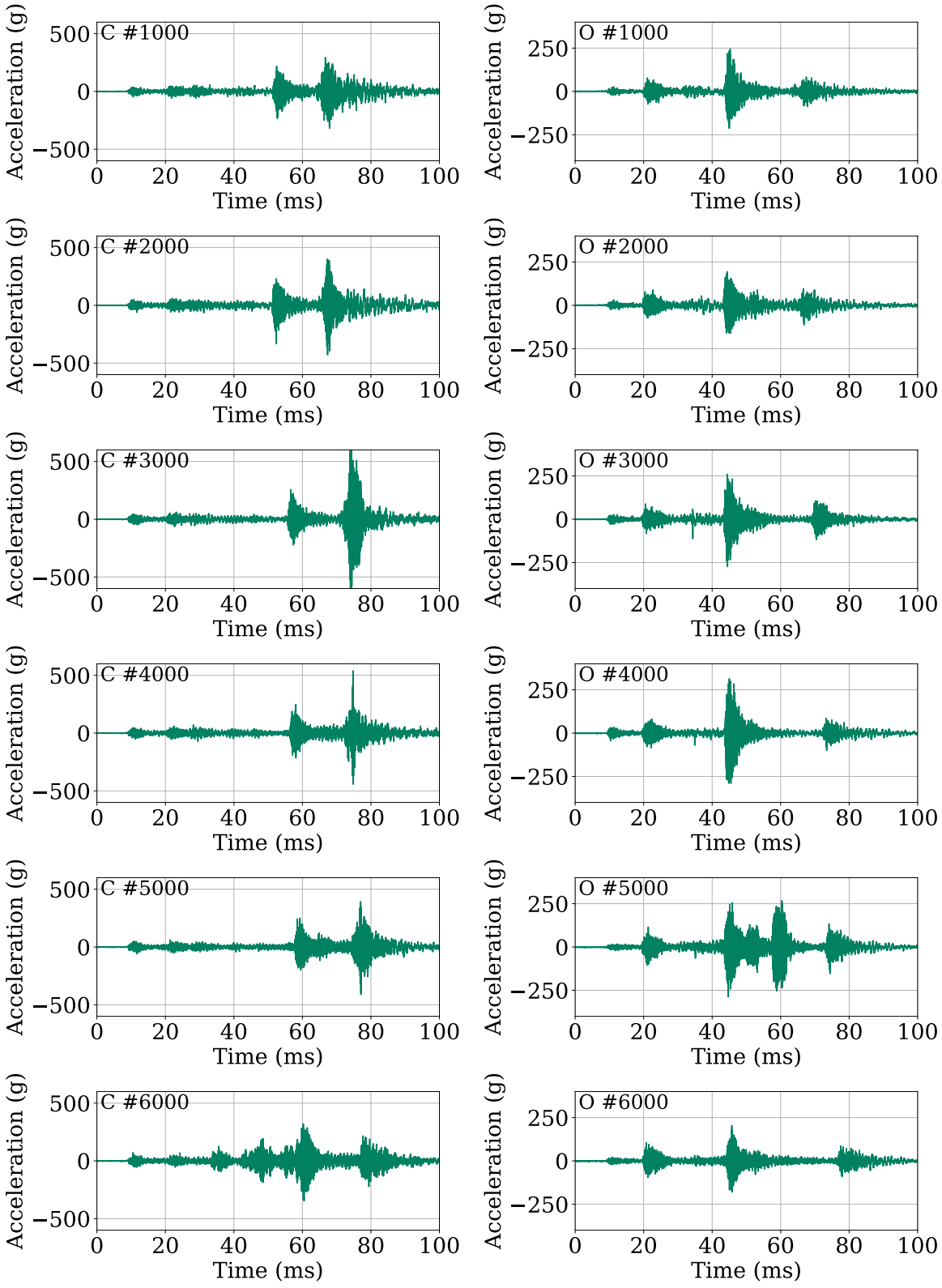


Figure 8.10: Vibration signals from accelerometer 353B14 recorded every 1 000 operations during closing and opening operations. Changes in vibration patterns such as an additional, missing, or delayed events, or variations in amplitude, may indicate potential anomalies in the operating mechanisms.

mechanisms, for both closing and opening operations are shown in Figure 8.11. For closing operations, RMS values fluctuate, with noticeable increases around operation #2000 and decreases around #4000. The operations start to be unstable and variability increases after #4000. Following the first failure (does not open on command) at operation #5812, RMS values become highly unstable and exhibit large variations.

In contrast to the steadily increasing RMS trend observed from GCB2 in Figure 8.3, the RMS values for GCB1 in Figure 8.11 show an unstable pattern. This indicates that feature trends depend on both CB type and fault type, with certain features proving useful for specific CB-fault combinations but not for others. For example, RMS is an effective feature for GCB2 condition but not for GCB1. This further suggests that GCB1 may have undergone multiple stages of degradation, where different components were progressively affected. These changes had varying impacts on the vibration signals, as shown in Figure 8.10, resulting in fluctuations in the extracted vibration features.

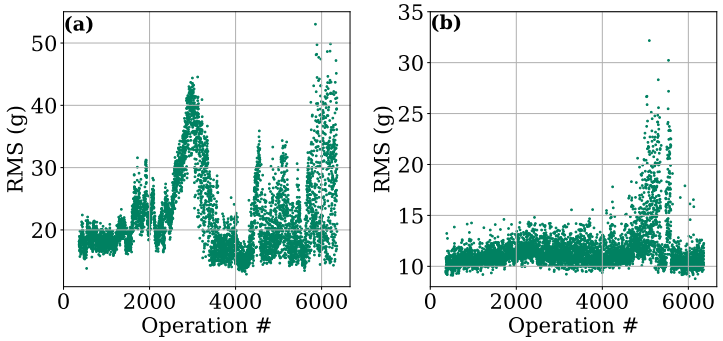


Figure 8.11: The RMS values from vibration signals recorded from accelerometer 353B14 for (a) closing and (b) opening operations of GCB1 during the run-to-failure process. These features may not be suitable for condition monitoring as the fluctuations are high.

Features from Coil Current Signals

Two features, i_1 and t_2, extracted from the open coil current signals are shown in Figure 8.12. Both exhibit a noticeable drop around operation #4700, despite unchanged operation conditions. This drop has also been observed in the key moments t_{o1} and t_{o2} in Figure 8.9, suggesting the development of a component fault affecting both the mechanisms linked to the key moments t_{o1} and t_{o2} and the coil current features i_1 and t_2.

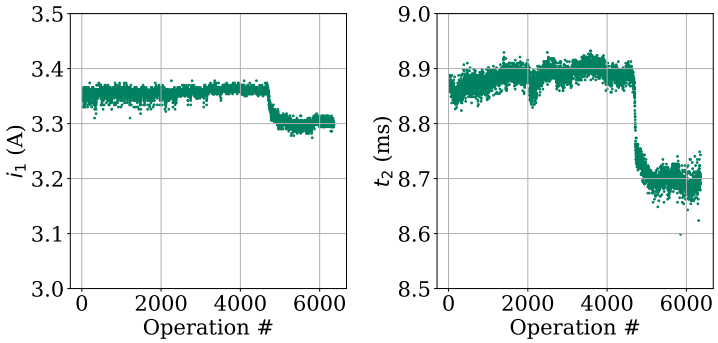


Figure 8.12: The features i_1 and t_2 extracted from open coil current signals. A decrease between operation #4600 and #4800 have similar pattern to the key moments t_{o1} and t_{o2}, suggesting potential change in the operation mechanisms.

The decrease in i_1 indicates reduced friction within the latch mechanism, suggesting that subsequent operations are performed with lower mechanical friction. The feature t_2 represents the initiation of the main operating mechanism and is typically followed shortly by an increase in vibration amplitude.

This behavior differs from the cases of GCB2 and GCB3 in Figure 8.6, where only abrupt changes due to idle time effect is observed. In contrast, i_1 and t_2 are the key features for reflecting CB condition. This highlights that different CB types and fault modes result in distinct degradation patterns. Therefore, monitoring framework or algorithm should incorporate a board set of features instead of relying on only a few.

8.1.3 MV Vacuum Circuit Breakers - Run-to-Failure

Parts of this section are based on the publication [28].

Timing Parameters

The closing and opening time, t_{c} and t_{o}, measured from the contact separation measurement of pole A of the MV VCB is shown in Figure 8.13. The closing time t_{c} increases when the operation number increases and starts from around $60\,\mathrm{ms}$ as described in the manual to more than $70\,\mathrm{ms}$ by the end of life. In contrast, the opening time has lower variance and remains below $40\,\mathrm{ms}$ until approximately operation # 28000, where the scatter starts to become larger. The other two poles Pole B and C show a similar trend. Therefore, only the closing time of pole A is shown here for simplicity.

In addition to the overall increasing trend observed during the run-to-failure process, several peaks appear, such as the two between operation #6000 and #9000. While the exact cause is uncertain, these variations in opening and closing time are likely linked to lubricant degradation within the CB due to continuous operation. Temporary redistribution of the lubricant may change friction conditions in the operating mechanisms, leading to short-term changes in operating timing. In this case, both opening and closing times can serve as useful indicators of CB condition.

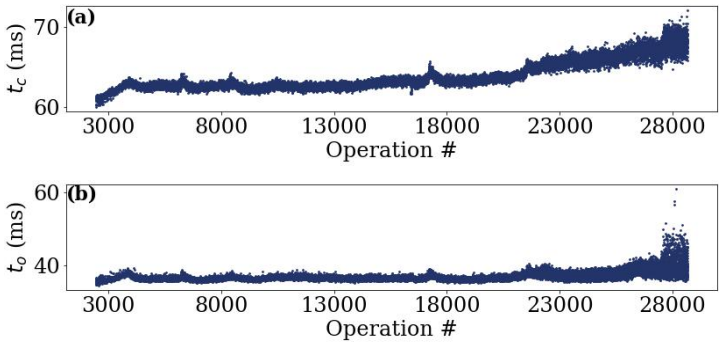


Figure 8.13: The (a) closing time t_c and (b) opening time and t_o of the VCB1 determined from the contact separation measurement over the entire run-to-failure experiment.

Specifically, the opening operations tend to be more consistent than the closing operations, meaning that the recorded signals during opening operations are more similar. This suggests that deviations in opening operations can be stronger indicators of degradation compared to deviations in closing operations. However, this observation is based on a single CB and may vary depending on the CB type and fault type.

8.1.4 HV Gas Circuit Breakers - In Substation

The CBs discussed in this chapter in the previous sections were operated in a laboratory environment. In this section, the focus is the four CBs operating in a substation as discussed in Section 6.7. Three key moments extracted from 28 opening operations of GCB7 are shown in Figure 8.14. All three key moments remain relatively stable, although the variation of t_{o3} is higher compared to the other two. This is likely because t_{o1} and t_{o2} occur during the contact movement, while t_{o3} takes place after the contacts have fully separated, meaning that it is not that critical for current interruption capability.

Unlike run-to-failure experiments, recording 28 opening operations for a single CB in the substation takes approximately one year, highlighting the limitations in data volume and the challenges of applying data-driven methods in real-world applications. However, the proposed framework is applicable even with a limited amount of data available.

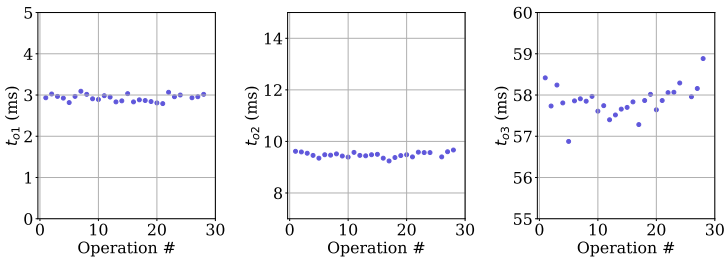


Figure 8.14: Key moments extracted from vibration signals during 28 opening operations of GCB7 in a substation over the course of approximately one year. The key moments remain unchanged, suggesting no significant variation in CB condition during this period.

8.2 Similarity-based Module

This section summarizes results when applying the similarity-based module on the different CBs.

8.2.1 HV Gas Circuit Breakers - Run-to-Failure

In this case, the first 50 operations of GCB2 were used as healthy baseline ($N_1 = 50$) and the similarity metrics were calculated between the baseline healthy signals and the last approximately 500 opening and closing operations.

Vibration and Acoustic Signals

To account for the highly non-stationary nature of the vibration signals, their STE representations were used instead of the raw signals. The results of the two metrics for one-dimensional time-series similarity, Euclidean distance and cosine similarity, on the STE of the vibration signals are shown in Figure 8.15. Only the first $125\,\mathrm{ms}$ of signals are considered, as most of signals damp out beyond this point.

For opening operations, the increase in Euclidean distance and the decrease in cosine similarity indicate that vibration patterns gradually diverge from those of the first 50 operations as the number of operations increases and when failure approaches. Similar to the vibration RMS from the feature-based module, both metrics exhibit a linear-exponential trend, with the operations close to failure having a large deviation compared to the healthy baseline.

For closing operations, both similarity metrics remain scattered yet stable throughout the run-to-failure process. This indicates that either these metrics are less effective for monitoring CB condition under this specific fault type, or that the components associated with closing operations have lower degree of degradation compared to those with opening operations. This observation aligns with the feature-based module results shown in Figure 8.3, where the vibration RMS feature shows a clear two-stage degradation trend in opening operations but not in closing operations.

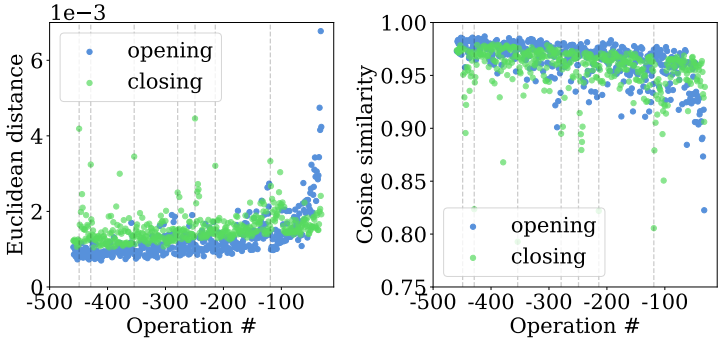


Figure 8.15: Average Euclidean distance and cosine similarity of the STE of the vibration signals during opening and closing operations. The vertical dashed lines represent operations with idle time longer than one hour.

Besides vibration signals, the results of the two similarity metrics for acoustic signals collected by a microphone are shown in Figure 8.16. The trends for both metrics in vibration and acoustics signals are similar, where for opening operations the similarity shows a gradual decreasing trend, while for closing operations, the values are more scattered.

Unlike vibration signals, acoustic signals typically have less distinct patterns, making the extraction of useful statistical features more challenging. However, when analyzed with the similarity-based module, acoustic signals can still reveal degradation patterns, particularly for opening operations in this case.

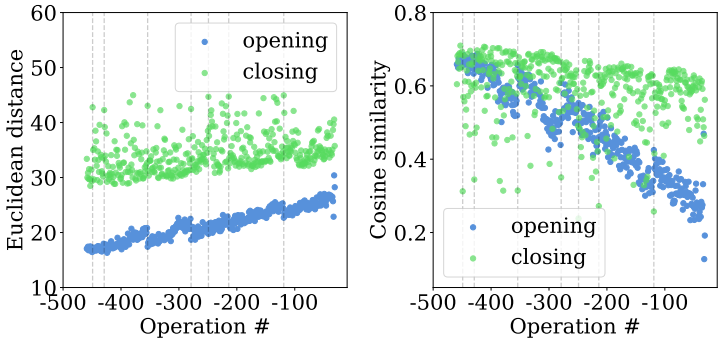


Figure 8.16: Average Euclidean distance and cosine similarity of the acoustic signals from a microphone during opening and closing operations. The vertical dashed lines represent operations with idle time longer than one hour.

Overall, both vibration and acoustic signals can be measured non-intrusively and can be used with similarity-based modules for tracking degradation of this CB. In addition, the variations during opening operations are lower, while the signals recorded during closing operations exhibit greater fluctuations and higher variations in the similarity metrics. This is similar to the results of VCB1 from Section 8.1.3, where the opening operations appear to be more robust and consistent while the closing operations deviate more and have higher variations.

Travel Curve

The first $80\,\mathrm{ms}$ of the travel curves are used to calculated the similarity metrics, which are shown in Figure 8.17. Unlike the results for vibration and acoustic signals, neither metrics show a clear trend across opening and closing operations. Only the last opening operation before failure shows a sudden change, with a Euclidean distance greater than 100 and a cosine similarity lower than 0.999, which fails outside the range displayed in Figure 8.17. Once the travel curve signals begin to deviate, failure occurs immediately in the next operation.

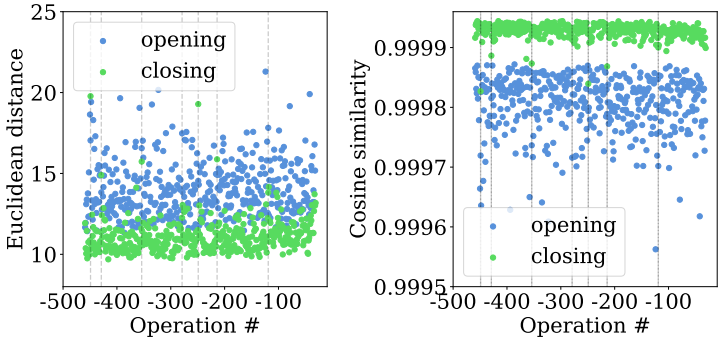


Figure 8.17: Average Euclidean distance and cosine similarity of the first $80\,\mathrm{ms}$ of the travel curves during opening and closing operations. The vertical dashed lines represent operations with idle time longer than one hour. Note that the last opening operation before failure, with a Euclidean distance greater than 100 and a cosine similarity below 0.999, is outside the plot range.

Throughout most of the run-to-failure process, cosine similarity remains high (> 0.999), indicating that contact movement is stable and consistent from one operation to another. Because the signals remain

nearly identical, they fail to capture subtle changes during operations. Interestingly, the variations of the two metrics are larger during opening operations than closing operations, in contrast to the vibration and acoustic cases. This is likely due to unstable motion near the damping region shortly before the contact stops at t_d, as shown in Figure 2.8 for opening operations. The damping of the contact movement around the end of the opening operation is not consistent with the initial part of the contact separation movement, which is more critical for current interruption. In addition, no idle time effects are observed, suggesting that extended inactivity affects mainly the operating mechanism, as seen in the vibration and acoustic signals, rather than the movement of the contacts themselves.

Vibration and Acoustic Spectrograms

Parts of this section are based on the publication [14].

The similarity metrics MSE and SSIM in the time-frequency vibration spectrogram, compared to the first 50 operations (operation #-500 to #-451) for both the opening and closing operations is shown in Figure 8.18. The MSE in both operations exhibit a clear increasing trend, indicating that the difference in vibration patterns between the initial 50 operations and the later operations is growing over time. The first $200\,\mathrm{ms}$ of the vibration signals are converted into spectrogram for investigation.

For opening operations, this trend is similar to the RMS feature in stage O-III from Module A as discussed in Section 8.1.1, where the increasing trend starts linearly and becomes exponential before the failure occurs. This two-mode degradation behavior, first linear and later exponential, can be leveraged for prognostic purposes, as it provides an early indication of failure.

In addition, for closing operations, the idle time effect is evident, with the MSE being higher and the SSIM being lower for operations that have longer idle time, meaning that the vibration patterns in terms of time and frequency domain with long idle time are distinct from the others. These operations with longer idle time could be detected as anomalies but they are conditional anomalies, where the anomalies arise from longer idle time and not CB faulty operating conditions.

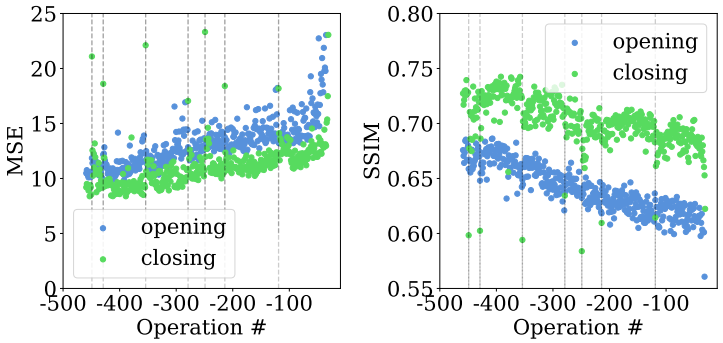


Figure 8.18: Average MSE and SSIM between vibration Mel spectrogram for opening and closing operations. The average similarity (MSE and SSIM) is calculated between the query sample to the first 50 samples. The vertical dashed lines represent operations with idle time longer than one hour.

Similarly, the average similarity metrics calculated from time-frequency spectrogram of microphone signals are shown in Figure 8.19. The first $200\,\mathrm{ms}$ of the microphone signals are converted into spectrogram. When compared to the vibration spectrogram metrics in Figure 8.18, the MSE values from microphone spectrograms during opening operations exhibit a similar linear-exponential degradation trend, which typically indicates imminent failure. However, the exponential phase only spans a limited number of operations. This suggests that the predictive capability of microphone spectrogram MSE is less effective than that of vibration spectrogram MSE, which captures a broader exponential phase, enabling earlier anomaly detection and intervention.

Depending on the application, similarity metrics calculated from vibration and acoustic spectrograms,

both can be measured non-intrusively, can serve as effective indicators for CB condition monitoring. Moreover, these spectrogram-based similarity metrics can help to identify and pinpoint potential fault types by investigating the pixel-wise difference between healthy and new spectrogram; see Section 8.3.2 for more details on fault diagnostics.

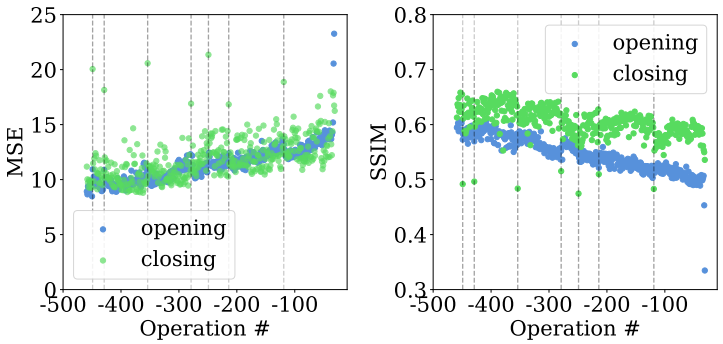


Figure 8.19: Average MSE and SSIM between microphone Mel spectrogram of GCB2 opening and closing operations microphone signals. The average similarity (MSE and SSIM) is calculated between the query sample to the first 50 samples. The vertical dashed lines represent operations with idle time longer than one hour.

8.2.2 MV Gas Circuit Breaker - Run-to-Failure

The first 50 operations are used as healthy baseline ($N_1 = 50$) and the similarity metrics are calculated between these healthy signals and the rest of opening and closing operations of the entire run-to-failure experiment.

Vibration Signals

The two similarity metrics for GCB1 opening and closing operations are shown in Figure 8.20. In this case, instead of directly using the raw one-dimensional vibration signals recorded by accelerometer 353B14, an additional pre-processing step was applied. Specifically, the first $125\,\mathrm{ms}$ of the vibration envelope was extracted using the STE method to smooth the highly non-stationary and high-dimensional vibration signals. Without this pre-processing, these high-dimensional vectors appear to be orthogonal and their cosine similarity is close to zero, due to the sparsity in high-dimensional space.

For opening operations, unlike the case of GCB2 in blue in Figure 8.15, no clear increasing or decreasing trend is observed. However, after operation #4000, the similarity starts to decrease, showing on both metrics, and the variability between operations increase, suggesting that the CB operations become progressively unstable.

For closing operations, the Euclidean distance follows a trend comparable to the RMS values from the feature-based module in Figure 8.11. Since Euclidean distance essentially represents RMS with an offset from the healthy baseline, RMS can serve as a more efficient alternative. It requires less computation and avoids the assumption that the initial samples are healthy. However, defining suitable threshold for triggering alarms remain challenging; further discussion on threshold determination is provided in Section 9.4.2.

This fluctuation of the two metrics of closing operations indicates that GCB1 may have experienced degradation of various non-critical components, while GCB2 may have been affected by a fault in a critical component that directly caused failure. As a result, GCB1 was able to continue operating after the increase in Euclidean distance and decrease in cosine similarity around operation #2200 for more than 4 000 operations, with fluctuations of vibration similarity metrics, before the failure occurs.

Coil Current Signals

The similarity metrics calculated based on the first $30\,\mathrm{ms}$ of the open and close coil current signals are shown in Figure 8.21. For opening operations, the trends are similar to those of the features i_1 and t_2 extracted from open coil current in Figure 8.12, where a gradual change occurs between operation #4600 and #4800. Both the feature-based and the similarity-based modules capture this transition, suggesting a potential fault in a component that influences not only the vibration signals but also the coil current signals.

For closing operations, however, both similarity metrics exhibit high variability and thus are less reliable for assessing CB condition. The consistently low Euclidean distance and high cosine similarity (> 0.9999) indicate that the close coil current signals remain nearly identical throughout the entire run-to-failure experiment, suggesting that the failure had little or no impact on the close coil.

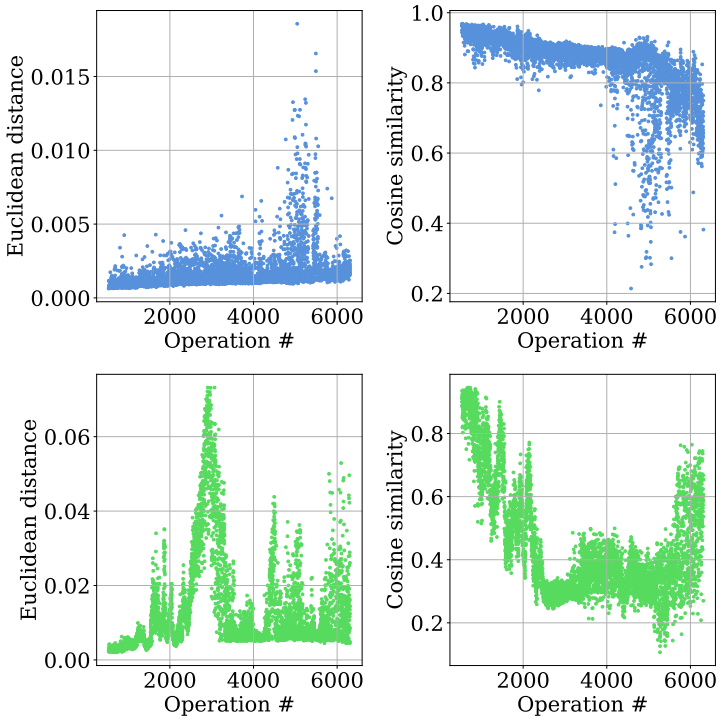


Figure 8.20: Average Euclidean distance and cosine similarity of the first $125\,\mathrm{ms}$ of the vibration signals acquired from the accelerometer 353B14 during opening (blue) and closing (green) operations. Due to high variability, these metrics are challenging to use for reliable condition assessment. Note that in this case, instead of the raw vibration signals, an additional pre-processing step was applied by extracting the vibration envelopes with STE before calculating the similarity metrics.

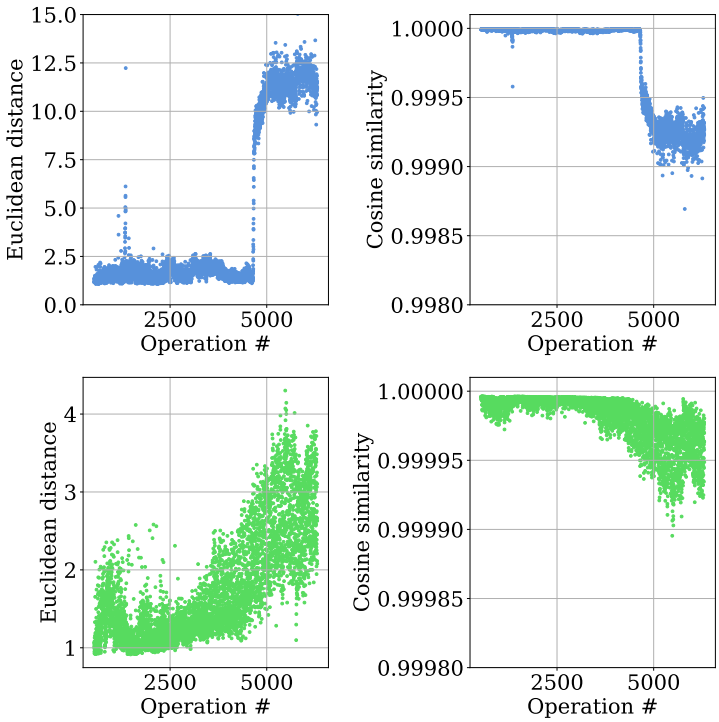


Figure 8.21: Average Euclidean distance and cosine similarity of the first $30\,\mathrm{ms}$ of the coil current signals during opening (blue) and closing (green) operations.

8.3 Machine Learning-based Module

For the ML-based module, both CBs from run-to-failure experiments and CBs with fault injection are considered. Therefore, instead of only tracking the evolution of indicators over operation numbers, this section investigates the feasibility of using the ML-based module for fault detection, segmentation, and diagnostics. It is important to note that in run-to-failure experiments, only a single fault type was observed. As a result, the analysis focuses solely on fault detection, while segmentation or diagnostics are additional to the case of CB with introduced faults.

8.3.1 HV Gas Circuit Breakers - Run-to-Failure

Fault Detection - CAE

The CAE residuals MSE from vibration spectrograms of opening operations are shown in Figure 8.22, exhibiting a trend similar to the average MSE in similarity-based module in Figure 8.18. For training the CAE, the first 70 samples are considered healthy, with 50 used for training and 20 for validation, while the last 500 operations are used for testing and are plotted in Figure 8.22.

Both residual metrics display a two-stage linear-exponential pattern, where values remain stable for approximately 300 operations before transition into an exponential change. This exponential stage is a typically indication of a fault occurrence. This trend makes them effective indicators for condition monitoring, as alarms can be triggered once the exponential stage begins. Thresholds are typically defined from statistics assuming normal distribution as the mean plus and minus three standard deviations of the residuals from the validation set, plotted as two horizontal dashed lines in Figure 8.22. Alternative threshold settings may be applied depending on the application and the criticality of the CB. Further discussion on threshold determination is presented in Section 9.4.2.

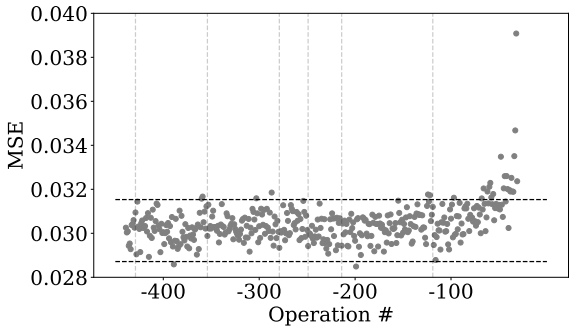


Figure 8.22: The residuals MSE of the CAE trained on 50 healthy samples and tested on the last 500 operations of the run-to-failure experiment for opening operations. The vertical dashed lines represent operations with idle time longer than one hour. The horizontal dashed lines are the mean plus minus three standard deviations of the residuals from the validation set.

Using these thresholds, an alarm would be raised approximately 100 operations before failure. Assuming a CB operates 50 times per year, this corresponds to an early warning approximately two years in advance, giving operators sufficient time to take action. However, relying only on a single indicator (only MSE) increases the risk of false alarms. To achieve more reliable assessment, other indicators from the feature-based or the similarity-based modules should be combined to achieve more reliable assessment.

8.3.2 HV Gas Circuit Breaker - Fault Injection

Parts of this section are based on the publication [15].

In this section, various fault types were artificially induced, enabling an evaluation not only of fault detection, as in run-to-failure experiments, but also of fault segmentation and diagnostics.

Fault Detection - CAE

The CAE residuals as defined in Equation (15) are plotted in Figure 8.23, where healthy samples are colored in green, faulty in red, based on the ground-truth. A horizontal dashed line represents the threshold τ defined in Equation (14) based on the healthy data. False negative samples occur when faulty samples (red) have residuals below the threshold, indicating that the model fails to detect these faults. In this case, the false negative rate is 1.79%. Overall, approximately 98.21% of faulty samples can be detected with the CAE trained only on the healthy samples.

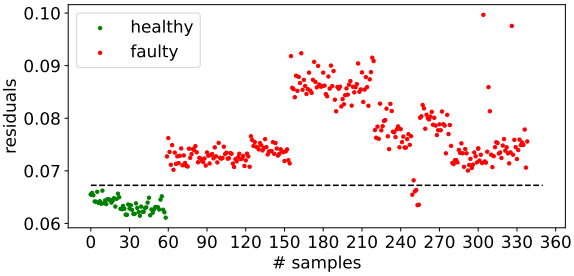


Figure 8.23: The fault detection results based on the CAE residuals with healthy (green) and faulty samples (red) from the ground truth. Horizontal dashed line represents the threshold τ defined in Equation (14).

Fault Segmentation - Offline Clustering

For simplicity, we first consider an offline clustering setting where the full dataset is available. Clustering results obtained by K-means and OPTICS are shown in Figure 8.24, using t-Distributed Stochastic Neighbor Embedding (t-SNE) to map the high-dimensional data into a two-dimensional space. Colors represent the clusters identified by the clustering algorithm, while marker numbers correspond to the ground-truth labels defined in Table 6.4. For K-means, the black, green, and yellow clusters exhibit clear separation, while the blue and purple clusters show slight overlap. Some samples are incorrectly assigned to other clusters (e.g., purple 4s or blue 5s). However, both blue and purple clusters primarily contain samples in Condition #4 and #5, representing low spring faults and differing only in damper conditions. OPTICS (on the right of Figure 8.24), however, failed to distinguish between these two clusters and assigned all samples from these two conditions to a single large cluster and a small cluster. No additional sub-clusters are visible within the blue and purple clusters, indicating that it is challenging to further separate the fault sub-types such as different levels of degraded damper (between kinematic viscosity $100\,\mathrm{mm}^2/\mathrm{s}$ and $120\,\mathrm{mm}^2/\mathrm{s}$) as described in Table 6.4.

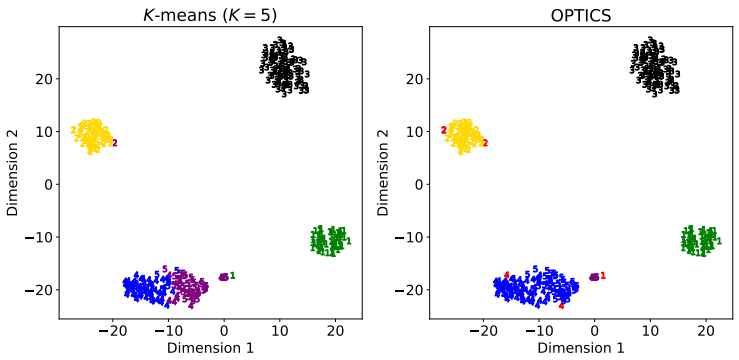


Figure 8.24: Offline clustering results using K-means (left) and OPTICS (right) with the CAE latent features, visualized in 2D using t-SNE. Colors are assigned from the clustering results, while markers are the ground-truth conditions as defined in Table 6.4: 1 - nSnD, 2 - nSdD, 3 - hSnD, 4 - lSnD, 5 - lSdD. Red samples in OPTICS clustering results correspond to the outliers.

Clustering performance metrics, including the ARI score, homogeneity score h, completeness score c, and v-measure v, as described in Section 7.6.1, are summarized for both clustering methods in Table 8.4. K-means has higher scores across all four metrics, with all four metrics exceeding 0.9. However, OPTICS has lower scores because of the misclassification of two different damper conditions under low spring conditions. Despite this, OPTICS offers an advantage over K-means: it does not require specifying the number of clusters, which is beneficial in real-world applications, where the number of clusters is typically unknown.

Table 8.4: Clustering performance of the K-means and OPTICS clustering methods. The symbol $\uparrow$ means the higher the value is, the better separated the clusters. The best score is 1 for all four metrics, where clusters are well separated.

Clustering method	ARI $\uparrow$	$h\uparrow$	$c\uparrow$	$v\uparrow$
K-means	**0.9172**	**0.9137**	**0.9136**	**0.9137**
OPTICS	0.8018	0.8366	0.8996	0.8670

The confusion matrix of the K-means results is shown in Table 8.5 as it achieves the highest scores in Table 8.4. As shown in Figure 8.24, the majority of misclassified samples occur between Condition #4 (lSnD) and #5 (lSdD). It is important to note that the clustering results do not inherently indicate which cluster corresponds to which fault label. This confusion matrix serves only for evaluation purposes,

Besides K-means and OPTICS, the clustering performance of the SOM with grid size $(10, 10)$ is shown

Table 8.5: Confusion matrix of the K-means clustering results with $K = 5$. Note that the ground-truth labels are unavailable in real-world scenarios, and one does not know which cluster corresponds to which condition.

		Prediction				
		1 - nSnD	2 - nSdD	3 - hSnD	4 - lSnD	5 - lSdD
Actual	1 - nSnD	60	0	0	0	0
	2 - nSdD	0	59	0	0	1
	3 - hSnD	0	0	96	0	0
	4 - lSnD	0	0	0	58	7
	5 - lSdD	0	0	0	6	53

in Figure 8.25 for the entire dataset in an offline setting. On the left of Figure 8.25, the U-matrix is presented, indicating the distance between neighboring cells with the projected samples. On the right side, the SOM cells are colored by class assignments. Quantitative evaluation of the SOM was performed using metrics discussed in Section 7.6.1. The homogeneity score h is 0.9564, higher than K-means and OPTICS as shown in Table 8.4. The map properly approximates the data distribution and is well-organized, with quantization and topographic errors of 0.1383 and 0.0559 respectively, and a topographic product equal to 0.0101, close to zero.

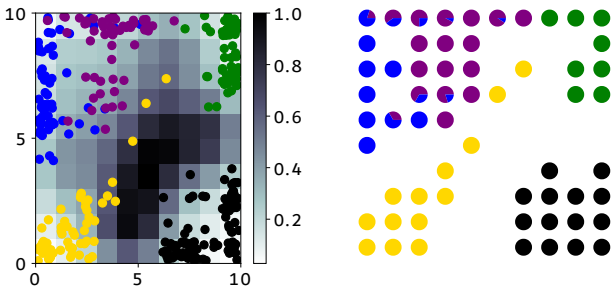


Figure 8.25: Offline clustering results using SOM with grid size (10, 10), colored by the ground-truth labels. On the left, the U-matrix indicates the distance between neighboring cells with the projected samples. On the right, the SOM cells are colored by class assignments.

Fault Segmentation - Online Clustering

In real-world applications, the complete dataset is not available initially in most cases, and new data are rather being incrementally streamed from substations with each CB switching operation. Thus, we consider an online clustering setting where new fault types potentially appear over time. In this setting, OPTICS and SOM are more suitable as they can better adapt to new incoming data, unlike K-means, which requires the number of clusters to be predefined at each step. In Figure 8.26 and Figure 8.27, we depict the online clustering results for OPTICS and SOM over time. The title of each subfigure denotes the data distribution available for each label defined in Table 6.4. The samples available at each time step of the data stream are assigned arbitrarily.

Initially, the CAE is trained with only healthy data, resulting in the formation of a single cluster, as depicted in Figure 8.26 (a) and Figure 8.27 (a). Subsequently, 20 new samples were collected, consisting of 10 Condition #2 (nSdD) and 10 Condition #3 (hSnD) samples. As shown in Figure 8.26 (b) and Figure 8.27 (b), both clustering algorithms identified two new clusters (black and yellow), potentially indicating two distinct fault types. Notably, some samples are marked in red in the case of OPTICS, representing outliers that the clustering algorithm could not assign to any cluster. Later, another batch of 40 samples (20 additional samples for Condition #2 and #3 each) was collected and the clustering results are shown in Figure 8.26 (c) and Figure 8.27 (c).

Interestingly, in Figure 8.26 (d), the cluster for Condition #1 splits into two sub-clusters, even though

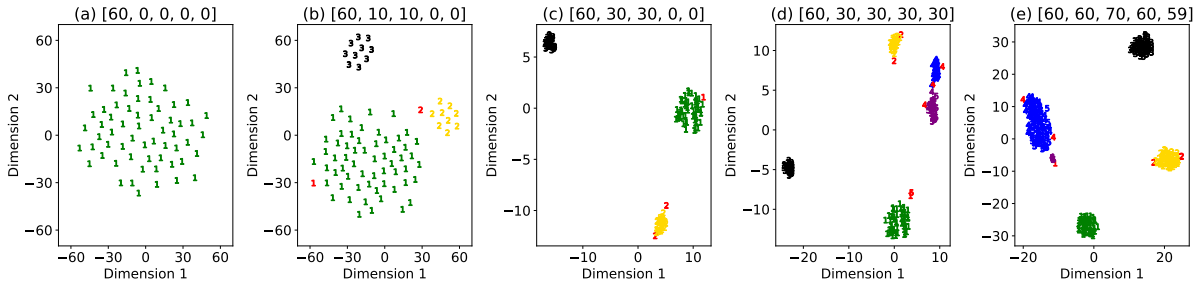


Figure 8.26: Clustering results using OPTICS with the CAE latent features over an incremental data stream (from (a) to (e)), visualized in 2D space using t-SNE. Colors are assigned from the clustering results, while markers are the ground-truth conditions as defined in Table 6.4: 1 - nSnD, 2 - nSdD, 3 - hSnD, 4 - lSnD, 5 - lSdD. The subfigure titles indicate the number of samples available in each class at each step of the data stream. For example, in (a) we have 60 samples from Condition#1 (nSnD).

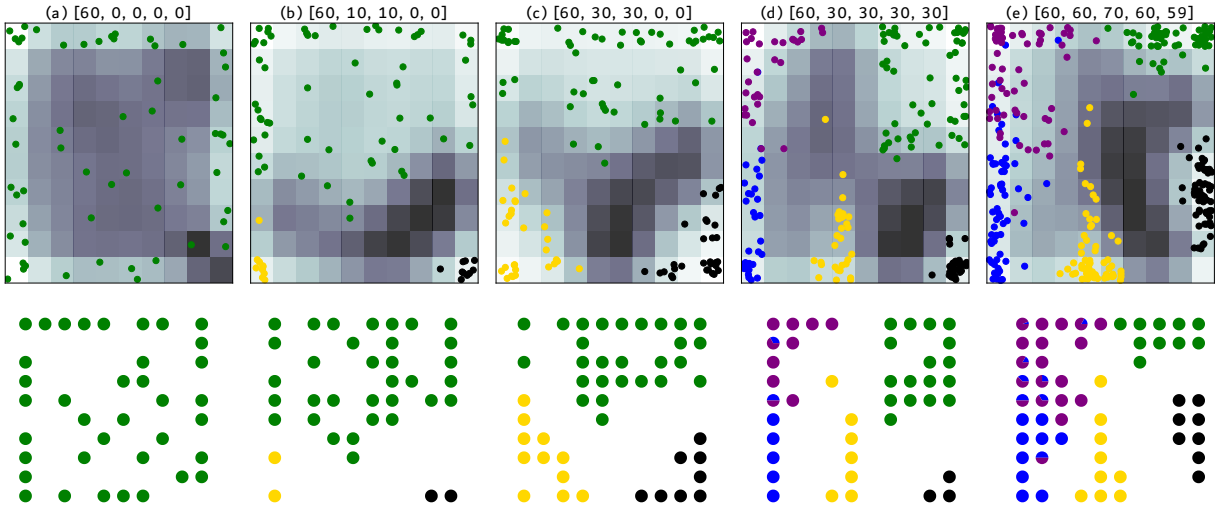


Figure 8.27: Clustering results using SOM with the CAE latent features over an incremental data stream (from (a) to (e)). Top row: U-matrix (indicating distance between neighboring cells) with projected data samples. Bottom row: map cells colored by class assignments. Colors are assigned from the ground-truth conditions as defined in Table 6.4: green - nSnD, yellow - nSdD, black - hSnD, blue - lSnD, purple - lSdD. The subfigure titles indicate the number of samples available in each class at each step of the data stream.



they are still considered as a single cluster by the clustering algorithm. After inspecting the ground-truth labels, it becomes evident that these sub-clusters correspond to two experimental blocks conducted on different days. This suggests that the healthy condition can deviate because of varying experimental conditions such as room temperature and gas pressure. However, the deviations between faulty and healthy conditions are considerably larger compared to the variations observed among healthy samples.

As shown in Figure 8.26 (d) and Figure 8.27 (d), new faulty samples result in two new clusters. However, in Figure 8.26 (e) and the clustering results of the full dataset on the right of Figure 8.24, the purple and blue clusters merge into a single large blue cluster and a small purple cluster. Similarly, the purple and blue clusters are close to each other and do not have a clear boundary in Figure 8.27 (e). This demonstrates that even with a limited number of faulty samples from the online data streaming process – a scenario commonly encountered in real-world applications – the proposed framework remains effective. It can still successfully segment most faulty samples into their corresponding clusters, ensuring reliable fault identification even under data scarcity.

We have demonstrated the feasibility of using different clustering methods with our proposed framework. The selection of the optimal clustering methods in real-world applications depends on the specific use case as different algorithms highlight different cluster properties. Cluster analysis is usually an interactive process, where users explore the underlying structure of the data distribution. Due to its unsupervised nature, defining a unique optimal clustering solution is challenging, as no ground-truth is available in practice. Thus, the selection of the optimal clustering methods (such as K-means, density-based OPTICS, or SOM-based clustering) is highly application-dependent. Users may need to apply and combine multiple clustering methods to uncover and identify fault types or fault sub-types in the data effectively.

Fault Diagnostics - Explainable Artificial Intelligence (XAI)-guided Diagnostics

This section evaluates the performance of fault diagnostics using XAI, focusing on the results of K-means with $K = 5$ for conciseness. First, the cluster centroids in the CAE latent space are used to identify a set of representative instances, which are the data points closest to each centroid. These instances are considered the most representative samples for each condition. The vibration signals of these samples in the axial direction, along with their corresponding spectrograms, are presented in the first and the second rows of Figure 8.28, namely in Figure 8.28 from (a1) to (e1) and from (a2) to (e2).

Before applying the XAI methods for fault diagnostics, we introduce an initial analysis step by computing the pixel-wise differences between the healthy and faulty normalized spectrograms, represented as $\boldsymbol{x_f} - \boldsymbol{x_h}$. These differences, shown in Figure 8.28 (b3), (c3), (d3), and (e3), provide an initial fault visualization. Here, $\boldsymbol{x_f}$ represents the faulty spectrogram, while $\boldsymbol{x_h}$ denotes the healthy spectrogram. Red and blue regions indicate areas where the faulty spectrogram exhibits higher or lower values, respectively, compared to the healthy reference.

Under low spring tension conditions (Condition #4 and #5), as shown in Figure 8.28 (d3) and (e3), the spectrogram differences have similar patterns, with higher values around $200\,\mathrm{ms}$, particularly in the high frequency regions, and lower values after $300\,\mathrm{ms}$ compared to the healthy spectrogram. In contrast, under high spring tension (Condition #3), the increased stiffness reduces vibration amplitude, leading to a shorter vibration duration and faster damping, as seen in the vibration signals in Figure 8.28 (c1). This is reflected in the spectrogram differences, where lower values appear around $100\,\mathrm{ms}$, and the red and blue regions are inverted compared to the low spring tension condition. Similarly, when the damper degrades and its viscosity decreases, the vibration amplitude increases, as shown in Figure 8.28 (b1) and (e1). In these cases, red regions appear more prominently in the higher frequency areas, indicating a stronger vibration response due to reduced damping efficiency.

The XAI method, Integrated Gradients, as described in Section 7.5.3, is applied to the trained classifier to generate attribution maps and diagnostics matrices, providing interpretability for the cluster assignment obtained from the fault segmentation step. Higher attribution values in these maps highlight the features that contribute most to assigning a sample to a specific cluster. By analyzing these maps, domain experts can identify potential fault types by recognizing similarities and differences across conditions. The diagnostics matrix for each faulty condition is presented in Figure 8.28 (b4), (c4), (d4), and (e4).

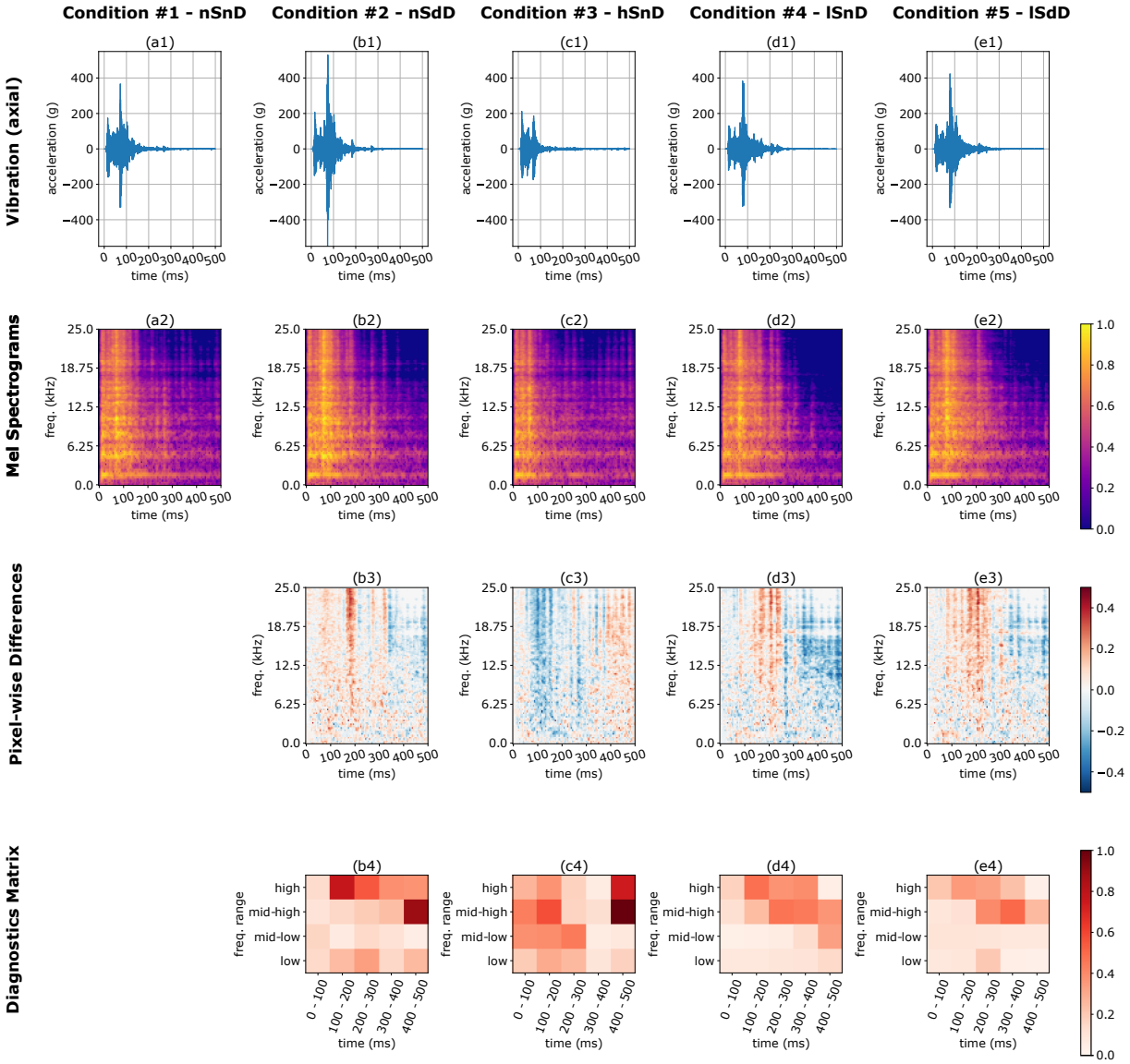


Figure 8.28: The representative instances for each condition are selected as the closest samples to each cluster centroid in the CAE latent space. Each column corresponds to different condition: (a) Condition #1 nSnD, (b) Condition #2 nSdD, (c) Condition #3 hSnD, (d) Condition #4 lSnD, and (e) Condition #5 lSdD. Each row represents different figures: 1. vibration signals in the axial direction, 2. corresponding Mel spectrograms, 3. corresponding pixel-wise differences between faulty and healthy spectrograms, 4. diagnostics matrix using max pooling based on attribution maps. Note: No difference spectrogram or diagnostics matrix is provided for the healthy condition (Condition #1).

The diagnostics matrices in Figure 8.28 (d4) and (e4) suggest that these two samples correspond to similar fault types, as indicated by their similar diagnostics matrices. High attribution values are observed between $100\,\mathrm{ms}$ and $300\,\mathrm{ms}$ in the high-frequency regions and between $200\,\mathrm{ms}$ and $400\,\mathrm{ms}$ in the mid-high-frequency regions, highlighting shared fault characteristics. In Figure 8.28 (b4), the presence of a red region around $200\,\mathrm{ms}$ suggests an additional vibration event occurring across all frequency ranges. The diagnostics matrix further reinforces this observation, as the highlighted high-frequency region between $100\,\mathrm{ms}$ and $300\,\mathrm{ms}$ indicates that this additional event plays a key role in cluster assignment during the fault segmentation step. These diagnostics matrices enhance the interpretability of the fault segmentation results obtained from unsupervised clustering methods, providing valuable insights into the distinguishing features of different fault conditions.

To further evaluate the faithfulness of the XAI attribution maps, the changes in the classifier's prediction confidence are represented in Figure 8.29 for both random occlusion and attribution-based occlusion, as described in Section 7.6.1. We gradually occlude between 0% (original spectrogram) and 30% of the total input features in the spectrograms by replacing them with zeros. For random occlusion, features are occluded randomly, while for attribution-based occlusion, features are selected in descending order of their attribution values. In both cases, the prediction delta Δ increases with the percentage of occluded features, but the curve is significantly higher for the attribution-based occlusion. The changes in predictions are higher for attribution-based occlusion than for random occlusion, confirming that the features with higher attribution values identified by the XAI method are indeed important for the assignment to a specific cluster.

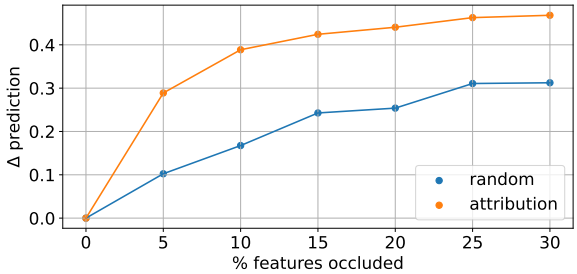


Figure 8.29: Faithfulness of the explanations evaluated by representing the change in classifier prediction confidence (Δ) as a function of the percentage of features (pixels in spectrogram) occluded, averaged over the entire dataset. The impact is higher for attribution-based occlusion than for random occlusion, showing that the features with higher attribution values are indeed important.

Contribution of each Sensor to Fault Segmentation

In this section, we examine the significance of each vibration direction and microphone in distinguishing between different faults when performing fault segmentation using K-means. We report four evaluation metrics in Table 8.6: ARI score, homogeneity score h, completeness score c, and v-measure v, as described in Section 7.6.1.

Using signals recorded from all three accelerometers and one microphone achieved the highest scores among all settings, with all four evaluation metrics exceeding 0.9, indicating well-separated clusters. In contrast, the worst performance is observed using only the microphone signals. Comparable performances are achieved using only one accelerometer. This discrepancy may stem from the fact that the microphone is not directly mounted on the CB structure, leading to a loss of information during the transmission of vibrations through the air. Unlike the accelerometers, which are directly mounted on the CB, the microphone signal is more prone to coupling with environmental noise. The direction of the accelerometer installation does not show a significant difference based on this experimental dataset. However, installation in the vertical and axial directions performs better than in the horizontal directions.

In summary, to best distinguish between the fault types, all four sensors, including three accelerome-

ters and one microphone, should ideally be used. However, the sensors installed in different directions contain highly redundant information. Using only the vertical or axial accelerometers yields comparable clustering performance for distinguishing faulty samples. Considering installation costs and practicality, installing an accelerometer in the axial direction is the preferred option for this experimental setup. Alternatively, a single vibration sensor capable of measuring three-directional vibrations could also be considered.

Table 8.6: Influence study on sensors. hor: accelerometer in horizontal direction, ver: accelerometer in vertical direction, axi: accelerometer in axial direction, mic: microphone. The symbol ↑ means the higher the value is, the better separated the clusters. The best score is 1, where clusters are well separated.

Sensor(s)	ARI ↑	h ↑	c ↑	v ↑
hor, ver, axi, mic	**0.9045**	**0.9013**	**0.9018**	**0.9015**
hor	0.8287	0.8237	0.8245	0.8241
ver	0.8607	0.8587	0.8651	0.8619
axi	0.8673	0.8737	0.8811	0.8774
mic	0.7839	0.8018	0.8063	0.8040

8.3.3 MV Gas Circuit Breaker - Run-to-Failure

Fault Detection - CAE

The residuals of CAEs trained on the first 50 assuming healthy operations for both opening and closing operations and the corresponding thresholds determined by the validation 20 operations are shown in Figure 8.30. Unlike the case for GCB2 in Figure 8.22 shows a typically linear-exponential pattern, the residuals show a high variations across the run-to-failure process.

For closing operations, the residuals decrease slightly during the first 1 500 operations, then increase until around operation #3000, corresponding to the rise in vibration RMS observed in Figure 8.11(a). Afterward, the residuals remain high, mostly above the threshold, and increase further beyond operation #5000 until failure occurs.

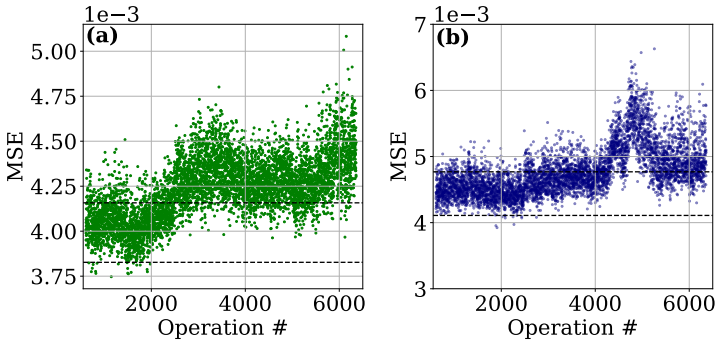


Figure 8.30: The residuals MSE of CAEs trained on vibration spectrograms for (a) closing and (b) opening operations of GCB1. The CAEs were trained on 50 samples, validated on 20 samples and test on the rest of the samples during run-to-failure experiment.

For opening operations, the residuals capture the changes in vibration events. During the first approximately 4 000 operations, the residuals remain mostly within the thresholds, suggesting that the typical four key vibration events as shown in Figure 8.10 are preserved. However, deviations in vibration signals emerge around operation #4500 with some extra events visible, leading to an increase in residuals. As shown in Figure 8.10, additional events appear between $40\,\mathrm{ms}$ and $60\,\mathrm{ms}$ in operation #5000. This rise in residuals aligns with the drop in certain features such as key moments t_{o1} and t_{o2} in Figure 8.9 when using the feature-based module. By operation #6000, the vibration pattern reverts to the four-event structure as shown in Figure 8.10, causing the residuals to decrease again.

For CBs with a high number of operations such as across a run-to-failure process, thresholds may need to be adjusted dynamically rather than static relying only on the first few operations. Using the mean plus minus three standard deviations as shown in Figure 8.30 results in residuals of many samples falling outside this range even in the beginning of the experiment. This suggests that such thresholds cannot provide reliable condition assessment and cause lots of false alarms.

It is important to note that a decrease in residuals does not indicate that the CB has returned to a healthy state. Instead, it suggests that the new samples share similar representations in the CAE latent space with the healthy baseline samples, even though the underlying conditions may differ. Consequently, additional indicators are required to achieve a more robust assessment.

8.3.4 HV Gas Circuit Breakers - In Substation

To validate the ML-based module in real-world applications, fault detection for three HV GCBs (GCB5, GCB7, and GCB8) in a substation is investigated in this section. These CBs are of the same type and operate under similar conditions. They are also monitored with the same monitoring systems, while

GCB6 is monitored with an updated version of the IoT box and thus is not included here. The vibration and acoustic sensors were also installed in the same position on the CBs; therefore, a CAE was trained on three CBs. The details about the data collection setup are described in Section 6.7.

Fault Detection - CAE

The residuals of the trained CAE using vibration spectrograms collected during closing and opening operations are shown in Figure 8.31. For both cases, even with the same CB types, sensor installation positions, and the same monitoring systems, the difference between CBs can still be observed where the model performs better for GCB5 with lower residuals in the first 25 samples for closing and first 20 samples for opening operations, while the other two CBs have relatively higher residuals. The implementation details about the CAE and the train-validation-test split are summarized in Section 7.6.3.

The thresholds are determined from the validation sets, assuming they are healthy, and marked in gray horizontal lines. They are the mean plus and minus three times the standard deviations from the residuals of the validation set. All test samples have residuals within the threshold range, indicating that for closing operations, they are all in a healthy state and do not have high deviations. However, for opening operations, there is one anomaly detected from GCB7 with high residuals above the threshold, because the signals recorded for this operation were corrupted. Instead of $120\,000\,\mathrm{sample}$ points, it contains only $109\,204\,\mathrm{sample}$ points, with a much shorter pre-trigger time, potentially due to the short operation interval between two operations, where the previous measurement was taken $26\,\mathrm{s}$ before the corrupted measurement.

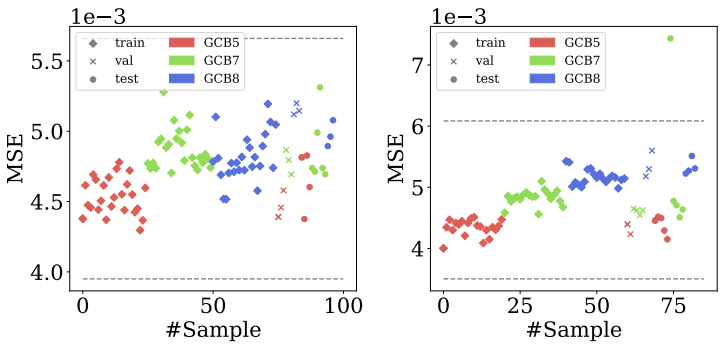


Figure 8.31: The residuals MSE of CAEs trained on vibration spectrograms for closing (left) and opening (right) operations of CBs in the substation. Two horizontal lines correspond to the thresholds, the mean plus and minus three times standard deviations of the residuals from the validation set. The samples in red correspond to GCB5, green to GCB7, and blue to GCB8. The diamond (⋄) is the training set, cross (x) for the validation set, and circle (o) for the test set.

This section presents the capability of the ML-based module to assess CB condition and detect anomalies in real-world applications under a data scarcity scenario. In this case, the training data were collected from three CBs of the same type over approximately one year. However, the low operation frequency remains a challenge for applying ML-based or other data-driven methods in practical CB monitoring applications.

8.4 Integrated Module

This section investigates the application of integrating all three modules, instead of using each module individually. For every operation and for each indicator, a z-score is calculated to quantify the degree of deviation from the healthy baseline. A z-score of 1 for a given indicator indicates that the corresponding indicator value from the new operation is one standard deviation above the mean of the baseline data.

Two run-to-failure CBs with different types are presented here to demonstrate the feasibility of integrating the modules of the proposed framework. To reflect real-world applications, only non-intrusive signals are considered in this section.

8.4.1 HV Gas Circuit Breakers - Run-to-Failure

The opening operations of GCB2 were monitored using 14 indicators derived from non-intrusive signals, including five from the feature-based module, eight from the similarity-based module, and one CAE residual calculated using vibration spectrograms from the ML-based module. These indicators are summarized in Table 8.7 with the corresponding z-scores shown in Figure 8.32. These z-scores are calculated with respect to the first 50 operations as the healthy baseline. For the ML-based module, however, the scores are calculated using the validation set with 20 samples.

Table 8.7: Details of the 14 indicators from all three modules used to assess the condition of GCB2 for opening operations. F-based: feature-based module; S-based: similarity-based module; Euc.: Euclidean distance; cos.: cosine similarity.

Module	#	Indicator	Module	#	Indicator
F-based	1	vibration RMS	S-based	8	vibration MSE
	2	vibration peak		9	vibration SSIM
	3	coil current i_3		10	microphone MSE
	4	coil current t_3		11	microphone SSIM
	5	microphone var.		12	coil current Euc.
S-based	6	vibration Euc.		13	coil current cos.
	7	vibration cos.	ML-based	14	vibration residual

The upper part of Figure 8.32 shows approximately 450 to 250 operations before failure, where the z-scores remain relatively stable below 3. As the number of operations increases, the z-scores begin to rise. The lower part of Figure 8.32 displays the last 230 operations before failure. In this stage, the z-scores exceed 5 or even 10, indicating deviations more than five to ten times the standard deviation of the healthy baseline. Most indicators show a gradual increase in z-scores, reflecting a progressive deviation of the operations from the healthy baseline. As the failure approaches, nearly all indicators exceed a z-score of 5, marked with the darkest color in Figure 8.32.

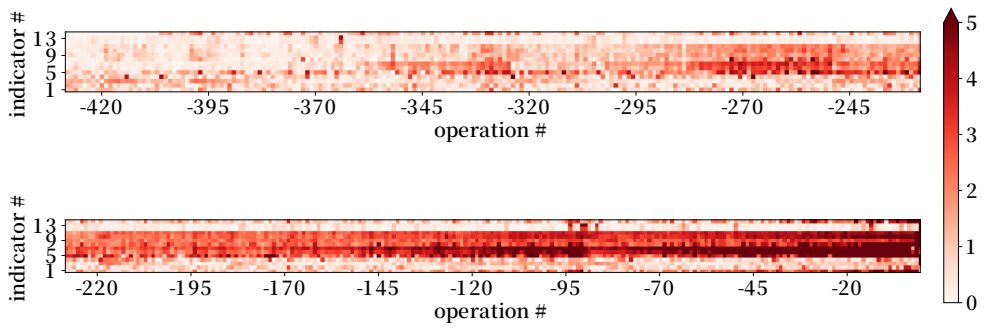


Figure 8.32: Results of applying the integration of all three modules with z-score for approximately the last 400 operations during the run-to-failure experiment for GCB2 opening operations with z-scores beyond 5 colored in the darkest color. The 14 indicators used are summarized in Table 8.7.

The z-score for each operation shown in Figure 8.32 can be used to monitor CB condition in practical applications, but thresholds must be defined to trigger inspections or corrective actions. Instead of relying on raw indicator values, z-scores provide a normalized basis for threshold determination. For example, a simple rule could be: if any indicator exceeds a z-score of 3 for two consecutive operations, an alarm is raised, and an inspection should be performed. In addition, multiple threshold levels can be defined to correspond to different actions depending on severity. For critical assets, lower thresholds may be applied to enable earlier warnings and timely intervention, whereas for CBs of lower criticality, high thresholds can be used.

8.4.2 MV Gas Circuit Breaker - Run-to-Failure

The opening operations of GCB1 were monitored with all three modules using the 12 selected indicators summarized in Table 8.8, including seven from the feature-based module, four from the similarity-based module, and one from the ML-based module. Their corresponding z-scores from the four selected stages during the run-to-failure process are shown in Figure 8.33. For clarify, only four subplots are shown, each representing 250 operations at different stages of the run-to-failure experiment.

Table 8.8: Details of the 12 indicators from all three modules, derived from non-intrusive signals, used to assess the condition of GCB1 opening operations. F-based: feature-based module; S-based: similarity-based module; Euc.: Euclidean distance; cos.: cosine similarity.

Module	#	Indicator	Module	#	Indicator
F-based	1	vibration RMS	S-based	8	vibration Euc.
	2	vibration t_{o1}		9	vibration cos.
	3	vibration t_{o2}		10	coil current Euc.
	4	vibration t_{o3}		11	coil current cos.
	5	vibration t_{o4}	ML-based	12	vibration residual
	6	coil current i_1			
	7	coil current t_2			

The first subplot corresponds to the early stage (operation number < 1000), where most indicators maintain low z-scores below 3, indicating that the CB operations remain similar to the healthy baseline and show no large deviations. The second subplot illustrates operations around #2500, where several indicators begin to show higher z-scores compared to the first subplot.

The third subplot captures the potential fault initiation around operation #4700, where many indicators exceed z-scores of 5, highlighted by the darkest color in Figure 8.33. Around operation #4700 with the high z-scores, the CB may enter a faulty state while still able to operate, with most indicators remaining consistently above 5 for several hundred operations until failure.

In practical applications, operations should be stopped around operation #4700 with inspections performed. However, since the objective here is to investigate mechanical degradation, the CB continues to operate without maintenance. The fourth subplot illustrates the last 250 operations before failure, where nearly all indicators reach z-scores above 5, shown with the darkest color, suggesting that the CB is in a faulty state while still able to keep no-load operation for hundreds of operations.

This patterns resemble the results for GCB2 in Figure 8.32, where for most indicators, the z-scores increase with the increase of operation numbers. However, unlike GCB2 with a gradual transition from healthy to faulty state, the transition from healthy to faulty state for this CB occurs rather abruptly, within only a few operations around #4710. This suggests that the emerging fault has a significant impact on CB operation and changes the operation patterns.

These two case studies suggest that while degradation trajectories and patterns vary across CB types and fault types, the general trend of the deviation from the healthy baseline with increasing z-scores can be observed and leveraged for triggering alarms and performing inspections or corrective actions before the CB ultimately fails.

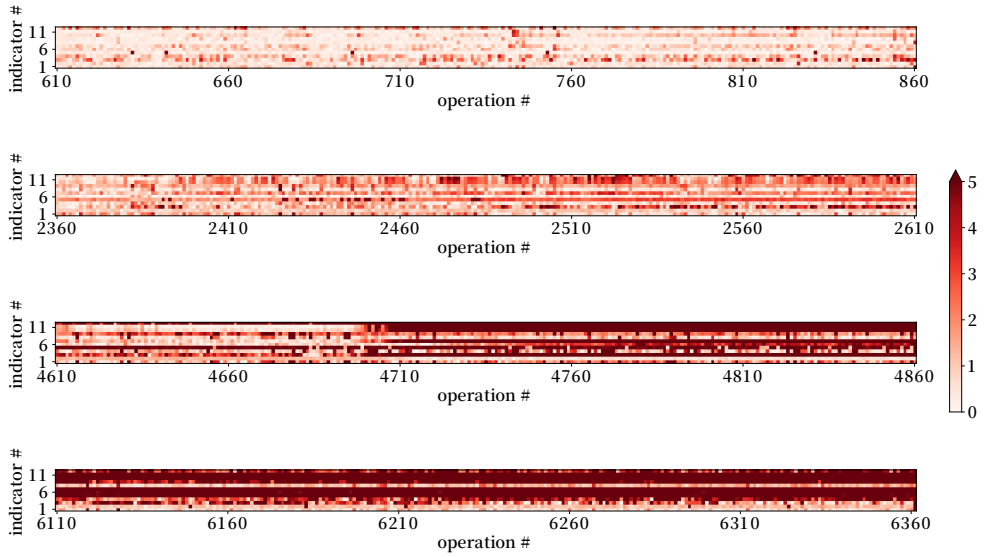


Figure 8.33: Results of applying the integration of all three modules with z-score for the entire run-to-failure experiment for GCB1 opening operations. The indicators used here are summarized in Table 8.8.

8.4.3 Summary of the Integrated Module Applications

The effectiveness of the proposed framework, combining three modules and using solely non-intrusive signals, has been demonstrated through two run-to-failure experiments on two CBs. The framework is both flexible and extendable, accommodating varying numbers of indicators, particularly those derived from domain knowledge. Furthermore, comprehensive action lists can be defined based on different threshold levels, degrees of deviations, and the specific indicators involved.

In the two case studies presented in this section, pre-selected sets of indicators were analyzed. However, in real-world applications, where neither the fault type nor the most relevant indicators are known in advance, monitoring a large set of indicators is preferable to relying on a small, fixed subset. This increases the likelihood of capturing signal deviations associated with diverse fault types. Further discussion on the framework with integrated modules and its practical applications is provided in Section 9.2.

9 Discussion

A three-module CB condition monitoring framework has been proposed and applied on different CB types. This chapter summarizes the key findings of this work connected to the aims of this work discussed in Section 5 and provides answer to the research questions outlined in Section 1.3.

9.1 Continuous CB Condition Monitoring

The first aim of this work was to identify key indicators for continuously monitoring CB conditions using non-intrusive signals, particularly vibration and acoustic signals. This has been validated through laboratory run-to-failure experiments on multiple CBs. Different indicators extracted from these signals, such as key moments from vibration signals, reflect distinct aspects of CB operation and reveal different degradation patterns. Some indicators show no change during degradation and are therefore not suitable for condition monitoring, while others exhibit continuous increasing or decreasing trends, making them more effective for condition monitoring and anomaly detection.

However, variability in operating conditions, such as idle time and spring load, can significantly affect the collected signals and lead to different patterns even under healthy states when operating conditions change. Therefore, to achieve a more robust assessment, it is important to incorporate operating conditions information alongside the condition monitoring signals. For instance, binary or categorical variables can be used to describe spring load conditions and other operating conditions. These information should also include the basic CB characteristics, such as the number of operations, the year of installation, and maintenance activities.

The first aim of this work also includes identifying suitable sensors for continuously monitoring CB conditions. In this work, several non-intrusive sensors were investigated, including accelerometers, microphones, and current sensors. While signals collected from all of these sensors can reflect CB condition, their effectiveness varies depending on the specific CB type and fault type.

The feasibility of interpreting and utilizing vibration signals for monitoring CB condition has been demonstrated with all three modules. One challenge, however, lies in identifying optimal sensor installation positions and orientations as discussed in Section 6.8.2. The installation locations strongly influence the quality and type of information captured. Placing a sensor too close to the operating mechanism results in a high vibration amplitude of even beyond $1000\,\mathrm{g}$, requiring sensors with a higher measurement range. These sensors are not only more expensive but also have typically lower sensitivity in the lower amplitude regions. In contrast, installing a sensor too far from the operating mechanism leads to only damped signals with limited information for tracking degradation.

One possible solution to determine optimal installation location and orientation is to deploy multiple vibration sensors at different locations, which may provide richer information but also increases installation complexity and cost. Alternatively, a practical approach is to have multiple vibration sensors with temporary fixation methods, such as C-clamps or magnetic mounts, and place them at various locations on the CB. By performing a test operation, the collected signals can be visually inspected, and the location that has the most distinct vibration waveforms can be selected for permanent installation.

Acoustic and coil current signals can also be used for monitoring CB condition, but their capabilities are more limited. When applying the feature-based and similarity-based modules to coil current signals, the resulting indicators often show either sudden changes or no clear trends, reducing their usefulness for condition monitoring. Indicators extracted from acoustic signals exhibit similar patterns to vibration signals but are typically more sensitive to environmental noise. Therefore, unless installing vibration sensors is not feasible, vibration sensors are recommended over microphones. Alternatively, both sensors can be deployed together as a complementary solution.

In summary, continuous monitoring of CB mechanical degradation using non-intrusive signals is feasible based on the laboratory experiments, but with some additional considerations required, such as including operating conditions.

9.2 Effectiveness of the Proposed Framework

The third aim of this work, as defined in Chapter 5, was to develop a condition monitoring framework for CBs, which has been accomplished. This section discusses key findings from applying the proposed framework to monitor CB condition, including implementation considerations that need to be considered for practical deployment.

9.2.1 Feature-based Module

The feature-based module relies on domain knowledge to identify which features should be investigated and offers more interpretable results, compared to the other two modules. For instance, the feature RMS extracted from the vibration signals represent the vibration energy. It is useful for monitoring condition of GCB2 (Figure 8.3 and Figure 8.4), because it shows linear-exponential degradation trends, but not for GCB1 (Figure 8.11), exhibiting only fluctuating trends. This means that certain features may be effective for a specific combination of CB-fault type, and operation conditions, but not for others.

Moreover, features derived directly from the vibration peak, such as peak-to-peak or impulse factor, are not reliable unless pre-processing is applied to remove EMI spikes. These spikes can have higher amplitude than the true signal peak, making it difficult to distinguish genuine signals from noise. Run-to-failure experiments also show that peak values vary over time with CB conditions, meaning that the measurement ranges of the data acquisition systems have to be adapted. If the range is too narrow, peaks may be clipped; if too wide, low-amplitude vibrations may be mixed with noise. As a result, peak-based features can be distorted and may fail to represent the CB condition, requiring caution when used in practice.

Features extracted from different condition monitoring signals, both intrusive and non-intrusive, exhibit distinct degradation trends, as shown in Section 8.1 and particularly in Section 8.1.1. These trends can be categorized into three types: no change, gradual increase or decrease, and sudden change. Among them, gradual trends are the most suitable for condition monitoring purposes, particularly when fluctuations of feature values under the healthy state are low, as they provide a stable baseline and enable early intervention. Some features may appear to fluctuate as if the CB is "recovering" and returning to normal operation. In reality, however, this is not the case, but it only implies that such features do not fully capture the CB condition. This underscores the importance of monitoring a broad set of features rather than relying only on a few.

9.2.2 Similarity-based and ML-based Module

The similarity-based module has been shown to be effective for tracking changes in CB condition. However, due to the high dimensionality of raw time-series signals, pre-processing is recommended before applying this module. Techniques such as filtering or smoothing (e.g., STE or moving average), or dimension reduction (e.g., PCA or downsampling) help mitigate the curse of dimensionality, where two high-dimensional vectors may appear almost unrelated and have nothing in common.

The ML-based module can handle previously unobserved faults, which are common in real-world applications, and provide diagnostics on the potential fault types. Furthermore, this module can be applied directly to new data without the need for pre-training, enabling practical use for monitoring new operations in a substation.

9.2.3 Integration of the Three Modules

After obtaining z-scores from all monitored indicators, criteria have to be established to raise alarms or define acceptable deviations that can still be considered healthy. A straightforward approach is to count how many indicators exceed a certain threshold (e.g., number of indicators with z-score > 3). However, this criterion can be biased because many indicators are not independent. For instance, Euclidean

distance from the similarity-based module and the RMS from the feature-based module are strongly correlated. Simply counting indicators above a threshold risks over-weighting a group of inter-dependent features.

One way to mitigate this issue is to assign weights to the indicators or to the modules, giving higher weights to those considered more informative or critical components, such as open coil or contacts. A unified health indicator can then be computed as a weighted combination of indicators to represent the overall CB condition. However, determining appropriate weights is challenging and typically requires substantial domain knowledge and historical data.

Another challenge lies in defining actions based on threshold levels. Thresholds set too high risk allowing a faulty CB to remain in operation, while thresholds set too low may generate excessive false alarms. Establishing suitable weights, thresholds, and corresponding actions requires access to large volumes of historical data for calibration.

More advanced indicators can also be used, such as the derivative of the indicator, which reflects how fast an indicator changes. They can be useful to detect a sudden change in indicator values, especially for indicators that exhibit abrupt deviations rather than a gradual increase or decrease trend. However, the effectiveness can vary depending on CB-fault combinations and their operation conditions.

9.3 Practical Considerations for Substation Deployment

The fourth aim of this work was to design and deploy a data acquisition system and deploy the proposed framework for monitoring CB condition in real-world applications. In this work, the CB condition monitoring system, together with the proposed framework, was successfully deployed to continuously monitor CBs in a substation for over a year.

To collect high-quality data under current interruption in a substation, effective shielding of both sensors and data acquisition systems are required to prevent electromagnetic interference. This is, however, not required for no-load laboratory experiments as no current is interrupted.

In addition, the second aim of this work was to compare condition monitoring signals with and without current interruption, as discussed in Section 6.8.1. The investigation in found out that depending on the CB types, the collected vibration patterns vary more in GCBs due to changes in pressure build-up during the interruption process. While in VCBs, no pressure build-up and thus no apparent changes in the vibration signals for both with and without current interruption conditions.

9.3.1 Idle Time Effect

Field technicians report that one of the most common CB failures in substations is called "Standschäden", which occurs when CBs are not operated for long periods and subsequently fail to operate upon command. This is likely caused by the drying of grease or lubrication, which increases friction to the point that the open or close coil can no longer initiate the operating mechanism. A practical mitigation is to operate CBs periodically to avoid long idle time, allowing the grease to redistribute and maintain proper lubrication.

This observation is similar to the idle time effect identified in the run-to-failure experiments, where operation patterns following a long idle time are different from those with shorter idle times. This change of patterns could also be a result of the changes in grease conditions.

In run-to-failure experiments, idle times are typically less than five minutes, whereas in substations, most operations occur after much longer idle periods of several weeks or even years. However, from the data collected in the substation as presented in Section 8.3.4, when all operations occur with long idle times, an average of one week inactive, the operation patterns remain consistent. In practice, the idle time is also recommended to be part of the monitoring indicators for conditional anomalies.

9.3.2 Threshold-action List

A threshold-action list is a list that defines corresponding actions when the indicators exceed certain thresholds. For example, at the first level, where the CB begins to deviate from its healthy state with increasing z-scores, between 1 and 3, but remains operational, the action may involve operating with caution and scheduling an inspection when possible. At the next level, where indicators show significant deviation, beyond 3 or even 5, from the healthy baseline, operations should be stopped for maintenance to prevent severe consequences from continued CB operation. The thresholds such as z-scores equal to 1, 3, or 5 have to be determined based on domain knowledge and historical operational data.

Maintenance activities are expected to reduce z-scores by aligning subsequent operations closer to the healthy baseline. However, this assumption could not be validated in this work, as no maintenance was performed. If z-scores do not decrease after maintenance, recalibration is required with an additional parameter to denote the maintenance activity. In such cases, the first few operations after maintenance can be taken as the new healthy baseline, with an important caveat that the CB has undergone maintenance rather than being equivalent to a new CB.

9.3.3 Transferability between CBs

The three modules are recommended to be applied only to a single CB at a time; therefore, it is not required to transfer models trained on one CB to another CB of the same type. With a fleet of the same type of CBs, provided that the same sensors are used and installed in the same setup with the same data acquisition systems, such as the case discussed in Section 8.3.4, the framework can be applied to the entire fleet together and treated as a single CB with multiple operations.

However, transferring the models across CB types is challenging based on the results of this work. Such transferability appears to be limited due to substantial differences in operating conditions, design of operating mechanisms, and sensor installation positions.

9.4 Limitations and Challenges

Even though the results demonstrate the effectiveness and feasibility of the proposed framework for monitoring CB health condition, some limitations and challenges still exist and must be considered.

9.4.1 General Data Scarcity and Lack of Labels

As outlined in Section 1.2, data scarcity poses a significant challenge for data-driven CB condition monitoring solutions. In this work, we addressed this by conducting run-to-failure experiments on multiple CBs, collecting datasets from over 30 000 opening and closing operations. This significantly expands the available data volume and facilitates the development of data-driven methods. However, these datasets are collected from only a few CBs, often one or two per type, limiting their generalization ability.

The proposed three-module framework, particularly the feature-based and similarity-based modules, is designed to be effective even with limited data availability. Over the long term, broader deployment of data acquisition and condition monitoring systems in the field would enable the collection of larger, more diverse datasets, enhancing the robustness and generalization of data-driven models.

To address the challenge of a lack of ground-truth fault labels, the features used in the feature-based module with physical explanation or the key moments can help pinpoint the potential faulty components without the need of fault labels. The ML-based module supports unsupervised fault detection and segmentation with an XAI approach applied to the detected faults, achieving fault diagnostics without requiring labels.

9.4.2 Thresholds for Fault Detection

Thresholds are essential for the CB condition monitoring system to determine when to raise alarms, yet selecting suitable thresholds is challenging. Narrow thresholds result in excessive false alarms and undermine trust in the monitoring system, while overly wide thresholds prevent anomalies from being detected. Thresholds presented in this work are based on the historical data from a single CB in a healthy state and can be updated or calibrated based on operating conditions. However, threshold determination can be improved with data from multiple CBs of the same type operating under similar conditions. This allows for distinction between normal variability and true anomalies.

In addition to static thresholds such as the mean plus three times standard deviations, dynamic thresholds based on the most recent operations proven to be in a healthy state could also be applied. However, such an approach may have a risk of mistakenly including faulty operations in the healthy baseline. In addition, dynamic thresholds are more suitable for long-term condition monitoring with a large number of operations, such as in run-to-failure experiments. In real-world applications, CBs typically operate infrequently, making dynamic thresholds less practical.

10 Conclusions and Outlook

*Parts of this section are based on the publication*s [14, 15].

This work introduced a condition monitoring framework for CBs using non-intrusive signals, integrating three complementary modules: feature-based, similarity-based, and ML-based. Each module can independently assess the CB condition and can be aggregated for a comprehensive overview. Rather than replacing traditional time-based maintenance, the framework is intended to enhance existing strategies by offering additional insights into CB condition between scheduled inspections with only basic parameters.

The framework was validated on various CBs types under both run-to-failure experiments and fault injection tests, highlighting its flexibility across different CB types and fault types. In total, over 30 000 switching operations were collected and analyzed, enabling investigation not only of tracking the mechanical degradation but also of fault detection, segmentation, and diagnostics. This represents a shift from the literature-dominant focus on discrete supervised fault classification toward a more realistic perspective of continuous monitoring.

By extracting features and identifying different stages based on the key moments, the feature-based module has demonstrated the feasibility of tracking CB condition over time using non-intrusively measured signals. From a broad set of features, we identified the most effective features for continuous monitoring. These features are different from CB to CB, highlighting that in real-world applications, it is preferable to monitor a wide range of features instead of only a few.

The similarity-based module effectively quantifies changes in non-intrusive signals without the need to have domain knowledge to know what features to extract. Compared to the feature-based module, it is more generalizable since it only requires calculating similarity relative to the healthy baseline. This module can be applied to all monitoring signals, but due to the high dimensionality of raw signals, smoothing is recommended before similarity calculation to obtain more robust results.

The ML-based module consists of an unsupervised fault detection and segmentation approach with an XAI approach to achieve fault diagnostics and assist domain experts in identifying potential fault types. The effectiveness of this module was validated on various CB types, including run-to-failure and fault injection cases. In particular, for the fault injection experiment, the clustering results using three different clustering methods have demonstrated the module's flexibility and feasibility in grouping healthy and unknown faulty samples into distinct clusters. Furthermore, the results from XAI further explain the clustered samples, achieving fault diagnostics even if the fault type has not yet been observed and ground-truth labels are not available during training.

Combining all three modules and monitoring the z-scores of each indicator provides a comprehensive assessment of the CB condition. Case studies on different CBs demonstrate the feasibility of integrating three modules, showing clear transitions from healthy to faulty and to failure, as reflected by the evolution of increasing z-scores. While the degradation patterns vary across CB types and fault modes, a consistent overall trend of increasing z-scores is observed, indicating progressive deviation from the healthy baseline and confirming the capability of the three-module framework to track CB conditions over time.

Besides the proposed framework, the CB run-to-failure experiments highlight the reliability of CBs, which can withstand more than 5 000 no-load operations in the laboratory even after decades in service. This suggests a large potential to extend CB lifetime when equipped with the monitoring framework, provided the CB remains in an operational state. Such an approach would allow utilities to extend the service lifetime of aging breakers, avoid costly premature replacements, and reduce unexpected failures.

This work highlights several future research directions. First, a large-scale deployment of monitoring systems in the field is needed to collect more CB condition monitoring datasets, facilitating research in PHM for CBs, similar to what has been achieved for other equipment, such as industrial bearings. Second, distinguishing between different severities of the same fault type and understanding how levels of severity evolve in the clustering space. Third, future research should focus on determining proper thresholds for triggering alarms for anomaly detection based on the potentially large volume of data collected

in the field, and even remaining useful life prediction, move beyond fault diagnostics to prognostics.

In summary, this work demonstrates that continuous monitoring of CBs using non-intrusive signals, particularly vibration signals, is feasible with the proposed three-module framework. The gap towards real-world applications lies in the lack of large CB datasets collected in substations due to the limited deployment of online monitoring systems. However, this situation may shift as utilities start to adopt digitization strategy and condition monitoring solutions, eventually leading to widespread deployment of condition monitoring systems across CBs in the near future.

11 National and International Cooperation

The project was in cooperation with Hitachi Energy and BKW. They have provided multiple circuit breakers of different types for laboratory testing and investigation. Furthermore, we have installed the prototype condition monitoring systems in a SBB substation.

The following members were involved in the research team at the High Voltage Laboratory at ETH Zurich:

1. Christian Franck (Professor)
2. Chi-Ching Hsu (Doctoral Student)
3. Tino Gfrörer (Doctoral Student)
4. Mahir Muratovic (Postdoctoral Researcher)
5. Zoltan Marcsek (Master Student)
6. Damien Briens (Master Student)
7. Dario Steiner (Bachelor Student)
8. Wilhelm Cordes (Bachelor Student)
9. Pascal Oetiker (Bachelor Student)
10. Tommaso Polonelli (Postdocatoral Researcher, Center for Project Based Learning)

The following members were involved in the research team at the Intelligent Maintenance and Operations Systems Laboratory, EPFL:

1. Olga Fink (Assistant Professor)
2. Gaetan Frusque (Postdoctoral Researcher)
3. Florent Forest (Postdoctoral Researcher)

The following members were involved from the industrial partners, including Hitachi Energy, BKW, and SBB:

1. Andreas Ebner (BKW)
2. Arnaldo Fava (BKW)
3. Dino Haldimann (BKW)
4. Patrick Noth (BKW)
5. Oliver Fritz (Hitachi Energy)
6. Lennart Merkert (Hitachi Energy)
7. Andrew Fairbrother (Hitachi Energy)
8. Thomas Christen (Hitachi Energy)
9. Ali Asghar Razi-Kazemi (Hitachi Energy)
10. Markus Bujotzek (Hitachi Energy)
11. Felipe Macedo (Hitachi Energy)

12. Patrick Stoller (Hitachi Energy)
13. Esteban Zimmermann (Hitachi Energy)
14. Francesco Fusaro (SBB)
15. Oliver Strauss (SBB)
16. Philipp Wenk (SBB)

12 Publications and Other Communications

1. C.-C. Hsu, G. Frusque, M. Muratovic, C. M. Franck, and O. Fink, “Vacuum circuit breaker closing time key moments detection via vibration monitoring: a run-to-failure study,” *2022 IEEE International Conference on Systems, Man, and Cybernetics (SMC)*, pp. 254–260, 2022
2. C.-C. Hsu, G. Frusque, and O. Fink, “A comparison of residual-based methods on fault detection,” *Annual Conference of the PHM Society*, vol. 15, no. 1, 2023
3. C.-C. Hsu, G. Frusque, O. Fink, and C. M. Franck, “Continuous health state monitoring of high voltage circuit breakers,” *IEEE Access*, vol. 13, pp. 89 819–89 830, 2025
4. C.-C. Hsu, G. Frusque, F. Forest, F. Macedo, C. M. Franck, and O. Fink, “Explainable AI guided unsupervised fault diagnostics for high-voltage circuit breakers,” *Reliability Engineering & System Safety*, vol. 263, p. 111199, 2025
5. C. M. Franck, C.-C. Hsu, Y. Xiao, P. Bleuler, G. Frusque, M. Muratovic, and T. Polonelli, “Transmission and distribution equipment: providing intelligent maintenance,” *IEEE Power and Energy Magazine*, vol. 21, no. 2, pp. 18–29, 2023
6. Z. Marcsek, T. Gfrörer, T. Polonelli, C.-C. Hsu, M. Magno, and C. M. Franck, “An IoT sensor platform for predictive maintenance of high voltage circuit breakers,” *10th IEEE International Workshop on Advances in Sensors and Interfaces*, pp. 1–6, 2025
7. C.-C. Hsu and F. Macedo, “eXplainable Artificial Intelligence (XAI) in industrial diagnostic: Interpretable unsupervised anomaly detection,” Presented at the 8th Intelligent Maintenance Conference, Lausanne, Switzerland, September 2024
8. C.-C. Hsu, “Condition monitoring on high-voltage circuit breakers with explainable ai guided fault diagnostics,” Presented at the European Safety and Reliability (ESREL) and Society for Risk Analysis Europe (SRA-E) conference, Stavanger, Norway, June 2025
9. ——, “Anwendungsmöglichkeiten von ki für predictive-maintenance von leistungsschaltern und ihre grenzen,” Presented at the FKH-Fachtagung 2025, Sursee, Switzerland, November 2025

13 Open Access Dataset

The circuit breaker run-to-failure datasets are openly accessible for further research.

Open Access Circuit Breaker Datasets

1. C.-C. Hsu, “Run-to-failure vacuum circuit breaker mechanical test dataset,” in ETH Zürich, Research Collection, Dataset. ETH Zürich, ETH Library, 2022, doi: 10.3929/ethz-b-000544221. [Online]. Available: https://www.research-collection.ethz.ch
2. C.-C. Hsu, “Run-to-failure high-voltage circuit breaker mechanical test dataset,” in ETH Zürich, Research Collection, Dataset. ETH Zürich, ETH Library, 2024, doi: 10.3929/ethz-b-000676480. [Online]. Available: https://www.research-collection.ethz.ch
3. C.-C. Hsu, “Run-to-failure medium-voltage circuit breaker mechanical test dataset," in ETH Zürich, Research Collection, Dataset. ETH Zürich, ETH Library, 2025, http://hdl.handle.net/20.500.11850/785308. [Online]. Available: https://www.research-collection.ethz.ch

14 References

[1] A. Scheuer, M. Bashiri, M. Bründlinger, C. Derks, T. Gönen, T. Kume, G. Mevel, A. Oudalov, M. Palkovic, D. Povh, M. Stanojevic, J. Stevenson, and H. T. V. Smit, *Substations*, ser. CIGRE Green Books. Paris, France: CIGRE, 2019. [Online]. Available: https://link.springer.com/referencework/10.1007/978-3-319-49574-3

[2] IEEE Power Systems Committee, "Ieee standard definitions for power switchgear," *IEEE Std. C37.100-1992 (R 2001)*, pp. 1–101, 1992.

[3] G. Mazza, "The first international enquiry on circuit-breaker failures and defects in service," *Electra*, vol. 79, 1981.

[4] L. Ruff, J. R. Kauffmann, R. A. Vandermeulen, G. Montavon, W. Samek, M. Kloft, T. G. Dietterich, and K.-R. Müller, "A unifying review of deep and shallow anomaly detection," *Proceedings of the IEEE*, vol. 109, no. 5, pp. 756–795, 2021.

[5] O. Fink, Q. Wang, M. Svensen, P. Dersin, W.-J. Lee, and M. Ducoffe, "Potential, challenges and future directions for deep learning in prognostics and health management applications," *Engineering Applications of Artificial Intelligence*, vol. 92, p. 103678, 2020.

[6] H. Ito, Ed., *Switching equipment*, ser. CIGRE Green Books. Springer, 2019. [Online]. Available: https://link.springer.com/referencework/10.1007/978-3-319-72538-3

[7] CIGRE Working Group A3.48, "Fourth cigre international reliability survey on equipment operated in 2014–17 – part 1: general results on transmission and distribution equipment," CIGRE, Technical Brochure 947, 2024.

[8] CIGRE Working Group B3.12, "Obtaining value from on-line substation condition monitoring," CIGRE, Technical Brochure 462, 2011.

[9] O. Fink, "Data-driven intelligent predictive maintenance of industrial assets," *Women in Industrial and Systems Engineering: Key Advances and Perspectives on Emerging Topics*, pp. 589–605, 2020.

[10] R. K. Mobley, *An introduction to predictive maintenance*. Elsevier, 2002.

[11] P. Nectoux, R. Gouriveau, K. Medjaher, E. Ramasso, B. Chebel-Morello, N. Zerhouni, and C. Varnier, "Pronostia: An experimental platform for bearings accelerated degradation tests." in *IEEE International Conference on Prognostics and Health Management*, 2012, pp. 1–8.

[12] B. Wang, Y. Lei, N. Li, and N. Li, "A hybrid prognostics approach for estimating remaining useful life of rolling element bearings," *IEEE Transactions on Reliability*, vol. 69, no. 1, pp. 401–412, 2018.

[13] C.-C. Hsu, "Intelligent maintenance of gas circuit breakers," Doctoral Thesis, ETH Zürich, 2025.

[14] C.-C. Hsu, G. Frusque, O. Fink, and C. M. Franck, "Continuous health state monitoring of high voltage circuit breakers," *IEEE Access*, vol. 13, pp. 89 819–89 830, 2025.

[15] C.-C. Hsu, G. Frusque, F. Forest, F. Macedo, C. M. Franck, and O. Fink, "Explainable AI guided unsupervised fault diagnostics for high-voltage circuit breakers," *Reliability Engineering & System Safety*, vol. 263, p. 111199, 2025.

[16] A. Janssen, D. Makareinis, and C.-E. Sölver, "International surveys on circuit-breaker reliability data for substation and system studies," *IEEE Transactions on Power Delivery*, vol. 29, no. 2, pp. 808–814, 2013.

[17] CIGRE Working Group A3.06, "Final report of the 2004–2007 international enquiry on reliability of high voltage equipment – part 1: summary and general matters; part 2 – reliability of high voltage sf6 circuit breakers," CIGRE, Technical Brochure 509, 2012.

[18] N. Zhou, Y. Xu, S. Cho, and C. T. Wee, “A systematic review for switchgear asset management in power grids: condition monitoring, health assessment, and maintenance strategy,” *IEEE Transactions on Power Delivery*, 2023.

[19] M. Kapetanovic, *High Voltage Circuit Breaker*. ETF - Faculty of Electrotechnical Engineering, University of Sarajevo, 2011.

[20] CIGRE Working Group A3.43, “Tools for lifecycle management of t&d switchgear based on data from condition monitoring,” CIGRE, Technical Brochure 953, 2025.

[21] CIGRE Working Group A3.29, “Ageing high voltage substation equipment and possible mitigation techniques,” CIGRE, Technical Brochure 725, 2018.

[22] A. A. Razi-Kazemi and K. Niayesh, “Condition monitoring of high voltage circuit breakers: Past to future,” *IEEE Transactions on Power Delivery*, vol. 36, no. 2, pp. 740–750, 2020.

[23] K. Obarcanin and B. Lacevic, “Methods for condition assessment of the high voltage circuit breakers based on vibration fingerprint–a survey,” *IEEE Access*, 2025.

[24] A. Vaswani, N. Shazeer, N. Parmar, J. Uszkoreit, L. Jones, A. N. Gomez, Ł. Kaiser, and I. Polosukhin, “Attention is all you need,” *Advances in Neural Information Processing Systems*, vol. 30, 2017.

[25] J. Devlin, M.-W. Chang, K. Lee, and K. Toutanova, “Bert: Pre-training of deep bidirectional transformers for language understanding,” in *Proceedings of the 2019 conference of the North American chapter of the association for computational linguistics: human language technologies, volume 1 (long and short papers)*, 2019, pp. 4171–4186.

[26] J. Deng, W. Dong, R. Socher, L.-J. Li, K. Li, and L. Fei-Fei, “ImageNet: A large-scale hierarchical image database,” in *2009 IEEE conference on Computer Vision and Pattern Recognition*, 2009, pp. 248–255.

[27] CIGRE Working Group 13.08, “Life management of circuit-breakers,” CIGRE, Technical Brochure 165, 2000.

[28] C.-C. Hsu, G. Frusque, M. Muratovic, C. M. Franck, and O. Fink, “Vacuum circuit breaker closing time key moments detection via vibration monitoring: a run-to-failure study,” *2022 IEEE International Conference on Systems, Man, and Cybernetics (SMC)*, pp. 254–260, 2022.

[29] K. Obarcanin, D. Skulj, and B. Lacevic, “High voltage circuit breaker vibration signature indices evaluation for condition assessment,” *B&H Electrical Engineering*, vol. 15, no. 1, pp. 82–88, 2021.

[30] N. Charbkaew, T. Suwanasri, T. Bunyagul, and A. Schnettler, “Vibration signal analysis for condition monitoring of puffer-type high-voltage circuit breakers using wavelet transform,” *IEEJ Transactions on Electrical and Electronic Engineering*, vol. 7, no. 1, pp. 13–22, 2012.

[31] V. Kraynov, A. Zhang, C. Nicolle, and D. Zhang, “Sensors for smart medium voltage circuit breaker,” in *2024 7th International Conference on Electric Power Equipment-Switching Technology (ICEPE-ST)*. IEEE, 2024, pp. 321–324.

[32] A. A. Razi-Kazemi, “Circuit breaker condition assessment through a fuzzy-probabilistic analysis of actuating coil’s current,” *IET Generation, Transmission & Distribution*, vol. 10, no. 1, pp. 48–56, 2016.

[33] Y. Pan, F. Mei, H. Miao, J. Zheng, K. Zhu, and H. Sha, “An approach for hvcb mechanical fault diagnosis based on a deep belief network and a transfer learning strategy,” *Journal of Electrical Engineering & Technology*, vol. 14, pp. 407–419, 2019.

[34] A. A. Razi-Kazemi, “Applicability of auxiliary contacts in circuit breaker online condition assessment,” *Electric Power Systems Research*, vol. 128, pp. 53–59, 2015.

[35] F. N. Rudsari, A. A. Razi-Kazemi, and M. A. Shoorehdeli, “Fault analysis of high-voltage circuit breakers based on coil current and contact travel waveforms through modified svm classifier,” *IEEE Transactions on Power Delivery*, vol. 34, no. 4, pp. 1608–1618, 2019.

[36] M. Abdollah and A. A. Razi-Kazemi, “Intelligent failure diagnosis for gas circuit breakers based on dynamic resistance measurements,” *IEEE Transactions on Instrumentation and Measurement*, vol. 68, no. 9, pp. 3066–3077, 2018.

[37] Y. Liu, G. Zhang, H. Qin, Y. Geng, J. Wang, J. Yang, and K. Zhao, “Prediction of the dynamic contact resistance of circuit breaker based on the kernel partial least squares,” *IET Generation, Transmission & Distribution*, vol. 12, no. 8, pp. 1815–1821, 2018.

[38] T. Sugimoto and M. Shimizu, “Study of condition monitoring by operating sound diagnosis for circuit breaker in substation,” in *2019 5th International Conference on Electric Power Equipment-Switching Technology (ICEPE-ST)*. IEEE, 2019, pp. 622–625.

[39] T. Iwata, T. Endo, J. Nukaga, Y. Takahashi, and T. Nishimura, “Development of acoustic diagnostics for opening and closing operations of gas circuit breakers,” in *2022 6th International Conference on Electric Power Equipment-Switching Technology (ICEPE-ST)*. IEEE, 2022, pp. 67–71.

[40] S. Darnsomboon and W. Boon-Nontae, “Field circuit breaker inspection using machine learning and data analytics on sound recognition,” *CIGRE Session*, no. D2-PS1 10991, 2022.

[41] X. Ye, J. Yan, Y. Wang, J. Wang, and Y. Geng, “A novel u-net and capsule network for few-shot high-voltage circuit breaker mechanical fault diagnosis,” *Measurement*, vol. 199, p. 111527, 2022.

[42] J. Qi, X. Gao, and N. Huang, “Mechanical fault diagnosis of a high voltage circuit breaker based on high-efficiency time-domain feature extraction with entropy features,” *Entropy*, vol. 22, no. 4, p. 478, 2020.

[43] P. Barkan, J. A. Deni, A. K. McCabe, J. G. Reckleff, H. N. Scherer, and R. C. Woodward, “Methodology for monitoring the condition of high voltage circuit-breakers,” *CIGRE Session*, 1988.

[44] T. Laitinen, T. Lyly, M. Stenstrand, J. Tammi, R. Albrecht, J. Nyberg, and K. Saksela, “Wireless sensor units for acoustic monitoring of switching devices,” *CIGRE Session*, no. B3-203_2018, pp. 26–31, 2018.

[45] E. D. Fylladitakis and A. X. Moronis, “Design and development of a prototype operating parameters monitoring system for high-voltage switchgear using iot technologies,” *IEEE Transactions on Power Delivery*, vol. 39, no. 3, pp. 1376–1385, 2024.

[46] E. Zio, “Prognostics and health management (phm): Where are we and where do we (need to) go in theory and practice,” *Reliability Engineering & System Safety*, vol. 218, p. 108119, 2022.

[47] M. A. Chao, B. T. Adey, and O. Fink, “Implicit supervision for fault detection and segmentation of emerging fault types with deep variational autoencoders,” *Neurocomputing*, vol. 454, pp. 324–338, 2021.

[48] C.-C. Hsu, G. Frusque, and O. Fink, “A comparison of residual-based methods on fault detection,” *Annual Conference of the PHM Society*, vol. 15, no. 1, 2023.

[49] S. Zhao and E. Wang, “Fault diagnosis of circuit breaker energy storage mechanism based on current-vibration entropy weight characteristic and grey wolf optimization–support vector machine,” *IEEE Access*, vol. 7, pp. 86 798–86 809, 2019.

[50] G. Floreale, P. Baraldi, X. Lu, P. Rossetti, and E. Zio, “Sensitivity analysis by differential importance measure for unsupervised fault diagnostics,” *Reliability Engineering & System Safety*, vol. 243, p. 109846, 2024.

[51] M. W. Hoffmann, S. Wildermuth, R. Gitzel, A. Boyaci, J. Gebhardt, H. Kaul, I. Amihai, B. Forg, M. Suriyah, T. Leibfried *et al.*, "Integration of novel sensors and machine learning for predictive maintenance in medium voltage switchgear to enable the energy and mobility revolutions," *Sensors*, vol. 20, no. 7, p. 2099, 2020.

[52] C. M. Franck, "Lecture notes in technology of electric power system components," February 2024.

[53] C. M. Franck, C.-C. Hsu, Y. Xiao, P. Bleuler, G. Frusque, M. Muratovic, and T. Polonelli, "Transmission and distribution equipment: providing intelligent maintenance," *IEEE Power and Energy Magazine*, vol. 21, no. 2, pp. 18–29, 2023.

[54] K. Niayesh and M. Runde, *Power switching components*. Springer, 2017.

[55] M. Seeger, R. Smeets, J. Yan, H. Ito, M. Claessens, E. Dullni, L. Falkingham, C. Franck, F. Gentil, W. Hartmann, Y. Kieffel, S. Jia, G. Jones, J. Mantilla, S. Pawar, M. Rabie, P. RobinJuan, H. Schellekens, J. Spencer, T. Uchii, X. Li, and S. Yanabu, "Recent development of alternative gases to sf6 for switching applications," *ELECTRA (CIGRE)*, 2017.

[56] M. Landry, O. Turcotte, and F. Brikci, "A complete strategy for conducting dynamic contact resistance measurements on hv circuit breakers," *IEEE Transactions on Power Delivery*, vol. 23, no. 2, pp. 710–716, 2008.

[57] D. Yan, Y. Shen, D. Zhu, J. Wang, X. Lin, J. Wang, S. Jia, and S. Xiu, "Life cycle state evaluation of auxiliary circuit-breaker in synthetic test circuit based on dynamic contact resistance," in *2024 7th International Conference on Electric Power Equipment-Switching Technology (ICEPE-ST)*. IEEE, 2024, pp. 338–343.

[58] CIGRE Working Group 13.09, "User guide for the application of monitoring and diagnostic techniques for switching equipment for rated voltages of 72.5 kv and above," CIGRE, Technical Brochure 167, 2000.

[59] B. Rusek, G. Balzer, M. Holstein, and M.-S. Claessens, "Timings of high voltage circuit-breaker," *Electric Power Systems Research*, vol. 78, no. 12, pp. 2011–2016, 2008.

[60] P. Grein, "Circuit breaker timing and time travel analysis testing," *NETA World*, pp. 44–54, 2024.

[61] International Electrotechnical Commission, "High-voltage switchgear and controlgear-part 100: high-voltage alternating-current circuit breakers," *International Electrotechnical Commission (IEC), 62271-100*, 2001.

[62] Y. Tan, E. Hu, Y. Liu, J. Li, and W. Chen, "Review of digital vibration signal analysis techniques for fault diagnosis of high-voltage circuit breakers," *IEEE Transactions on Dielectrics and Electrical Insulation*, vol. 31, no. 1, pp. 404–418, 2024.

[63] G. Pang, C. Shen, L. Cao, and A. V. D. Hengel, "Deep learning for anomaly detection: A review," *ACM computing surveys (CSUR)*, vol. 54, no. 2, pp. 1–38, 2021.

[64] G. Li, J. Hu, Y. Ding, A. Tang, J. Ao, D. Hu, and Y. Liu, "A novel method for fault diagnosis of fluid end of drilling pump under complex working conditions," *Reliability Engineering & System Safety*, vol. 248, p. 110145, 2024.

[65] Y. Xu, X. Yan, K. Feng, X. Sheng, B. Sun, and Z. Liu, "Attention-based multiscale denoising residual convolutional neural networks for fault diagnosis of rotating machinery," *Reliability Engineering & System Safety*, vol. 226, p. 108714, 2022.

[66] A. Blazquez-Garcia, A. Conde, U. Mori, and J. A. Lozano, "A review on outlier/anomaly detection in time series data," *ACM Computing Surveys (CSUR)*, vol. 54, no. 3, pp. 1–33, 2021.

[67] H. Deng and X. Li, "Anomaly detection via reverse distillation from one-class embedding," in *Proceedings of the IEEE/CVF Conference on Computer Vision and Pattern Recognition*, 2022, pp. 9737–9746.

[68] K. Roth, L. Pemula, J. Zepeda, B. Schölkopf, T. Brox, and P. Gehler, “Towards total recall in industrial anomaly detection,” in *Proceedings of the IEEE/CVF Conference on Computer Vision and Pattern Recognition*, 2022, pp. 14 318–14 328.

[69] J. Wu, C. Wu, S. Cao, S. W. Or, C. Deng, and X. Shao, “Degradation data-driven time-to-failure prognostics approach for rolling element bearings in electrical machines,” *IEEE Transactions on Industrial Electronics*, vol. 66, no. 1, pp. 529–539, 2018.

[70] A. Carreño, I. Inza, and J. A. Lozano, “Analyzing rare event, anomaly, novelty and outlier detection terms under the supervised classification framework,” *Artificial Intelligence Review*, vol. 53, pp. 3575–3594, 2020.

[71] G. Chen, G. Lu, Z. Xie, and W. Shang, “Anomaly detection in eeg signals: a case study on similarity measure,” *Computational intelligence and neuroscience*, vol. 2020, no. 1, p. 6925107, 2020.

[72] P. Vincent, H. Larochelle, Y. Bengio, and P.-A. Manzagol, “Extracting and composing robust features with denoising autoencoders,” in *Proceedings of the 25th International Conference on Machine Learning*, 2008, pp. 1096–1103.

[73] P. Vincent, H. Larochelle, I. Lajoie, Y. Bengio, P.-A. Manzagol, and L. Bottou, “Stacked denoising autoencoders: Learning useful representations in a deep network with a local denoising criterion.” *Journal of Machine Learning Research*, vol. 11, no. 12, 2010.

[74] D. P. Kingma and M. Welling, “Auto-encoding variational bayes,” *arXiv preprint arXiv:1312.6114*, 2013.

[75] B. Schölkopf, J. C. Platt, J. Shawe-Taylor, A. J. Smola, and R. C. Williamson, “Estimating the support of a high-dimensional distribution,” *Neural computation*, vol. 13, no. 7, pp. 1443–1471, 2001.

[76] L. Ruff, R. Vandermeulen, N. Goernitz, L. Deecke, S. A. Siddiqui, A. Binder, E. Müller, and M. Kloft, “Deep one-class classification,” in *Proceedings of the 35th International Conference on Machine Learning*, ser. Proceedings of Machine Learning Research, vol. 80. PMLR, 2018, pp. 4393–4402.

[77] P. Bergmann, M. Fauser, D. Sattlegger, and C. Steger, “Uninformed students: Student-teacher anomaly detection with discriminative latent embeddings,” in *Proceedings of the IEEE/CVF Conference on Computer Vision and Pattern Recognition*, 2020, pp. 4183–4192.

[78] M. Salehi, N. Sadjadi, S. Baselizadeh, M. H. Rohban, and H. R. Rabiee, “Multiresolution knowledge distillation for anomaly detection,” in *Proceedings of the IEEE/CVF Conference on Computer Vision and Pattern Recognition*, 2021, pp. 14 902–14 912.

[79] M. Sabokrou, M. Khalooei, M. Fathy, and E. Adeli, “Adversarially learned one-class classifier for novelty detection,” in *Proceedings of the IEEE conference on Computer Vision and Pattern Recognition*, 2018, pp. 3379–3388.

[80] T. Schlegl, P. Seeböck, S. M. Waldstein, U. Schmidt-Erfurth, and G. Langs, “Unsupervised anomaly detection with generative adversarial networks to guide marker discovery,” in *International Conference on Information Processing in Medical Imaging*. Springer, 2017, pp. 146–157.

[81] A. B. Arrieta, N. Díaz-Rodríguez, J. Del Ser, A. Bennetot, S. Tabik, A. Barbado, S. García, S. Gil-López, D. Molina, R. Benjamins *et al.*, “Explainable artificial intelligence (XAI): concepts, taxonomies, opportunities and challenges toward responsible AI,” *Information fusion*, vol. 58, pp. 82–115, 2020.

[82] S. Pashami, S. Nowaczyk, Y. Fan, J. Jakubowski, N. Paiva, N. Davari, S. Bobek, S. Jamshidi, H. Sarmadi, A. Alabdallah, R. P. Ribeiro, B. Veloso, M. Sayed-Mouchaweh, L. Rajaoarisoa, G. J. Nalepa, and J. Gama, “Explainable predictive maintenance,” *arXiv preprint arXiv:2306.05120*, 2023.

[83] L. Cummins, A. Sommers, S. B. Ramezani, S. Mittal, J. Jabour, M. Seale, and S. Rahimi, "Explainable predictive maintenance: A survey of current methods, challenges and opportunities," *IEEE Access*, vol. 12, pp. 57 574–57 602, 2024.

[84] J. Reckleff, A. McCabe, and J. H. N. Scherer, "Maintenance procedures and experience with circuit-breakers on the american electric power system," *CIGRE, 1984*, 1984.

[85] E. D. Fylladitakis, "Fault identification and predictive maintenance techniques for high-voltage equipment: a review and recent advances," *Journal of Power and Energy Engineering*, vol. 13, no. 7, pp. 1–39, 2025.

[86] M. Stanek, "Model-aided diagnosis for high voltage circuit breakers," Ph.D. dissertation, ETH Zürich, 2000.

[87] M. Hosseini, B. Stephen, S. D. McArthur, and J. Helm, "Current-based trip coil analysis of circuit breakers for fault diagnosis," in *2018 IEEE PES Innovative Smart Grid Technologies Conference Europe (ISGT-Europe)*. IEEE, 2018, pp. 1–6.

[88] Y. Fu, X. Duan, L. Wu, Z. Jiang, and M. Liao, "Research on fault diagnosis of high voltage circuit breakers based on improved fcn," in *2024 7th International Conference on Electric Power Equipment-Switching Technology (ICEPE-ST)*. IEEE, 2024, pp. 387–391.

[89] K. Chen, F. Wang, H. Li, H. Gao, Y. Xia, and Y. Liu, "Remaining life prediction of high-voltage circuit breakers based on optimized particle swarm-bidirectional long short-term memory neural network," in *2024 7th International Conference on Electric Power Equipment-Switching Technology (ICEPE-ST)*. IEEE, 2024, pp. 697–701.

[90] C. Zhao, G. Zhang, W. Zheng, Z. Mao, L. Liu, and J. Liu, "Mechanical fault identification of high-voltage circuit breaker based on neural network and lifelong learning," in *2024 7th International Conference on Electric Power Equipment-Switching Technology (ICEPE-ST)*. IEEE, 2024, pp. 668–672.

[91] L. Lundgaard, "Partial discharge - Part XIV: Acoustic partial discharge detection-practical application," *IEEE Electrical Insulation Magazine*, vol. 8, no. 5, pp. 34–43, 2002.

[92] S. Wang, Y. Zhou, and Z. Ma, "Research on fault identification of high-voltage circuit breakers with characteristics of voiceprint information," *Scientific Reports*, vol. 14, no. 1, p. 9340, 2024.

[93] A. Stokes and L. Timbs, "Circuit breaker diagnostics," *CIGRE Session*, pp. 13–03, 1988.

[94] V. Demjanenko and L. K. Benenson, "Mechanical failure detection of circuit breakers," *IEEE Transactions on Power Delivery*, vol. 3, no. 4, 1988.

[95] S. Park, M. Lai, C. Lin, H. Naidu, A. Soom, A. Reinhorn, Y. Lee, V. Demjanenko, D. Benenson, T. Soong *et al.*, "Measurements for noninvasive mechanical diagnostics of power circuit breakers," *Electric Power Systems Research*, vol. 19, no. 1, pp. 1–10, 1990.

[96] M. Runde, T. Aurud, L. Lundgaard, G. Ottesen, and K. Faugstad, "Acoustic diagnosis of high voltage circuit-breakers," *IEEE Transactions on Power Delivery*, vol. 7, no. 3, pp. 1306–1315, 1992.

[97] P. Voumard, "A simple approach to condition monitoring of circuit-breakers," *CIGRE Session*, no. 13-203_1994, 1994.

[98] D. Hess, S. Park, M. K. Tangri, S. Vougioukas, A. Soom, V. Demjanenko, R. Acharya, D. Benenson, and S. Wright, "Noninvasive condition assessment and event timing for power circuit breakers," *IEEE Transactions on Power Delivery*, vol. 7, no. 1, pp. 353–360, 1992.

[99] A. Polycarpou, A. Soom, V. Swarnakar, R. Valtin, R. Acharya, V. Demjanenko, M. Soumekh, D. Benenson, and J. Porter, "Event timing and shape analysis of vibration bursts from power circuit breakers," *IEEE Transactions on Power Delivery*, vol. 11, no. 2, pp. 848–857, 1996.

[100] M. Landry, F. Léonard, C. Landry, R. Beauchemin, O. Turcotte, and F. Brikci, “An improved vibration analysis algorithm as a diagnostic tool for detecting mechanical anomalies on power circuit breakers,” *IEEE Transactions on Power Delivery*, vol. 23, no. 4, pp. 1986–1994, 2008.

[101] N. Huang, H. Chen, S. Zhang, G. Cai, W. Li, D. Xu, and L. Fang, “Mechanical fault diagnosis of high voltage circuit breakers based on wavelet time-frequency entropy and one-class support vector machine,” *Entropy*, vol. 18, no. 1, p. 7, 2015.

[102] D. S. Lee, B. J. Lithgow, and R. E. Morrison, “New fault diagnosis of circuit breakers,” *IEEE Transactions on Power Delivery*, vol. 18, no. 2, pp. 454–459, 2003.

[103] I. Goodfellow, Y. Bengio, A. Courville, and Y. Bengio, *Deep learning*. MIT press Cambridge, 2016, vol. 1, no. 2.

[104] Y. LeCun, Y. Bengio, and G. Hinton, “Deep learning,” *Nature*, vol. 521, no. 7553, pp. 436–444, 2015.

[105] Q. Yang, J. Ruan, Z. Zhuang, and D. Huang, “Condition evaluation for opening damper of spring operated high-voltage circuit breaker using vibration time-frequency image,” *IEEE Sensors Journal*, vol. 19, no. 18, pp. 8116–8126, 2019.

[106] X. Ye, J. Yan, Y. Wang, L. Lu, and R. He, “A novel capsule convolutional neural network with attention mechanism for high-voltage circuit breaker fault diagnosis,” *Electric Power Systems Research*, vol. 209, p. 108003, 2022.

[107] W. Samek, G. Montavon, S. Lapuschkin, C. J. Anders, and K.-R. Müller, “Explaining deep neural networks and beyond: A review of methods and applications,” *Proceedings of the IEEE*, vol. 109, no. 3, pp. 247–278, 2021. [Online]. Available: https://ieeexplore.ieee.org/document/9369420

[108] M. D. Zeiler and R. Fergus, “Visualizing and understanding convolutional networks,” in *European Conference on Computer Vision (ECCV)*. Springer, 2014, pp. 818–833.

[109] D. Baehrens, T. Schroeter, S. Harmeling, M. Kawanabe, K. Hansen, and K.-R. Müller, “How to explain individual classification decisions,” *Journal of Machine Learning Research*, vol. 11, no. 61, pp. 1803–1831, 2010. [Online]. Available: http://jmlr.org/papers/v11/baehrens10a.html

[110] M. Sundararajan, A. Taly, and Q. Yan, “Axiomatic attribution for deep networks,” in *International Conference on Machine Learning*. PMLR, 2017, pp. 3319–3328.

[111] G. Montavon, A. Binder, S. Lapuschkin, W. Samek, and K.-R. Müller, “Layer-wise relevance propagation: an overview,” *Explainable AI: interpreting, explaining and visualizing deep learning*, pp. 193–209, 2019.

[112] S. Bach, A. Binder, G. Montavon, F. Klauschen, K.-R. Müller, and W. Samek, “On pixel-wise explanations for non-linear classifier decisions by layer-wise relevance propagation,” *PloS one*, vol. 10, no. 7, p. e0130140, 2015.

[113] G. Li, Q. Yao, C. Fan, C. Zhou, G. Wu, Z. Zhou, and X. Fang, “An explainable one-dimensional convolutional neural networks based fault diagnosis method for building heating, ventilation and air conditioning systems,” *Building and Environment*, vol. 203, p. 108057, 2021.

[114] C. Zhu, Z. Chen, R. Zhao, J. Wang, and R. Yan, “Decoupled feature-temporal CNN: explaining deep learning-based machine health monitoring,” *IEEE Transactions on Instrumentation and Measurement*, vol. 70, pp. 1–13, 2021. [Online]. Available: https://ieeexplore.ieee.org/abstract/document/9442731

[115] Z. Chen, W. Qin, G. He, J. Li, R. Huang, G. Jin, and W. Li, “Explainable deep ensemble model for bearing fault diagnosis under variable conditions,” *IEEE Sensors Journal*, vol. 23, no. 15, pp. 17 737–17 750, 2023.

[116] L. Lomazzi, S. Fabiano, M. Parziale, M. Giglio, and F. Cadini, “On the explainability of convolutional neural networks processing ultrasonic guided waves for damage diagnosis,” *Mechanical Systems and Signal Processing*, vol. 183, p. 109642, 2023. [Online]. Available: https://www.sciencedirect.com/science/article/abs/pii/S0888327022007282

[117] H.-Y. Chen and C.-H. Lee, “Vibration signals analysis by explainable artificial intelligence (XAI) approach: application on bearing faults diagnosis,” *IEEE Access*, vol. 8, pp. 134 246–134 256, 2020. [Online]. Available: https://ieeexplore.ieee.org/abstract/document/9131692

[118] M. S. Kim, J. P. Yun, and P. Park, “An Explainable Neural Network for Fault Diagnosis With a Frequency Activation Map,” *IEEE Access*, vol. 9, pp. 98 962–98 972, 2021. [Online]. Available: https://ieeexplore.ieee.org/abstract/document/9477565

[119] T. Decker, M. Lebacher, and V. Tresp, “Does your model think like an engineer? explainable ai for bearing fault detection with deep learning,” in *ICASSP 2023-2023 IEEE International Conference on Acoustics, Speech and Signal Processing (ICASSP)*. IEEE, 2023, pp. 1–5.

[120] J. Grezmak, P. Wang, C. Sun, and R. X. Gao, “Explainable convolutional neural network for gearbox fault diagnosis,” *Procedia CIRP*, vol. 80, pp. 476–481, Jan. 2019. [Online]. Available: https://www.sciencedirect.com/science/article/pii/S2212827118312873

[121] J.-H. Han, S.-U. Park, and S.-K. Hong, “A study on the effectiveness of current data in motor mechanical fault diagnosis using XAI,” *Journal of Electrical Engineering & Technology*, vol. 17, no. 6, pp. 3329–3335, Nov. 2022. [Online]. Available: https://doi.org/10.1007/s42835-022-01207-y

[122] D. C. Sanakkayala, V. Varadarajan, N. Kumar, Karan, G. Soni, P. Kamat, S. Kumar, S. Patil, and K. Kotecha, “Explainable AI for Bearing Fault Prognosis Using Deep Learning Techniques,” *Micromachines*, vol. 13, no. 9, p. 1471, 2022. [Online]. Available: https://www.mdpi.com/2072-666X/13/9/1471

[123] Y. Tan, J. Gong, S. Li, J. Li, and W. Chen, “Fault feature assessment method for high-voltage circuit breakers based on explainable image recognition,” *IEEE Transactions on Dielectrics and Electrical Insulation*, vol. 32, no. 1, pp. 92–101, 2025.

[124] G. Montavon, J. Kauffmann, W. Samek, and K.-R. Müller, “Explaining the predictions of unsupervised learning models,” in *International Workshop on Extending Explainable AI Beyond Deep Models and Classifiers*. Springer, 2020, pp. 117–138.

[125] J. Gama, R. P. Ribeiro, S. Mastelini, N. Davari, and B. Veloso, “From fault detection to anomaly explanation: a case study on predictive maintenance,” *Journal of Web Semantics*, vol. 81, p. 100821, 2024.

[126] J. Kauffmann, M. Esders, L. Ruff, G. Montavon, W. Samek, and K.-R. Müller, “From clustering to cluster explanations via neural networks,” *IEEE Transactions on Neural Networks and Learning Systems*, 2022.

[127] P. W. Koh, T. Nguyen, Y. S. Tang, S. Mussmann, E. Pierson, B. Kim, and P. Liang, “Concept bottleneck models,” in *Proceedings of the 37 th International Conference on Machine Learning*, 2020.

[128] F. Forest, K. Rombach, and O. Fink, “Interpretable prognostics with concept bottleneck models,” *Information Fusion*, p. 103427, 2025.

[129] O. Li, H. Liu, C. Chen, and C. Rudin, “Deep learning for case-based reasoning through prototypes: A neural network that explains its predictions,” in *Proceedings of the AAAI Conference on Artificial Intelligence*, vol. 32, 2018.

[130] C. Chen, O. Li, D. Tao, A. Barnett, C. Rudin, and J. K. Su, “This looks like that: deep learning for interpretable image recognition,” in *Advances in Neural Information Processing Systems*, vol. 32, 2019.

[131] S. Verma, V. Boonsanong, M. Hoang, K. Hines, J. Dickerson, and C. Shah, "Counterfactual explanations and algorithmic recourses for machine learning: A review," *ACM Computing Surveys*, vol. 56, no. 12, pp. 1–42, 2024.

[132] J. F. Barraza, E. L. Droguett, and M. R. Martins, "SCF-Net: A sparse counterfactual generation network for interpretable fault diagnosis," *Reliability Engineering & System Safety*, vol. 250, p. 110285, 2024.

[133] Q. Yang, Z. Wang, J. Ruan, and Z. Zhuang, "Small-sample fault diagnosis method for high-voltage circuit breakers via data augmentation and deep learning," *IEEE Transactions on Instrumentation and Measurement*, 2024.

[134] Y. Wang, J. Yan, X. Ye, Q. Jing, J. Wang, and Y. Geng, "Few-shot transfer learning with attention mechanism for high-voltage circuit breaker fault diagnosis," *IEEE Transactions on Industry Applications*, vol. 58, no. 3, pp. 3353–3360, 2022.

[135] K. Loparo, "Case western reserve university bearing data center," *Bearings Vibration Data Sets, Case Western Reserve University*, pp. 22–28, 2012.

[136] M. A. Chao, C. Kulkarni, K. Goebel, and O. Fink, "Aircraft engine run-to-failure dataset under real flight conditions for prognostics and diagnostics," *Data*, vol. 6, no. 1, p. 5, 2021.

[137] A. Saxena, K. Goebel, D. Simon, and N. Eklund, "Damage propagation modeling for aircraft engine run-to-failure simulation," in *2008 international conference on prognostics and health management*. IEEE, 2008, pp. 1–9.

[138] S. Rudd, V. Catterson, S. McArthur, and C. Johnstone, "Circuit breaker prognostics using sf 6 data," in *2011 IEEE Power and Energy Society General Meeting*. IEEE, 2011, pp. 1–6.

[139] R. Gitzel, F. Frech, and A. Boyaci, "Evaluation of anomaly detection algorithms on circuit breaker lifetime test data," vol. 24, 2024.

[140] C.-C. Hsu, "Run-to-failure vacuum circuit breaker mechanical test dataset," in *ETH Zürich, Research Collection, Dataset*. ETH Zürich, ETH Library, 2022, doi: 10.3929/ethz-b-000544221. [Online]. Available: https://www.research-collection.ethz.ch

[141] A. Ukil, M. Zlatanski, and M. Hochlehnert, "Monitoring of HV generator circuit breaker contact ablation based on acoustic emission," *IEEE Transactions on Instrumentation and Measurement*, vol. 62, no. 10, pp. 2683–2693, 2013.

[142] C. Franck, J. T. Engelbrecht, M. Muratovic, P. Pietrzak, P. Simka, and Current Zero Club, "Comparative test program framework for non-sf6 switching gases," *B&H Electrical Engineering*, vol. 15, no. 1, pp. 19–26, 2021.

[143] Z. Marcsek, T. Gfrörer, T. Polonelli, C.-C. Hsu, M. Magno, and C. M. Franck, "An IoT sensor platform for predictive maintenance of high voltage circuit breakers," *10th IEEE International Workshop on Advances in Sensors and Interfaces*, pp. 1–6, 2025.

[144] Z. Marcsek, "A low-Power IoT sensor platform for predictive maintenance of high voltage circuit breaker," Master Thesis, ETH Zürich, 2025.

[145] H. K. Hoidalen and M. Runde, "Continuous monitoring of circuit breakers using vibration analysis," *IEEE Transactions on Power Delivery*, vol. 20, no. 4, pp. 2458–2465, 2005.

[146] C.-C. Hsu, "Run-to-failure high-voltage circuit breaker mechanical test dataset," in *ETH Zürich, Research Collection, Dataset*. ETH Zürich, ETH Library, 2024, 10.3929/ethz-b-000676480. [Online]. Available: https://www.research-collection.ethz.ch

[147] F. Macedo, T. Christen, and A. Garyfallos, "Diagnostics of high voltage circuit breakers by monitoring of vibration signals," *CIGRE Condition Monitoring, Diagnosis and Maintenance, CMDM2023*, 2023.

[148] Y. Meng, S. Jia, Z. Shi, and M. Rong, “The detection of the closing moments of a vacuum circuit breaker by vibration analysis,” *IEEE transactions on Power Delivery*, vol. 21, no. 2, pp. 652–658, 2006.

[149] Y. Meng, S. Jia, and M. Rong, “Condition monitoring of vacuum circuit breakers using vibration analysis,” in *XXIst International Symposium on Discharges and Electrical Insulation in Vacuum, 2004. Proceedings. ISDEIV.*, vol. 2. IEEE, 2004, pp. 341–344.

[150] M. Muratovic, J. T. Engelbrecht, P. Simka, P. Pietrzak, F. Mächler, S. Erismann, and C. M. Franck, “An experimental circuit breaker for benchmarking the intrinsic interruption performance of sf6 alternative gas mixtures,” *IEEE Transactions on Power Delivery*, vol. 39, no. 6, pp. 3082–3091, 2024.

[151] A. Secic and K. Obarcanin, “Power circuit breaker condition assessment based on vibration fingerprint measurement and why it can save your day,” *NETA World*, pp. 73–79, 2017.

[152] M. Jalil, F. A. Butt, and A. Malik, “Short-time energy, magnitude, zero crossing rate and autocorrelation measurement for discriminating voiced and unvoiced segments of speech signals,” in *2013 The International Conference on Technological Advances In Electrical, Electronics And Computer Engineering (TAEECE)*. IEEE, 2013, pp. 208–212.

[153] R. W. Schafer and L. R. Rabiner, “Digital representations of speech signals,” *Proceedings of the IEEE*, vol. 63, no. 4, pp. 662–677, 1975.

[154] J. W. Picone, “Signal modeling techniques in speech recognition,” *Proceedings of the IEEE*, vol. 81, no. 9, pp. 1215–1247, 1993.

[155] R. B. Blackman and J. W. Tukey, “The measurement of power spectra from the point of view of communications engineering—part i,” *Bell System Technical Journal*, vol. 37, no. 1, pp. 185–282, 1958.

[156] K. Obarcanin, D. Skulj, and B. Lacevic, “Condition assessment of power circuit breakers based on machine learning algorithms,” *IEEE Transactions on Power Delivery*, 2023.

[157] Z. Wang and A. C. Bovik, “Mean squared error: love it or leave it? a new look at signal fidelity measures,” *IEEE Signal Processing Magazine*, vol. 26, no. 1, pp. 98–117, 2009.

[158] Z. Wang, A. C. Bovik, H. R. Sheikh, and E. P. Simoncelli, “Image quality assessment: from error visibility to structural similarity,” *IEEE Transactions on Image Processing*, vol. 13, no. 4, pp. 600–612, 2004.

[159] M. Ankerst, M. M. Breunig, H.-P. Kriegel, and J. Sander, “Optics: Ordering points to identify the clustering structure,” *ACM Sigmod record*, vol. 28, no. 2, pp. 49–60, 1999.

[160] T. Kohonen, “The self-organizing map,” *Proceedings of the IEEE*, vol. 78, no. 9, pp. 1464–1480, 1990.

[161] F. Forest, Q. Cochard, C. Noyer, M. Joncour, J. Lacaille, M. Lebbah, and H. Azzag, “Large-scale vibration monitoring of aircraft engines from operational data using self-organized models,” in *Annual Conference of the PHM Society*, vol. 12, 2020, p. 11. [Online]. Available: https://papers.phmsociety.org/index.php/phmconf/article/view/1131

[162] F. Forest, H. Porta, D. Tuia, and O. Fink, “From classification to segmentation with explainable ai: A study on crack detection and growth monitoring,” *Automation in Construction*, vol. 165, p. 105497, 2024.

[163] H. Purohit, R. Tanabe, K. Ichige, T. Endo, Y. Nikaido, K. Suefusa, and Y. Kawaguchi, “Mimii dataset: Sound dataset for malfunctioning industrial machine investigation and inspection,” *arXiv preprint arXiv:1909.09347*, 2019.

[164] H. Meng, T. Yan, F. Yuan, and H. Wei, “Speech emotion recognition from 3d log-mel spectrograms with deep learning network,” *IEEE Access*, vol. 7, pp. 125 868–125 881, 2019.

[165] L. Hubert and P. Arabie, “Comparing partitions,” *Journal of classification*, vol. 2, pp. 193–218, 1985.

[166] A. Rosenberg and J. Hirschberg, “V-measure: a conditional entropy-based external cluster evaluation measure,” in *Proceedings of the 2007 joint conference on empirical methods in natural language processing and computational natural language learning (EMNLP-CoNLL)*, 2007, pp. 410–420.

[167] F. Forest, M. Lebbah, H. Azzag, and J. Lacaille, “A survey and implementation of performance metrics for self-organized maps,” *arXiv preprint arXiv:2011.05847*, 2020.

[168] D. Alvarez Melis and T. Jaakkola, “Towards robust interpretability with self-explaining neural networks,” *Advances in Neural Information Processing Systems*, vol. 31, 2018.

[169] D. P. Kingma and J. Ba, “Adam: a method for stochastic optimization,” *arXiv preprint arXiv:1412.6980*, 2014.

[170] G. Vettigli, “Minisom: minimalistic and numpy-based implementation of the self organizing map,” 2018, github.com/JustGlowing/minisom/. [Online]. Available: https://github.com/JustGlowing/minisom/

[171] C.-C. Hsu and F. Macedo, “eXplainable Artificial Intelligence (XAI) in industrial diagnostic: Interpretable unsupervised anomaly detection,” Presented at the 8th Intelligent Maintenance Conference, Lausanne, Switzerland, September 2024.

[172] C.-C. Hsu, “Condition monitoring on high-voltage circuit breakers with explainable ai guided fault diagnostics,” Presented at the European Safety and Reliability (ESREL) and Society for Risk Analysis Europe (SRA-E) conference, Stavanger, Norway, June 2025.

[173] ——, “Anwendungsmöglichkeiten von ki für predictive-maintenance von leistungsschaltern und ihre grenzen,” Presented at the FKH-Fachtagung 2025, Sursee, Switzerland, November 2025.